

UNIVERSITY OF BIRMINGHAM

MANIPULATION OF ULTRACOLD ATOMIC GASES WITH SPATIALLY AND TEMPORALLY CONTROLLED OPTICAL POTENTIALS

by

THOMAS EASTON

A thesis submitted to the University of Birmingham for the degree of

DOCTOR OF PHILOSOPHY

Cold Atoms

School of Physics and Astronomy

College of Engineering and Physical Sciences

University of Birmingham

September 2023

UNIVERSITY OF
BIRMINGHAM

University of Birmingham Research Archive

e-theses repository

This unpublished thesis/dissertation is copyright of the author and/or third parties. The intellectual property rights of the author or third parties in respect of this work are as defined by The Copyright Designs and Patents Act 1988 or as modified by any successor legislation.

Any use made of information contained in this thesis/dissertation must be in accordance with that legislation and must be properly acknowledged. Further distribution or reproduction in any format is prohibited without the permission of the copyright holder.

© Copyright by THOMAS EASTON, 2023

All Rights Reserved

Abstract

This thesis focusses on the use of a Digital Micromirror Device (DMD) to produce spatially and temporally varying optical potentials for the manipulation of ultracold atoms. I discuss the apparatus used to generate ultracold atomic samples as well as that used to manipulate them, including a comparison of the various light sources used with the DMD. Here I demonstrate the advantages in image quality that can be achieved using a superluminescent diode. I also report on work which uses the capability to produce spatially and temporally controlled potentials to engineer a synthetic dimension of harmonic oscillator sites, forming a lattice consisting of 10s of lattice sites on which Bloch Oscillations are demonstrated. Finally I describe simulations which demonstrate the clustering behaviour of quantised vortices in a Bose-Einstein condensate when arranged in linear structures, as could be done by the method of phase imprinting using a DMD. I demonstrate the use of a cluster detection algorithm which is novel in the field of quantised vortices, and show that in many cases, vortex clusters can be modelled by methods similar to those used for single vortices.

To Abi,

Acknowledgements

I'd like to begin by thanking some of the many people who have helped me in my journey to get to this point. I'm sure I'll miss people, and I'm sorry if I do. Firstly, I have to thank my supervisor Giovanni for all of his tireless work training and guiding all of us in the lab. None of this would have been possible without his steady hand on the tiller. Next, Jaime and Aaron, the more senior PhD students on the QPrint experiment, who patiently trained me up on the machine and went through the highs and lows of laboratory life along with me. I can't forget Anna from whom we took the experiment, and who we often leaned on for help. There are also Symran and James, the next generation who I have every expectation will take the experiment to greater heights. I must also thank Marios, whose enthusiasm for our simulations project never dwindled, no matter how many nitpicks I made, and without whom that work would never have been finished. I wish him the best of luck in the rest of his long PhD. I must also acknowledge our lab-roommate experiment: Qmix. Jorge, Eric, Rahul, Tom and Manan have all been there for us whenever we needed support (of either the technical or moral variety). I won't individually name the rest of the cold atoms department at Birmingham, but it has been a pleasure to work with you all, and I hope the many friendships I have made there will continue long after I graduate. Of course I would never have even got to Birmingham without my amazing family. My parents always encouraged me to be curious and supported me in doing what I loved, and my brother Jack inspired me with his intelligence and thoughtfulness. Lastly and certainly not least, I must thank my wonderful fiancée Abi. She has put up with a lot over the course of my PhD (as well as before), not least of which was being stuck in a flat with me non-stop during the COVID lockdowns. Despite that she has supported me every step of the way, sharing my

excitement when I published papers, understanding when I had to spend long hours in the lab and encouraging me to keep writing when the thesis seemed an overwhelming task. She has even tried listening when I've explained the project. Multiple times!

Contents

Abstract i

Acknowledgements v

Contents vii

List of Figures x

List of Acronyms xiii

List of Publications xiv

1 Introduction 1

1.1 Overview of Thesis . . . 2

1.2 Bose-Einstein Condensates . . . 4

1.3 Optical Potentials in Cold Atoms . . . 5

1.3.1 Theory of Optical Potentials . . . 6

1.3.2 Phase Imprinting . . . 8

1.4 Synthetic Dimensions . . . 10

1.5 Quantised Vortices . . . 12

2 Experimental Apparatus 14

2.1 Vacuum System . . . 15

2.2 Optical Setup . . . 16

2.2.1 Lasers & Laser Locking . . . 16
2.2.2 Imaging Systems . . . 19
2.3 Magneto-Optical Traps . . . 21
2.3.1 Working Principle . . . 21
2.3.2 Experimental Implementation . . . 22
2.4 Optical Dipole Trap . . . 23
2.4.1 Crossed Optical Dipole Trap . . . 24
2.4.2 Flattened Trap . . . 25
2.5 Sequence Control . . . 26
2.6 Optical Potentials . . . 28
2.6.1 Digital Micromirror Device . . . 28
2.6.2 Tuneable Laser . . . 32
2.6.3 Superluminescent Diode . . . 32
2.6.4 Red Laser . . . 41

3 Implementation of Synthetic Dimensions with Atomic Trapped States 43
3.1 Overview of Scheme . . . 44
3.2 Experimental Implementation . . . 47
3.3 Bloch Oscillations . . . 48
3.4 Analytical results . . . 56
3.5 Creation of highly-excited states . . . 58

4 Simulations of Clustering Dynamics in Quantised Vortex Systems 64
4.1 Quantised Vorticity . . . 65
4.2 Simulation Methods . . . 66
4.2.1 Ground State . . . 67
4.2.2 Time Evolution . . . 68
4.3 Cluster Formation . . . 69
4.4 Cluster Detection . . . 72

4.5 Vortex Dynamics 75
4.6 Cluster Dynamics 77

5 Conclusions and Outlook **81**

References **85**

List of Figures

2.1 Image of the experimental apparatus 14

2.2 Schematic showing the connections between the various components of the apparatus 15

2.3 Hyperfine structure for the $5^2S_{1/2}$, $5^2P_{1/2}$ and $5^2P_{3/2}$ levels (not to scale) . . . 17

2.4 Schematic showing the connections between the various components of the laser locking system. 19

2.5 Schematic showing the components of the imaging systems, along with the path along which imprinting light is sent from the DMD (see section 2.6). 20

2.6 Schematic diagram of the various laser beams around the science chamber. a) Cut-through view from the side. Atoms arrive from the 2D MOT via resonant push beam from the left. The radial MOT beams are arranged at 45° from vertical to allow room above and below the chamber for microscope objectives which are used for imaging and projecting the imprinting light (see sections 2.2.2 and 2.6. b) Cut-through view from above. The axial MOT beams, which include repumping light, crossed dipole beams (section 2.4.1), flat trap beam (section 2.4.2) and horizontal imaging beam (section 2.4.2 all lie in the horizontal plane. 23

2.7 Absorption images of a typical cloud 24

2.8 Simulations of the beam propagation through the flat trap optics after exiting the optical fibre 25

2.9 Images of the flattened trap 26

2.10 Diagram of the analogue and digital signals for a typical experimental sequence 27

2.11 Image of our DMD in position 29
2.12 Ray diagram for a reflective diffraction grating in three configurations and SEM of a DMD pixel 30
2.13 Curves showing the angles of incidence, α, which correspond to the blazing condition for different wavelengths and different diffraction orders 31
2.14 Schematic representation of our optical system for comparison of the SLD with a laser, SLD spectra, images formed by SLD and laser 34
2.15 Square grating images with laser and SLD, their residuals and fits 35
2.16 Fidelity, contrast and quality of images formed with SLD and laser as a function of feature size 36
2.17 Quality of SLD and laser generated images as a function of distance from focal plane 37
2.18 Atoms captured in disordered potentials formed by SLD light 38
2.19 Evolution of atomic density under time varying potential fromed by SLD light . 40
2.20 Intensity and scattering rate at different wavelengths 41

3.1 Schematic of the experiment and signatures of the synthetic-dimension Bloch oscillations in real space 45
3.2 Bloch oscillation frequency and real space amplitude as a function of detuning . 50
3.3 Varying the shaking power to control the dynamics 52
3.4 Example Bloch oscillation in synthetic space 53
3.5 Bloch oscillation amplitude in synthetic space 54
3.6 Column density of shaken cloud 59
3.7 Time evolution of the integrated synthetic space density for varying conditions . 60
3.8 Cloud density with respect to λ for the low power parameters 62
3.9 Numerically-calculated matrix elements of the full Floquet Hamiltonian 63

4.1 Snapshots of the column density in the xy plane over time 70

4.2 Dendrogram for the hierarchical agglomerative algorithm for the same data as Fig.4.1 73

4.3 Maximum N_v of imprinted vortices that can generate clusters as a function of d and D 76

4.4 Cluster motion and effective cluster charge as a function of N_v 78

List of Acronyms

AOM Acousto-Optic Modulator.

BEC Bose-Einstein Condensate.

CCD Charge-Coupled Device.

COM Centre of Mass.

DMD Digital Micromirror Device.

FPGA Field Programmable Gate Array.

GPE Gross-Pitaevskii Equation.

MOT Magneto-Optical Trap.

NI National Instruments.

PID Proportional Integral Derivative.

RMS Root Mean Square.

SEM Scanning Electron Microscope.

SLD Super-Luminescent Diode.

SLM Spatial Light Modulator.

TA Tapered Amplifier.

TOF Time of Flight.

TTL Transistor-Transistor Logic.

VCO Voltage Controlled Oscillator.

List of Publications

Bloch oscillations along a synthetic dimension of atomic trap states

Christopher Oliver, Aaron Smith, **Thomas Easton**, Grazia Salerno, Vera Guarrera, Nathan Goldman, Giovanni Barontini, and Hannah M. Price

In: Physical Review Research 5 (5 July. 2023), p. 033001

doi: 10.1103/PhysRevResearch.5.033001.

Generation of optical potentials for ultracold atoms using a superluminescent diode

Aaron Smith, **Thomas Easton**, Vera Guarrera, and Giovanni Barontini

In: Physical Review Research 3 (3 Sept. 2021), p. 033241

doi: 10.1103/PhysRevResearch.3.033241.

Vortex clustering in trapped Bose-Einstein condensates

Thomas Easton, Marios Kokmotos, and Giovanni Barontini

In: Scientific Reports 13 (8 Nov. 2023), 19432

doi: 10.1038/s41598-023-46549-3.

Chapter 1

Introduction

The creation of the first optical dipole trap for neutral atoms in 1986 [1], and then the first magneto-optical trap in 1987 [2] kick started the field of cold atomic physics. Since then, rapid advances have been made, using a variety of techniques to further cool samples down to Bose-Einstein condensate [3, 4] or degenerate Fermi gas states [5], as well as producing traps for single atoms [6], traps for molecules [7], as well as lattice traps [8]. These experiments have lead to huge advances in our understanding of fundamental topics such as quantum turbulence [9] and ultra-cold chemistry [10]. Cold atoms have also been used as tools to probe nature, for example, they can be used as the basis for atom interferometers which are used to sense acceleration and gravity [11–13], and atomic clocks [14] which provide the most precise and accurate measurements so far achieved. Many searches for physics beyond the standard model use cold atoms and molecules as a starting point [15–17] due to the precision with which they can be controlled and measured, and the well developed understanding of the fundamental physics which governs their behaviour. Finally, cold atoms systems are frequently used as the basis for quantum simulations [18]. This term refers to any system which can be engineered to mimic the behaviour of another quantum system. For example, it is possible to engineer optical lattices such that trapped cold atoms will experience the same Hamiltionian as atoms in a condensed matter crystal [19, 20], but with parameters which can be tuned far more easily. As will be described in this thesis, quantum simulations can also be extended to situations which

cannot be easily implemented in other ways, for example simulations of systems in more than 3 spatial dimensions [21]. The trapping and manipulation of ultracold atoms is a key aspect to many of these applications. In some cases simple geometries such as harmonic wells and periodic lattices are sufficient, however in many cases more exotic trapping potentials unlock new physics, for example the physics of disordered crystals could be more easily simulated using non-periodic lattices. Full control over the potential experienced by the atoms, including the ability to dynamically alter it as a function of time enables a wide variety of new physics to be explored, such as the effects of rotating traps [22] or stirring of atomic clouds [23]. Finally, in the case of Bose-Einstein condensates, the phase of the order parameter can be precisely manipulated using carefully controlled potentials [24]. This can be used to generate arbitrary flows, opening yet another avenue of exploration. Recently, Spatial Light Modulators (SLMs) have become a widely used tool for the generation of spatially and temporally varying potentials [25–28].

1.1 Overview of Thesis

In this thesis I will detail the results of my research while working on the QPrint experiment. I will also describe the principles by which the experiment works, as well as the apparatus used to perform the research, including the existing equipment as well as the modifications that I have made during the course of the research project. The QPrint experiment is focused on the production of ultracold samples of ^{87}Rb and their manipulation using spatially and temporally controlled optical potentials generated using a type of Spatial Light Modulator (SLM) known as a Digital Micromirror Device (DMD). The apparatus is flexible enough to allow for multiple science goals. During my time on the project, the primary goal was to use the system to demonstrate a synthetic dimension of quantum harmonic oscillator states. Due to the COVID-19 pandemic, a substantial amount of time had to be spent outside of the laboratory, during which I developed simulations of vortex clustering dynamics in a system which could in principle be implemented on the QPrint apparatus via the method of phase imprinting in a Bose-Einstein

condensate (BEC). Beyond these, preliminary work was performed on a system to demonstrate the superfluid fountain effect in an atomic BEC. As this work was not completed, I will not present it in detail in this thesis, but I will present the principles as well as other potential avenues for the future of the project in the concluding chapter of this thesis.

The thesis is arranged as follows:

- **Chapter 1: Introduction** In the remainder of this chapter I will outline the key concepts required to understand this work, in particular the context and theory of optical potentials and how they can be used to perform phase imprinting, the concept of synthetic dimensions, and the idea of quantised vorticity in Bose-Einstein condensates.

- **Chapter 2: Experimental Apparatus** In this chapter I will describe the apparatus used in the experiment including the vacuum and laser systems, the traps used to confine and cool the atomic samples, the control systems and finally I will discuss the generation of optical potentials using the Digital Micromirror Device and the various light sources used with it.

- **Chapter 3: Implementation of Synthetic Dimensions with Atomic Trapped States** In this chapter I will describe the scheme used to produce a synthetic dimension of harmonic oscillator states in our system. I will then describe the particular experimental set-up used during this work, and then report the results showing the production of Bloch Oscillations. I will also briefly discuss the ways in which this scheme could be used to prepare samples in highly excited oscillator states.

- **Chapter 4: Simulations of Clustering Dynamics in Quantised Vortex Systems** In this chapter I will describe the theory underpinning the quantisation of vorticity and angular momentum in a BEC. I will then explain the simulation methods used to implement the Gross-Pitaevskii equation used to model the dynamics of a BEC. Next, I will report on the clustering behaviour that we have observed when beginning with a linear vortex structure, and finally I will describe the analytical models which can be used to describe vortex motion, and how these can be extended to models for the behaviour of clusters of vortices.

- **Chapter 5: Conclusions and Outlook** In this chapter I will conclude and describe the ways in which this work can be extended, as well as other avenues for research which this apparatus could address.

1.2 Bose-Einstein Condensates

The species which we use for our experiments is ^{87}Rb. Each atom is comprised of 37 protons, 50 neutrons and 37 electrons, and so is a composite boson. Because of this, it is possible for multiple atoms to occupy the same quantum state. When an energy state (usually the ground state) of a sample of atoms is macroscopically occupied, i.e. the number of atoms in that state is on the order of the total number of atoms in the sample, we say that the sample has undergone Bose-Einstein condensation, or is a Bose-Einstein condensate (BEC). This occurs when the phase space density is of order one,

$$P.S.D = \rho\lambda_T^3 \sim 1, \tag{1.1}$$

where ρ is the number density and λ_T is the thermal de Broglie wavelength. This can be achieved in the case of extremely high density, as is believed to be the case inside of neutron stars [29], but in a laboratory setting, the phase space density is increased by reducing the temperature, and thus increasing λ_T in an ideal gas. Bose-Einstein condensation occurs below a critical temperature, which is a function of the number of atoms and the trapping frequencies of the harmonic trap which the atoms are contained within. To first order, this is given by,

$$T_c = \frac{\hbar\omega_{ho}}{k_B}(N/\zeta(3))^{1/3}, \tag{1.2}$$

with ω_{ho} the geometric average of the trapping frequencies, N the number of atoms and $\zeta(x)$ the Riemann Zeta function. For temperatures between absolute zero (where all atoms would be in the condensate), and T_c, a portion of the atoms condense, while the rest of the cloud remains thermally distributed, according to the usual Bose distribution. This leads to a bimodal

distribution, both in real and in momentum space, with the condensed part appearing as a sharp peak in the centre of the cloud, with zero momentum. As a BEC is a highly degenerate system of many atoms in the same quantum state, it is convenient to model its behaviour using a complex function $\Psi(\vec{r}, t)$ which is known as the 'order parameter' or 'wave function of the condensate'. This can be thought of as the wavefunction of the highly occupied ground state. To high precision, it follows the famous Gross-Pitaevskii Equation,

$$i\hbar\partial_t\Psi = \frac{-\hbar^2}{2m}\nabla^2\Psi + U\Psi + g|\Psi|^2\Psi, \tag{1.3}$$

with m the particle mass, U the external potential, and $g = \frac{4\pi\hbar^2 a}{m}$ is a coupling constant which depends on the s-wave scattering length a. We normalise the equation so that $\int \Psi dV = N$, with N being the total particle number. For more information on trapped atomic Bose-Einstein condensates, see [30]. Though we avoid condensing the cloud by rapid evaporation in the work on generating synthetic dimensions, a condensate is required for any experimental implementations of our simulations work on quantised vortex dynamics, as well as many of the other projects which I will describe in chapter 5.

1.3 Optical Potentials in Cold Atoms

There are three ways in which cold neutral atoms can be trapped and manipulated: via radiation pressure, via the application of magnetic traps, and via optical potentials. Radiation pressure schemes such as the magneto-optical trap (MOT) have the great advantage of being able to trap and cool atoms from a thermal background to the micro-kelvin range. However, they have several disadvantages. First, there is a lower limit in temperature, namely the recoil energy. As these systems rely on the absorption and re-emission of light, the minimum momentum transfer is that of a single photon. The near resonant light can also induce a range of unwelcome effects, such as light assisted inelastic collisions which can limit the density that can be achieved. Because of this, radiation pressure traps are typically used for experiments where extremely low temperatures and high densities are not required, or as the first stage of a cooling process. Magnetic traps in which

a single state's field dependent energy is exploited by generating an inhomogeneous magnetic field again have several advantages and disadvantages. They produce conservative potentials, ideal for many applications, and can easily be used to perform evaporative cooling by resonantly transferring high energy atoms from the trapped to an anti-trapped state. However, these traps do require that the atoms stay in the trapping state, which reduces the available physics potential in cases where internal state is important, e.g. investigations of spinor condensates. They also have the major disadvantage of being difficult to engineer the shape of. The requirement to use fixed coils, as well as the complexity of calculating the geometry of a coil required to produce a given field configuration means that these traps are generally used for experiments requiring a simple and fixed trapping geometry, such as a simple harmonic oscillator potential. Finally, we have the optical potentials in which atoms experience an A.C. Stark shift and thus feel a potential proportional to the intensity of an off-resonant light field. These are not completely conservative, however they have the advantages of being extremely versatile in shape, allowing complex trap geometries and time varying potentials. Optical potentials can also be independent of the sub-level of the atom and thus allow for experiments in which the internal electronic state must be manipulated. In this experiment a radiation pressure based MOT is used to trap and pre-cool atoms, before they are loaded into a crossed optical dipole trap (i.e. a trap using the optical potential of two crossed high intensity beams). In this trap, they are evaporatively cooled and then held in a near harmonic trap. Finally, the experiment uses a shaped beam to produce spatially and time varying optical potentials on the cloud of atoms.

1.3.1 Theory of Optical Potentials

The following is a brief summary of the theory of optical potentials, as relevant to this work. A more complete description is given in [31].

A neutral atom in an oscillating electric field, $\vec{E}$ has an induced dipole moment, $\vec{p} = \alpha\vec{E}$, where α is the complex polarizability of the atom, and is a function of the frequency of the driving electric field. The interaction of the field with the induced dipole moment produces an

interaction potential,

$$U = -\frac{1}{2}\langle \vec{p}\vec{E}\rangle = -\frac{\mathrm{Re}(\alpha)I}{2\epsilon_0 c}, \tag{1.4}$$

where the intensity $I = 2\epsilon_0 c|\tilde{E}|^2$ is introduced. Similarly, the scattering rate is given by,

$$\Gamma_{sc} = \frac{\langle \dot{\vec{p}}\vec{E}\rangle}{\hbar\omega} = \frac{\mathrm{Im}(\alpha)I}{\hbar\epsilon_0 c}. \tag{1.5}$$

Using the following form for the polarizability,

$$\alpha = 6\pi\epsilon_0 c^3 \frac{\Gamma/\omega_0^2}{\omega_0^2 - \omega^2 - i\Gamma\omega^3/\omega_0^2}, \tag{1.6}$$

with Γ the natural linewidth, ω_0 the transition frequency and ω the frequency of the incident light gives us,

$$\begin{aligned} U &= \frac{3\pi c^2\Gamma}{2\omega_0^3\Delta} I \\ \Gamma_{sc} &= \frac{3\pi c^2\Gamma^2}{2\hbar\omega_0^3\Delta^2} I, \end{aligned} \tag{1.7}$$

where $\Delta = \omega_0 - \omega$ and Δ/ω_0 and Γ/Δ are both taken to be small. These approximations can be improved for a multilevel atom by treating the potential instead as a perturbation in the energy of the ground state. Using second order perturbation theory gives us the general equation for the shift in energy of an energy eigenstate,

$$\Delta E_g = \sum_j \frac{|\langle e_j|\hat{H}'|g\rangle|^2}{E_g - E_{e_j}}, \tag{1.8}$$

from which we get,

$$\Delta E_g = \sum_j \frac{|\langle e_j|\hat{\mu}|g\rangle|^2}{\hbar\Delta_j}|\vec{E}|^2, \tag{1.9}$$

where the interaction Hamiltonian $\hat{H}'$ is taken to be minus the electric field multiplied by the electric dipole operator, $-\vec{E}\hat{\mu}$ and the difference in energy is taken to be $\hbar\Delta_j$ with $\Delta_j = \omega - \omega_j$

is the detuning from the $|g\rangle \rightarrow |e_j\rangle$ transition. This is because one photon with energy $\hbar\omega_j$ is absorbed and the internal energy is increased by $\hbar\omega_j$. Finally, we can take the electric field's magnitude to be $|\tilde{E}|^2 = I/2\epsilon_0 c$ and the matrix element to be $\langle e_j|\,\hat{\mu}\,|g\rangle = \sqrt{\frac{3\pi\hbar c^3\Gamma}{\omega_j^3}}c_{gj}$, where c_{gj} are real transition coefficients depending on the particular atomic states, and the values of which can be found in the literature [32]. This gives us a perturbed energy which is position dependent via the intensity, and can thus be considered a potential. In the case of ^{87}Rb, we have

$$U(\vec{r}) = \frac{\pi c^2\Gamma}{2}\left(\frac{2}{\Delta_2\omega_2^3} + \frac{1}{\Delta_1\omega_1^3}\right)I(\vec{r}). \tag{1.10}$$

Note that the result has been divided by 3 to account for the fact that linearly polarised light only addresses one component of the dipole operator. Using the same matrix elements, one can calculate the scattering rate to be,

$$\Gamma_{sc} = \frac{\pi c^2\Gamma^2}{2\hbar}\left(\frac{2}{\Delta_2^2\omega_2^3} + \frac{1}{\Delta_1^2\omega_1^3}\right)I(\vec{r}). \tag{1.11}$$

Importantly, the potential scales inversely with detuning while the scattering rate, and thus heating rate, scales with the inverse square of the detuning. Therefore it is usually advantageous to use high intensity and large detunings in order to reduce the effects of photon scattering.

1.3.2 Phase Imprinting

It is possible to use optical potentials to modify the phase of the order parameter of a BEC as well as to modify its density. The prominent uses for this technique are the production of solitonic states, and the production of quantised vortices. Both of these states are examples of topologically protected states, in which the energy of the system cannot be reduced by smooth deformations of the condensate. In the case of a solitonic state in one dimension, the phase of the condensate's order parameter is stepped by π between 2 regions. The sharp change in the condensate phase between the to sides costs energy, but any smooth deformation would further increase the energy. Similarly in a vortex state, the phase is wound around a point. The variation in phase again costs energy, but the phase cannot unwind by any smooth deformation. The fact

that these states are topologically stable means that they cannot easily decay but also means that they cannot easily be generated by the evolution of the bulk condensate from a low energy configuration. In fact quantised vortices are made either in pairs when generated by dragging a defect through a cloud, or by nucleating on the boundary, as when a condensate is rotated. Phase imprinting using optical potentials allows topological configurations such as these to be generated by modifying the condensate in a way that isn't a smooth deformation, but rather a sudden jump in the phase. This can be controlled accurately using precisely shaped potentials, allowing for arbitrary vortex configurations, for example, to be produced. I will now briefly explain the mechanism behind phase imprinting.

As mentioned above, a BEC follows the Gross-Pitaevskii equation (GPE),

$$i\hbar\partial_t\Psi = \frac{-\hbar^2}{2m}\nabla^2\Psi + U\Psi + g|\Psi|^2\Psi. \tag{1.12}$$

We can then introduce the number density ρ and phase ϕ of the order parameter via the Madelung transformation,

$$\Psi(\vec{r},t) = \sqrt{\rho(\vec{r},t)}e^{i\phi(\vec{r},t)}. \tag{1.13}$$

Substituting this into the GPE gives the following coupled differential equations for the density and phase,

$$\begin{aligned}\dot{\rho} &= -\frac{\hbar}{m}\nabla\cdot(\rho\nabla\phi)\\ \dot{\phi} &= -\frac{\hbar|\nabla\rho|^2}{8m\rho^2} + \frac{\hbar\nabla^2\rho}{4m\rho} - \frac{\hbar|\nabla\phi|^2}{2m} - \frac{U}{\hbar} - \frac{g\rho}{\hbar}.\end{aligned} \tag{1.14}$$

if we identify $\vec{v} = \frac{\hbar}{m}\nabla\phi$ as the velocity, the first line of this is simply the continuity equation. Notably, this equation doesn't directly involve the external potential U. Therefore, changes to the particle density occur only via changes in the phase. Because of this, a rapid change in the potential primarily affects the phase of the condensate, rather than its density. Therefore if we

change U to some U' for a short time interval Δt, the phase will change to

$$\phi'(t + \Delta t) \approx \dot{\phi}\Delta t - \frac{U'\Delta t}{\hbar}, \tag{1.15}$$

where $\dot{\phi}$ is taken to be without the modification to the potential. If Δt is small compared to the timescale associated with the unperturbed cloud, i.e. $\Delta t \partial_t \Psi_{unperturbed} \ll 1$, the density will not change appreciably over this time. If the condensate was originally in its ground state, then $\dot{\phi}$ is not a function of position (as the ground state is by definition a stationary state), however U' is an applied potential, which we can choose to be spatially inhomogeneous. As noted above, the condensate velocity is proportional to the gradient of the phase, so by modifying the phase of the condensate in this way, it is possible to produce arbitrary flows by using a brief flash of a shaped optical potential,

$$\Delta\vec{v}(\vec{r}) \approx -\frac{\nabla U'(\vec{r})\Delta t}{m}. \tag{1.16}$$

This approximation is better for smaller imprinting times, which require higher potential gradients to produce the same flows.

1.4 Synthetic Dimensions

The introductory material in this section includes parts that have been published in the paper: C. Oliver, A. Smith, T. Easton, G. Salerno, V. Guarrera, N. Goldman, G. Barontini, and Hannah M. Price "Bloch oscillations along a synthetic dimension of atomic trap states", published in Physical Review Research. Some of this material remains largely unchanged, others has been made more appropriate for the thesis.

'Synthetic dimensions' is the name given to a wide range of schemes in which degrees of freedom in a system are coupled together so that they can be treated mathematically as though they were an extra dimension of physical space. Typically this is done by coupling discrete states so that there is a notion of adjacency between states, i.e. states which are to be close in

the synthetic dimension are coupled strongly and more distant states only weakly if at all. The use of discrete states means that the synthetic dimension is typically best thought of as a lattice rather than a continuous dimension.

Synthetic dimensions provide a powerful approach for simulating condensed matter physics in cold atoms [33–46] and photonics [47–50], and they are opening up many new avenues for simulating and exploring exotic physics, including quantum Hall ladders [34, 40, 41], non-Hermitian topological bands [51], topological Anderson insulators [52], and even lattice physics in four dimensions or higher [33, 35, 53]. A key reason that this framework is so powerful is that it is very general, and can be applied to a wide-range of very different physical systems. For example, synthetic dimensions have so far been realised experimentally in cold atoms with hyperfine [33, 40, 41], magnetic [44], Rydberg [45, 46], and clock states [42, 43], as well as with momentum [34, 35], orbital [38] and superradiant states [36]. However, in these experiments, the size of the synthetic dimension has been so far limited by the number of states that can feasibly be coupled. Indeed, the largest momentum state lattice [54] employed so far consists of a 1D lattice of 21 sites.

Notably, it has been recently realised that such limitations can be lifted if external degrees of freedom associated with trapping potentials are used to generate the synthetic dimensions [47, 55, 56]. Indeed, trapping potentials typically allow for tens or hundreds of trapped states in each direction, and by suitably coupling them one could implement very long synthetic dimensions, unleashing the full potential of this technique for quantum simulation. Additionally, this kind of synthetic dimension is extremely appealing because it provides a framework for the manipulation and control of trap states. A range of applications including quantum simulations in optical lattices [57–59], trapped and guided atom interferometry [60–62] and quantum thermodynamics [63–65] require the use of highly-excited trapped states, which are generally difficult to realise with a good degree of precision and control.

In chapter 3, I will describe how we experimentally engineered a very long synthetic dimension of many tens of atomic trap states by dynamically modulating the harmonic trap of an ultracold atomic sample [55, 56]. By controlling the driving frequency we generated a

force along the synthetic dimension that induces Bloch oscillations, which act as a smoking gun signature that the synthetic dimension behaves as expected. Bloch oscillations were first famously predicted for electrons moving in a crystal under an electric field, and have since been observed in various setups, including optical lattices for cold atoms [66], as well as synthetic dimensions of photonic frequency modes [67] and of room-temperate molecular angular momentum states [68]. However, Bloch oscillations in our experiment are physically very different from previous realizations, as they correspond to atoms periodically oscillating between low- and high-energy states of the harmonic trap. As such, another benefit of the synthetic dimension Bloch oscillations implemented here is that they allow us to explore highly-excited harmonic states, and thus can lead towards a novel approach for quantum engineering of external atomic states. More generally, this work paves the way for the exploration of higher-dimensional quantum Hall physics with artificial magnetic fields, and opens new opportunities in quantum simulations more widely. For example, a tunable artificial gauge field can be implemented by spatial modulation of the phase of the driving potential, allowing access to 2D quantum Hall physics.

1.5 Quantised Vortices

The introductory material in this section includes parts that have been published in the paper: T. Easton, M. Kokmotos and G. Barontini "Vortex clustering in trapped Bose-Einstein condensates". This has been submitted for publication in Scientific Reports. Some of this material remains largely unchanged, others has been made more appropriate for the thesis.

The notion of vortices and vorticity is ubiquitous in physics, as it appears in classical physics, e.g., in hydrodynamics, gravitational physics, electromagnetism [69] and non-linear optics [70], as well as in in the quantum realm, through quantum turbulence and quantum hydrodynamics in superfluids [71] and superconductors [72].

A vortex in a quantum system such as a Bose-Einstein condensate is a topological defect which carries one or more quanta of angular momentum [73]. In a 3D system, these defects are

1D curves which can tangle and support waves (known as Kelvin waves) along their lengths. In a 2D system these lines reduce down to point-like objects. These point-like vortices can still undergo complicated dynamics. In particular, vortices which carry more than one quantum of angular momentum are unstable, and tend to decay. On top of this, when multiple vortices interact, they may form bound structures.

Bound structures such as vortex-vortex or vortex-antivortex pairs have been created in BECs [74–77] and predicted in ultracold Fermi gases [78]. In the optical regime, vortex cluster formations have also been demonstrated in microcavity exciton-polariton condensates [79]. The processes and parameters that lead to the formation of vortex clusters rather than, e.g., turbulence or disorder, are however less understood and investigated.

Atomic BECs are a good platform for the generation and study of vortex clusters and their dynamics due to their extensive controllability in the experiments [80] and the wide availability of tools for numerical simulations both at zero [81] and finite temperature [82, 83]. In trapped BECs, the vortex dynamics are dictated by density and phase gradients of the superfluid background. The gradient of the background density created by the trapping potential induces a precession of the vortex about the centre of the trap. In addition, each vortex creates a velocity field that affects the motion of the other vortices similarly to the way seen in fluid physics. This can be seen as a vortex-vortex interaction that depends on the separation of the vortices as well as their topological charges [84]. It can lead to a rotational motion where the vortices rotate around each other, or a linear motion where the vortices travel in parallel. The combination of these effects is at the core of the formation of vortex clusters, turbulence or vortex lattices.

For what concerns vortex clusters, the many features of trapped BECs are ideal to gain precious insight, both in real experiments and in numerical simulations, on the dynamics of the clusters formation and the conditions for their existence and stability. Numerical simulations on these clusters will be explored in chapter 4.

Chapter 2

Experimental Apparatus

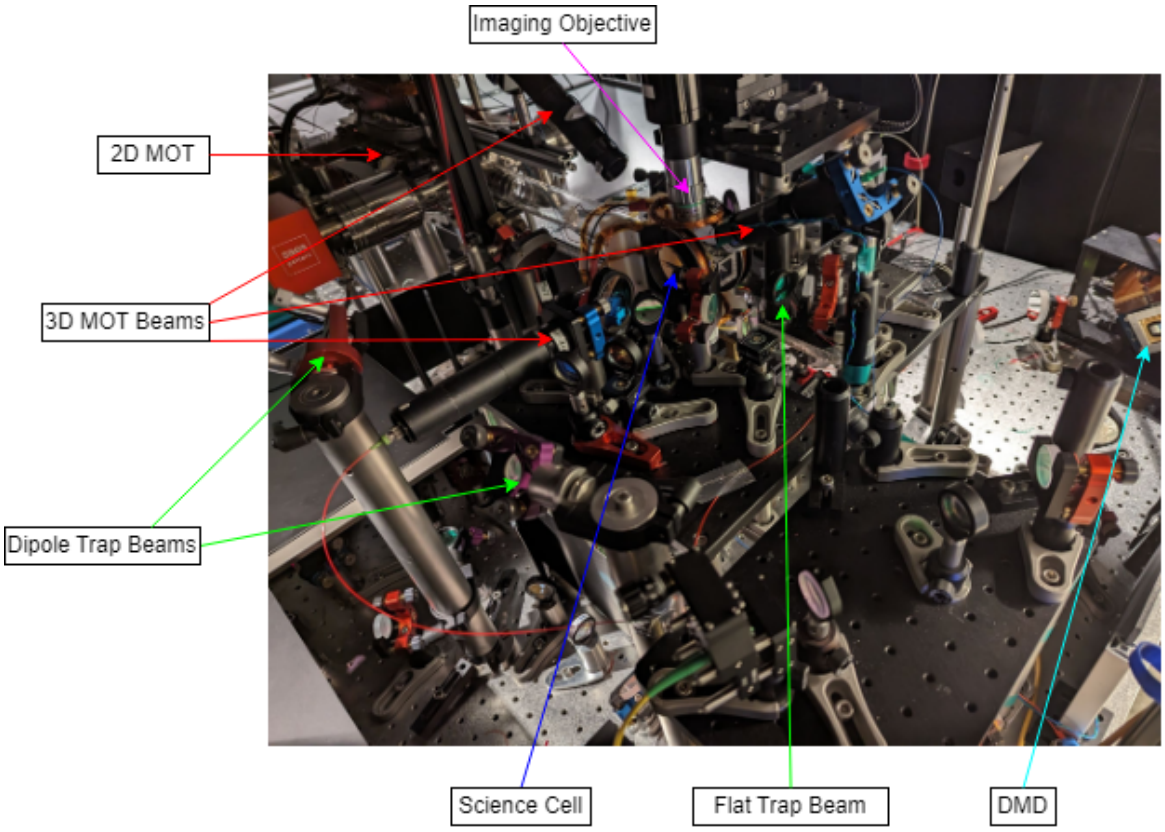


Figure 2.1: Image of the experimental apparatus labelled with some of the key components.

In this chapter, I will summarise the main components of the experimental apparatus in order to contextualise the rest of the work. While the experiment was originally built in 2017[85] to investigate the physics of spinor condensates, there have been changes made to almost every

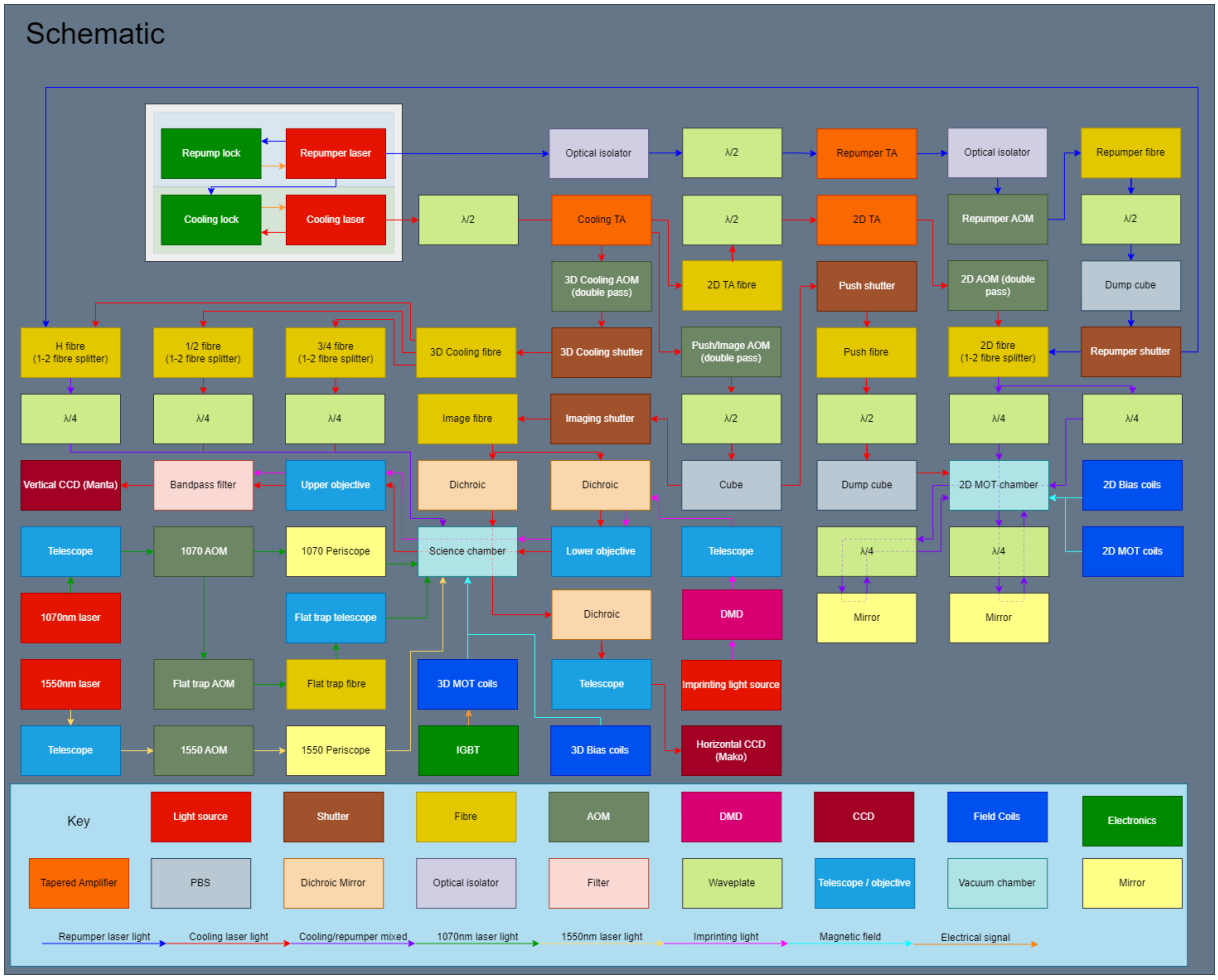


Figure 2.2: Schematic showing the connections between the various components of the apparatus, focussing on the optics. Note that this diagram is not representative of the positions of components in physical space, and mirrors used simply to redirect optical paths around the bench are omitted. For detail on the locking electronics, see Fig.2.4

.

aspect of the setup since. For completeness, I will touch on all of the major elements of the setup, but I will focus on those areas which I have directly modified. A summary of the connections between the various components of the apparatus is shown in figure 2.2.

2.1 Vacuum System

The vacuum system is broken into 2 separate chambers, the 2D MOT chamber, at a pressure of $\approx 10^{-7}$ mbar and the science chamber, at $\approx 10^{-10}$ mbar. These are connected by a small tube 21 mm of length and 1.1 mm diameter, which allows for the pressure difference to be maintained.

The 2D MOT chamber is kept at the higher pressure to increase the rate of atom loading, as this is the chamber where atoms are initially loaded into a trap and pre-cooled. The science chamber, where we reach BEC temperatures must be at the lower pressure in order to limit the rate of collisions between ultracold trapped atoms and room temperature background gas atoms.

2.2 Optical Setup

2.2.1 Lasers & Laser Locking

The 780 nm light for the MOTs is provided by 2 Toptica DL Pro lasers, one for the cooling light, and one for the repumper light. In order for the wavelengths of these lasers to stay correct for the MOT, they must be locked via active feedback loops. This is summarised in figure 2.4. The relevant energy levels are detailed in figure 2.3.

The repumper is kept at a constant frequency, on resonance with the $F = 1 \rightarrow F' = 2$ transition of the D2 line. It can therefore be easily locked to a saturated absorption spectrum generated by retro-reflecting 300 µW through a cell containing ^{87}Rb vapour, then directing it onto a fast photodiode. On the first pass of the light through the cell, atoms are excited when the laser is close to the resonant frequency, creating an absorption trough. This feature is Doppler broadened, as each velocity class of atoms sees a different wavelength (in the lab frame) as resonant. On the reverse pass excited atoms which are stationary in the direction of laser propagation are stimulated to emit. This is because only atoms which see the laser as having the same frequency in both passes are excited and then stimulated. This creates small peaks in the large trough. As well as peaks corresponding to each transition, there are so called 'cross-over' peaks, at the midpoint between each pair of transitions. These occur because there will always be a velocity class such that one transition is resonant on the 1st laser pass, and the other is resonant on the second laser pass. As we wish to use an AOM to modulate the power of the repumper beam, and AOMs shift the frequency of the light, we choose to lock to the $F = 1 \rightarrow F' = 1$CO2 cross-over peak, and choose the AOM frequency to be 78.47 MHz, which is equal to the detuning between the crossover and the $F = 1 \rightarrow F' = 2$ transition. The

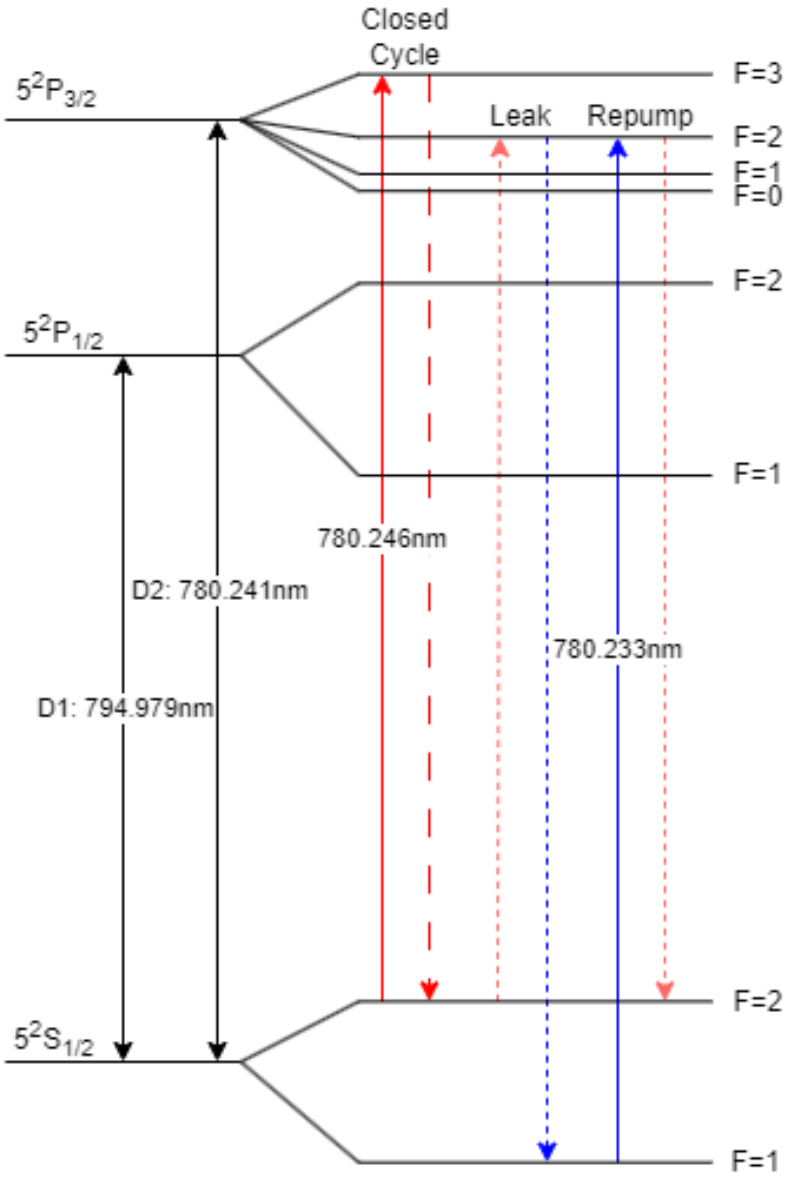


Figure 2.3: Hyperfine structure for the $5^2S_{1/2}$, $5^2P_{1/2}$ and $5^2P_{3/2}$ levels (not to scale). Arrows denote relevant transitions, with the red and blue solid arrows corresponding to exciting the atoms with the cooling and repumper beams respectively. The wide-dashed red arrow indicates the deexcitation of atoms which remain in the closed cycle. The dashed upward arrow shows the path by which atoms can be 'accidentally' excited into the $F' = 2$ state. The remaining two arrows show the paths that atoms in this excited state can take. Without the repumping beam, all atoms would collect in the $F = 1$ lower ground state. This is exploited in the dark MOT stage (see below), to avoid loss of atoms by collisional deexcitation.

spectrum, as seen by the photodiode is passed to the laser control box, where it is dithered to generate an error signal, and then a PID loop is used to lock the laser to the peak by adjusting its piezo voltage.

The cooling laser has a variable detuning over the course of the sequence, so it is offset locked to the repumper with a variable offset. This is accomplished by overlapping 5 mW of each laser onto another photodiode, connected to a bias tee. This produces a beat signal with frequency components at the sum and difference of the two laser frequencies. This is then passed through a low pass filter to remove the sum of the frequencies, then it is mixed with an RF local oscillator frequency. Again, the output contains the sum and difference of these two frequencies, so it is once again passed though a low pass filter, before being compared to a standard reference frequency to produce an error signal. This is done by splitting the signal into two branches, one being passed through a high-pass filter with a forward facing diode, while the other is passed through a fixed 3 dB attenuator with a reverse facing diode. These branches are then combined again after more low pass filtering to bring them close to DC. The sum of voltages will then be positive or negative depending on whether the filter attenuates more or less than the fixed attenuator. These will attenuate at the same level for a signal at 171 MHz. Again, this error signal is fed into the Toptica laser control box, which uses a PID loop to adjust the piezo voltage to keep the laser locked to the desired frequency. In order to vary the frequency offset of the lock during the sequence, the local oscillator's frequency is modified. Due to a lack of availability of standalone VCOs at the required frequency, the signal is produced by a synthesizer (EV-ADF5356SD1Z), with a reference frequency provided by a function generator, which is in turn frequency modulated by an analog signal from the control computer.

The above description is of the current setup. Over the course of the project, due to degrading lasers the scheme was changed from one involving a master laser which was spectroscopy locked, along with two slave lasers (cooling and repumper), which were both individually beat locked. The new setup is simpler and more efficient, requiring only 2 lasers, and also uses the laser control box to provide the PID loops, rather than external systems as were in the previous system.

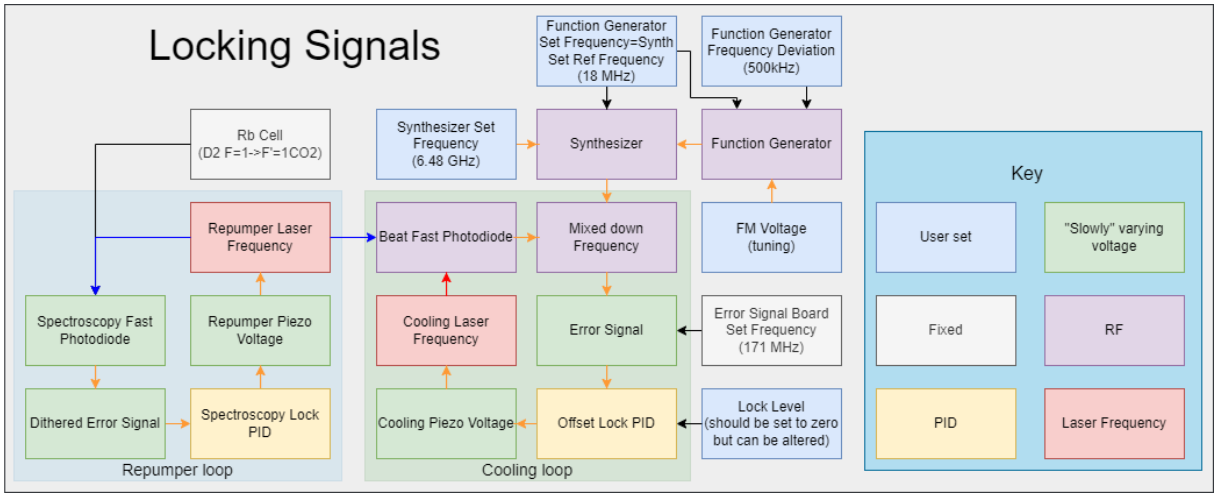


Figure 2.4: Schematic showing the connections between the various components of the laser locking system.

2.2.2 Imaging Systems

Our setup includes two absorption imaging systems. The first images the atoms along the horizontal direction, typically at a time-of-flight of 25 ms, with a total magnification of 2.7. This is used for measuring the atom number, temperature and condensate fraction of the cloud. It also has the potential to be used in some future measurements, particularly those involving the fountain effect (see chapter 5). The second imaging system images along the vertical direction via a series of 2 microscope objectives, one to focus light onto the atomic sample, and one to form an image. This has a much higher magnification which can be modified by swapping between various microscope objectives, but is typically 20×. This system is useful as it images along the same optical path as the imaging light, allowing us to see dynamics in the same plane as the potential we generate, and has a resolution of around 2 µm.

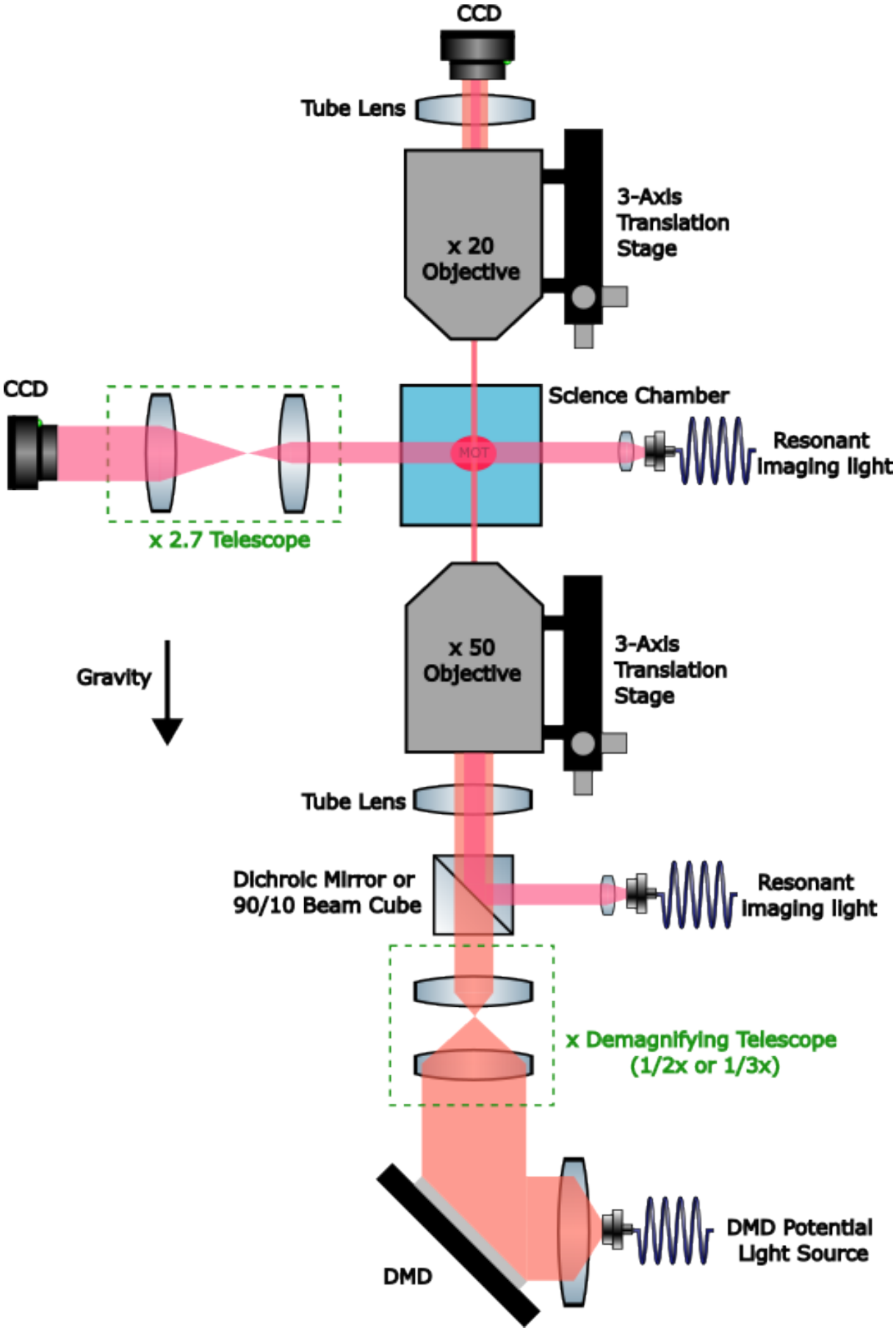


Figure 2.5: Schematic showing the components of the imaging systems, along with the path along which imprinting light is sent from the DMD (see section 2.6).

2.3 Magneto-Optical Traps

The first step in producing our ultracold atomic samples is to trap and cool the atoms within magneto-optical traps. This is a commonly used technique in cold atoms physics which allows us to take 10^9 room temperature atoms from the background gas and trap and cool them down to $350\,\mu\text{K}$.

2.3.1 Working Principle

In a Magneto-Optical Trap (MOT), light which is red-detuned from a resonance is incident on atoms. The atoms can absorb the light, gaining its momentum, $\hbar\omega$ in the direction of the beam's propagation. The atom can then lose the gained energy in one of 2 ways, either by spontaneous emission, or by stimulated emission. If the atom undergoes stimulated emission, it loses the momentum it gained, and there is no net change of momentum in the process. If on the other hand, it undergoes spontaneous emission, it gains another momentum kick of $\hbar\omega$ in a random direction. After many cycles, these directions average out, meaning that the atom gains a net momentum change in the direction of the beam's propagation due to the absorption. Because the light is red-detuned from the transition, the atom sees it doppler shifted towards the transition when it travels towards the light source, and doppler shifted away from the transition when it is moving away from the light source. This means that the probability of absorption is increased for atoms moving towards the light source compared to those moving away from it. As the average momentum kick is in the direction of light propagation, this has the effect of slowing atoms which move towards the beam. By using 6 beams of light, one for each face of a cube, this slowing can apply to atoms moving in any direction. This configuration is known as optical molasses as the force acts similarly to a friction or drag force, slowing any particle regardless of its momentum. As this configuration slows the random motion of atoms it has a cooling effect, however the force is homogeneous and so cannot trap atoms. In order to add trapping to optical molasses, a quadrupole magnetic field is applied, typically using a pair of coils in anti-helmholtz configuration. This causes a zeeman split in the atomic transitions proportional to the distance

from the centre of the coils. By using light which is σ^- polarised, light only addresses the zeeman level which is reduced in energy when the field strength is increased. This has the effect of increasing the transition probability, and therefore force, as distance from the centre increases, thereby introducing a restoring force. This configuration is known as the magneto-optical trap.

2.3.2 Experimental Implementation

We use the closed cycle in the D2 line, i.e. $F = 2 \rightarrow F' = 3$. This is known as a closed transition because for atoms in the $F' = 3$ state the only allowed transition is to decay back to the $F = 2$ state, and so atoms should, in theory, never leave the cycle of $F = 2 \rightarrow F' = 3 \rightarrow F = 2$. However, the atoms have a finite probability of instead undergoing the $F = 2 \rightarrow F' = 2$ transition instead of the intended $F = 2 \rightarrow F' = 3$. They can then decay into the lower ground state $F = 1$. We therefore also use a repumping beam resonant on the $F = 1 \rightarrow F' = 2$ transition, in order for these atoms to then be able to decay into the $F = 2$ ground state and thus reenter the cooling cycle. We have two stages of MOT, first a 2D MOT, which uses a pair of retro-reflected σ^- polarised beams, at a power of $85\,\mathrm{mW}$, with a cooling to repumper power ratio of $2:1$. These beams are expanded in one direction using cylindrical lenses. This allows us to produce a cigar-shaped trap. The large extent of this trap allows for the trapping of significantly more atoms than could be done in a 3D MOT. The 2D MOT is then transferred via the resonant push beam into the science cell where it is collected by the 3D MOT.

The 3D MOT is formed from 3 pairs of counter propagating σ^- beams with $5\,\mathrm{mW}$ of cooling light in each beam. The repumper need not be isotropic so we choose to only supply $5\,\mathrm{mW}$ of it to the horizontal pair. In order for the imprinting light to propagate in the vertical direction, 2 pairs of MOT beams are rotated 45° from vertical. Over $5\,\mathrm{s}$ of loading from the 2D MOT into the 3D MOT, we are able to capture 10^9 atoms and cool them to $350\,\mu\mathrm{K}$. This temperature is still higher than the dipole trap's depth, as so we use a dark MOT stage to reduce the temperature down to $50\,\mu\mathrm{K}$. This involves further red-detuning the cooling light to favour cooling over trapping, while reducing the intensity of the repumping light to reduce the number of scattering events. This also means that at the end of the dark MOT, the atoms are all able

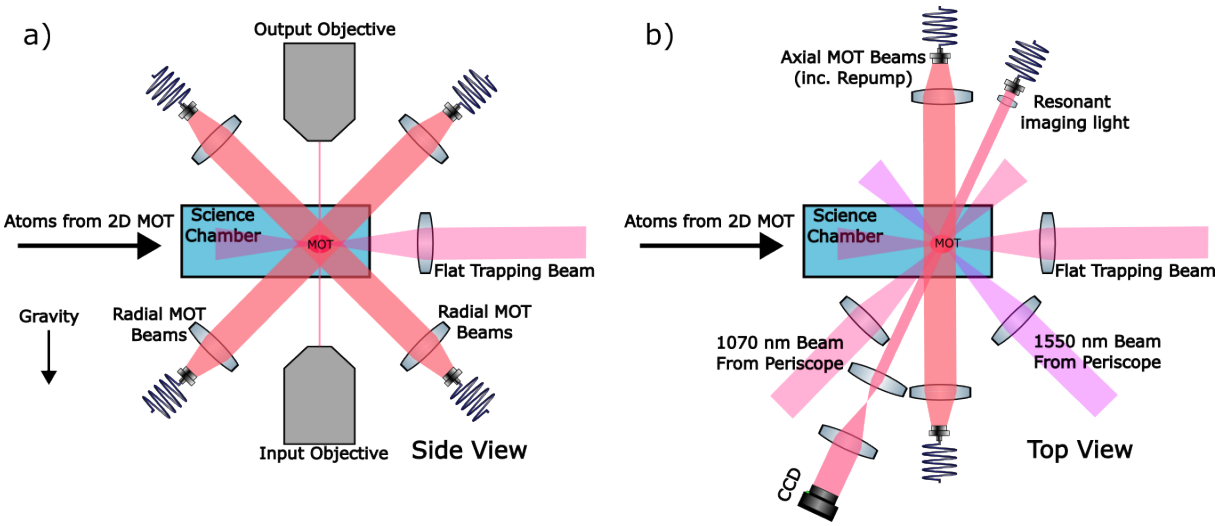


Figure 2.6: Schematic diagram of the various laser beams around the science chamber. a) Cut-through view from the side. Atoms arrive from the 2D MOT via resonant push beam from the left. The radial MOT beams are arranged at 45° from vertical to allow room above and below the chamber for microscope objectives which are used for imaging and projecting the imprinting light (see sections 2.2.2 and 2.6. b) Cut-through view from above. The axial MOT beams, which include repumping light, crossed dipole beams (section 2.4.1), flat trap beam (section 2.4.2) and horizontal imaging beam (section 2.4.2 all lie in the horizontal plane.

to fall into the lower ground state, so that they can no longer undergo collisional deexcitation which would otherwise be a major atom loss channel.

2.4 Optical Dipole Trap

As MOT works on the principle of absorption and re-emission of photons, the minimum possible temperature it can reach is the recoil temperature, corresponding to the recoil energy, i.e. the kinetic energy an atom gains by emitting a single photon. In order to reach colder temperatures and higher phase space densities, the atoms are loading into a crossed optical dipole trap. This trap works on the same principle as the optical potentials that are applied on the final samples, i.e. the A.C. Stark effect. In brief, the rapidly oscillating electric field of the applied laser light shifts the energy levels of the atom depending on the detuning from resonances and the power of the beam. The energy levels are shifted lower in the presence of light which is red detuned, and therefore by using a red-detuned beam with a gaussian profile, the atoms feel a force towards the highest intensity region of the beam, i.e. its centre.

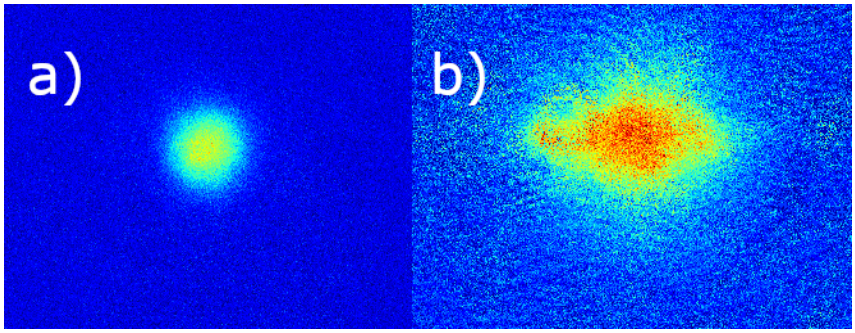


Figure 2.7: Absorption images of a typical cloud. a) From the horizontal imaging system after 25 ms time of flight expansion. b) From the vertical imaging system without time of flight expansion.

2.4.1 Crossed Optical Dipole Trap

Using a focussed beam means that there is trapping not only in the transverse direction, but also in the axial direction. This can be used to create a trap on its own, however in order to produce tighter confinement in this direction, as well as to have more control over the relative trapping strengths in each direction, we produce a crossed optical dipole trap, in which 2 high power red detuned beams are overlapped to produce tight confinement in every direction. We use a 1070 nm laser at 20 W with waist 26 µm and a 1550 nm at 10 W with a waist of 53 µm. Both pass through AOMs to allow for their power to be adjusted duing the experimental sequence. In order to reduce the temperature of the cloud, we can then employ evaporative cooling by reducing the power of the beams. This allows the highest energy atoms to leave the trap, and if it is done slowly enough, the atoms can rethermalise to a lower temperature before the next highest energy atoms leave the trap, and so on. During this process we lose $\sim 99\%$ of the atoms, but the remaining ones can be as cold as 20 nK. The atoms occupy the centre of the beams, so we are free to approximate the gaussian profiles as quadratics, and can therefore treat the trap as harmonic. By adjusting the ratio of powers of the two beams, we are able to achieve a range of trapping frequencies, but typically use $\sim (10, 100, 100)$ Hz. At these temperatures, this causes the atoms to undergo Bose-Einstein condensation. A typical evaporation ramp involves the 1070 nm beam from $\sim$ 12.4 W to 0.1 W over 7.875 s with the 1550 nm beam switched on at $\sim$ 3.9 W 275 ms into the process, with it ramping down in power to $\sim$ 0.05 W for the final 6.7 s of the evaporation.

2.4.2 Flattened Trap

We have also implemented a flattened trap beam to allow us to produce clouds with a very high trapping frequency in the vertical direction. This was achieved by extracting one of the unused orders from the 1070 nm trapping beam's AOM and passing it through its own AOM for power control, before fibre coupling it to the level of the science cell. The beam is then passed through a series of lenses including a pair of cylindrical lenses which produce a beam with a very small waist of 11 µm in the vertical direction with a large waist of 390 µm in the horizontal direction. A diagram of the optical setup for the flattened trap is shown in figure 2.8. The top panel of this figure shows the original design for the optics, which has the vertical and horizontal waists coinciding. This produces a large trap depth at the focal point. However we found that by moving the final cylindrical lens by 4 mm, we could displace the horizontal waist, providing a much higher trap aspect ratio. This is shown in the lower panel of figure 2.8.

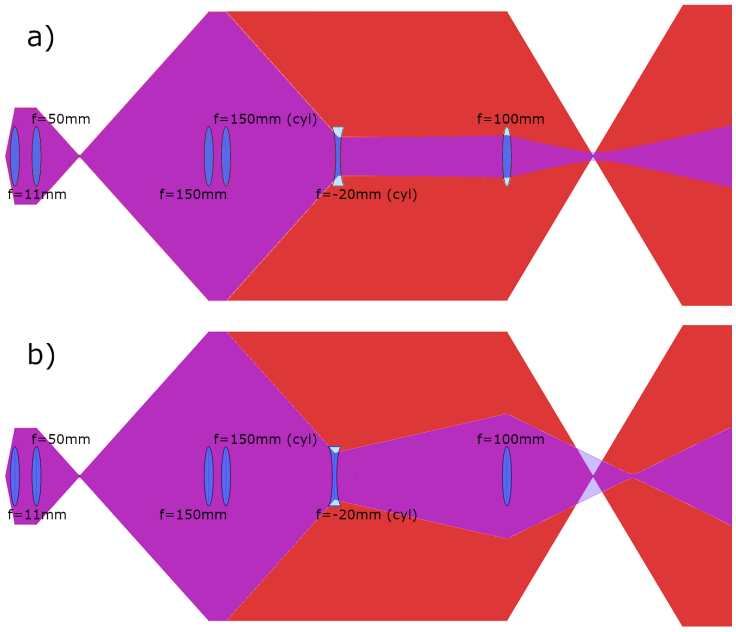


Figure 2.8: Simulations of the beam propagation through the flat trap optics after exiting the optical fibre. Purple shows the horizontal component of the light, while red shows the vertical. a) The original design with the two focci coinciding. b) The same configuration but with the final cylindrical lens moved by 4 mm. This has the effect of displacing the horizontal focus and giving a much wider horizontal beam diameter at the position of the vertical waist.

We determined that when used in conjunction with one or more of the other dipole trap beams, there was still a high enough trap depth to contain an atomic sample, and were able to

observe aspect ratio inversion in time of flight imaging, a 'smoking gun' indicator of a BEC in a non-isotropic trap.

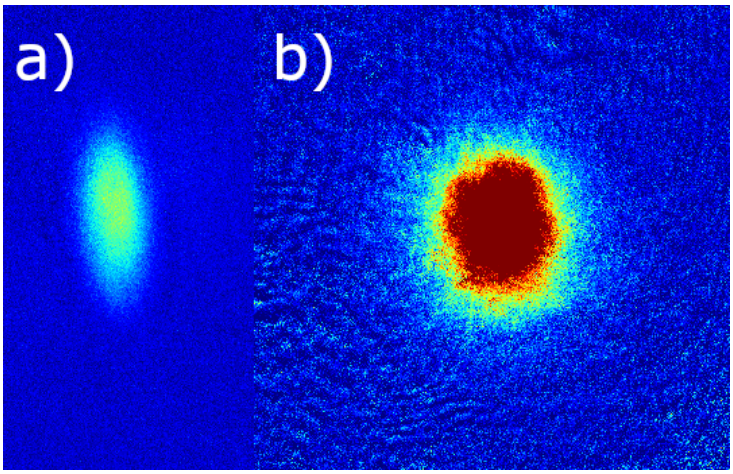


Figure 2.9: Images of the flattened trap. a) Image taken using the horizontal imaging system after 25 ms of time of flight. It is clear to see the aspect ratio inversion from the 'pancake shaped' cloud formed in the trap to the 'cigar shaped' cloud reached after dropping for 25 ms. This is a clear indication that we have produced a BEC in the flat trap. b) A picture of the same cloud from the vertical imaging system. We can see that the cloud is relatively round in the horizontal plane. Note, the blue circular disc corresponds to the aperture of the microscope objective.

The purpose of the flat trap beam was intended to be to generate clouds such as those described in the work on simulations of vortex dynamics (see chapter 4), however when the 1550 nm laser broke, the flat beam could be used to allow measurements to still be taken by using it as the weaker cross beam until the 1550 nm could be repaired.

2.5 Sequence Control

We use Cicero Word Generator/ Atticus[86], along with a National instruments PXIe-1062Q chassis containing a PXIe-8360 card, a PXI-6713 card and a PXIe-6535 card. These are attached to breakout boards with current buffers, allowing us to produce analogue and digital signals. We use a variable timebase generated using an Opal Kelly XEM3001 FPGA which allows us to produce samples at up to 1 MHz where needed, but to produce them at less than 1 Hz in longer stages with few changes, so that we don't overfill the buffers on the National Instruments (NI) cards. An example of an experimental sequence as seen in Cicero is shown in figure 2.10.

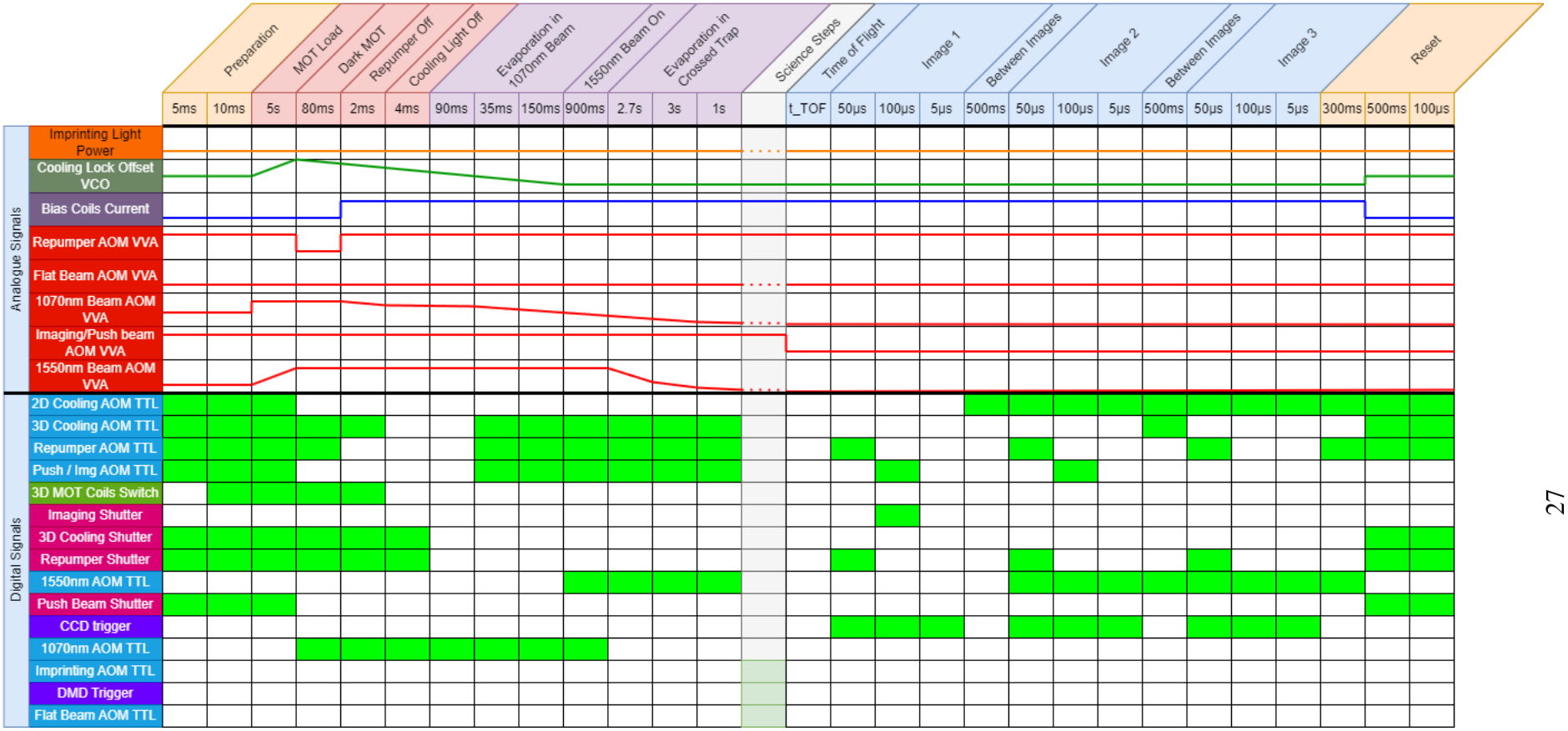


Figure 2.10: Diagram of the analogue and digital signals for a typical experimental sequence. The sequence is broken up into time steps (columns), of varying durations given by the time at the top of each time step. Each row is a different analogue or digital signal generated by the NI cards. The top 8 rows are analogue, and a trace is shown for each of these describing how the analogue value changes through a sequence. The bottom 15 rows are digital signals, and are either marked as green or white in each timestep, with green signifying the 'on' state and white signifying the 'off' state. The time steps corresponding to the particular science stages (e.g. modulating the cloud for a synthetic dimensions measurement or taking a measurement of the trap frequencies) are omitted and replaced with a grey column, as these steps vary greatly. In this column, analogue signals which might be used are denoted with a dotted line, and digital signals which may be used are in a dull green.

2.6 Optical Potentials

The above apparatus allows for the generation of ultracold atomic samples. The purpose of generating these is to then manipulate them using optically generated potentials. In this section I will describe how these are generated, first by describing the digital micromirror device and the related optics. Next I will discuss the various light sources used. We originally made a comparison between a tuneable Toptica DL Pro laser and a superluminescent diode (SLD), which showed favourable results for the SLD in regards to the generated image quality. It was decided, however that it would be advantageous to perform many of the experiments using repulsive potentials, which can only be produced by blue detuned light, and that the tuneable laser was preferable. Towards the end of the project, it was determined that the heating effect of the tuneable laser was too high for some experiments which involved longer projection times. We therefore implemented a red laser with a much higher power and a much larger detuning from resonance.

2.6.1 Digital Micromirror Device

We use an DLP9500 digital micromirror device. It is formed of an array of 1920x1080 micromirrors, each with a side length of 10.8 µm. The device has a refresh rate of 10 kHz. The DMD accepts data in the form of black and white bitmap images with a bit depth of 8 per channel. We are able to supply the DMD with a folder of such images, and can proceed from one image to the next by supplying a TTL signal. This can either be done directly from the control system, or we can use a function generator to supply signals at a fixed frequency, gated by a digital signal from the control system. While it is convenient to picture the DMD as a mask, simply directing light incident on the 'on' pixels in one direction the 'off' pixels in another, the system is actually more complex. As the DMD is a uniform array of many identical optical elements, it must also be considered as an optical grating, and diffraction effects are important. In particular, the light incident on the DMD is split among many diffraction orders, and the efficiency of the reflection depends strongly on the angles of incidence and reflection, as well as the wavelength of the light.

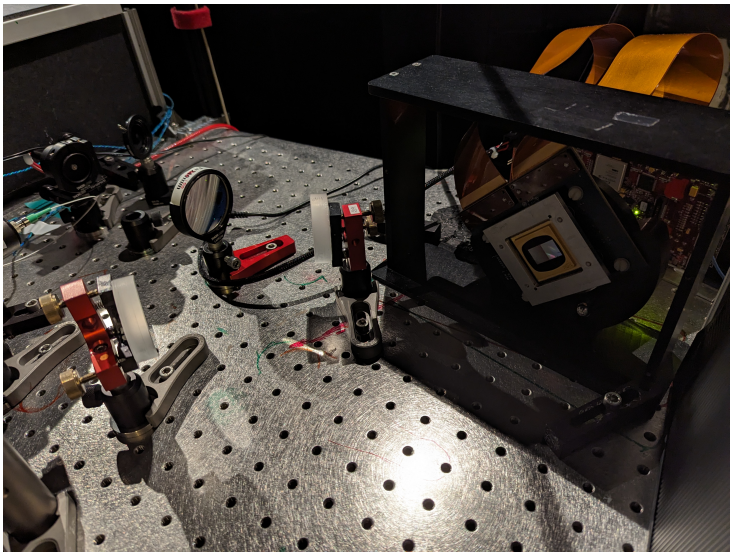


Figure 2.11: Image of our DMD in position. In the background are the optics for the red laser (see below).

A reflective diffraction grating obeys the equation,

$$m\lambda = d(\sin\alpha - \sin\beta), \tag{2.1}$$

where m is an integer determining the diffraction order, λ is the wavelength of light, d is the grating spacing and α and β are the input and output angles relative to the diffraction grating normal, as shown in figure 2.12. This equation accounts only for the effects of coherent interference.

Clearly, we will see improved efficiency if the angles are chosen so that the path also corresponds to specular reflection. This gives us the additional constraint that,

$$\alpha - \theta = \beta + \theta, \tag{2.2}$$

where θ is the angle of the micromirrors, as defined in figure 2.12. When both of these conditions are met, the diffraction is said to be 'blazed'. Using trigonometric identities we can see that equations 2.1 and 2.2 lead directly to,

$$\frac{m\lambda}{2d} = \sin\theta\cos(\alpha - \theta). \tag{2.3}$$

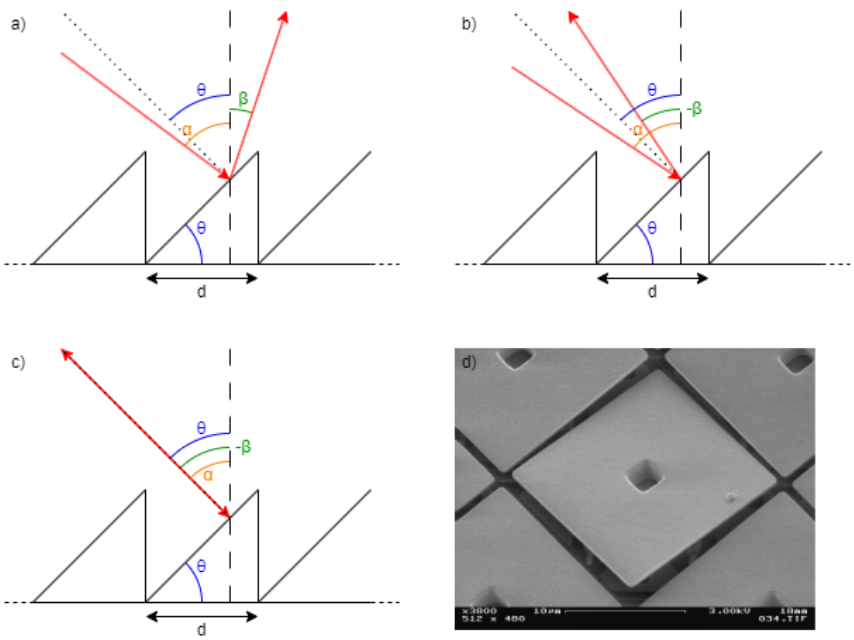


Figure 2.12: Ray diagram for a reflective diffraction grating in three configurations: a) Non-blazed diffraction, b) Blazed diffraction, c) Littrow configuration. The dashed line represents the normal to the grating while the dotted line represents the normal to the surface of an individual micromirror. d) an SEM image of a DMD pixel flipped to the 'on' state (in this case 10°, while the actual DMD we used had a 'pitch' of 12°)[87].

There is a special case, known as Littrow configuration, in which $\alpha = -\beta = \theta$, where the input and output beams follow the same path. Unfortunately, as θ and d are both fixed by the geometry of the DMD, this gives a strict constraint on the wavelength,

$$\lambda(m) = \frac{2d\sin\theta}{m}. \tag{2.4}$$

Where the only other free parameter is m, which must be an integer. We find that for our parameters of $\theta = 12°$ and $d = 10.8\,\mu\text{m}$, the closest wavelengths allowed by this condition to the D1 and D2 lines are $\lambda = 748.5\,\text{nm}$ for $m = 6$ and $\lambda = 898.2\,\text{nm}$ for $m = 5$. Neither of these are suitable, so we choose not to use Littrow configuration, and instead use a blazed configuration with $m = 4$ in most cases. We choose a low value of m, as the efficiency of diffraction drops as m increases, but take one high enough to allow for simple geometry of the optics.

The blazed diffraction order then forms an image which is passed through a 3× telescope, before being combined with the imaging beam path on a dichroic mirror for 674 nm light, or

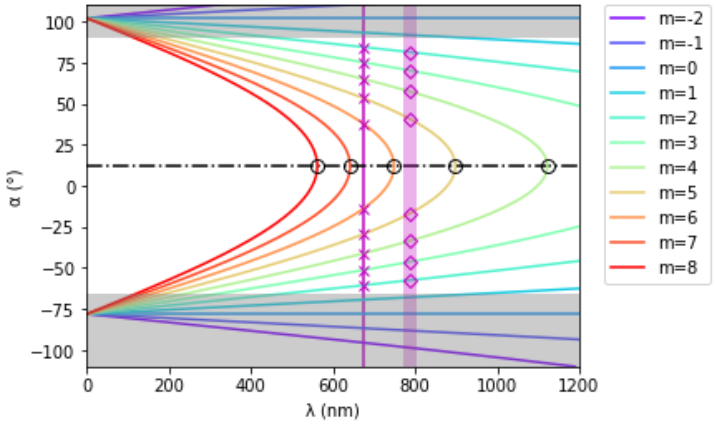


Figure 2.13: Curves showing the angles of incidence, α, which correspond to the blazing condition for different wavelengths and different diffraction orders (orders $m = -2$ to $m = 8$ shown) on our DMD with $d = 10.8\,\mu\text{m}$ and $\theta = 12°$. The magenta shaded area shows the region of wavelengths used with the tuneable laser, with blazed angles shown as diamonds. The solid magenta line shows the wavelength of the red laser, and its blazed angles are shown as magenta crosses. The black dash-dotted line shows the Littrow configuration condition i.e. $\alpha = \theta$, and the black circles show the wavelengths for which this is also blazed. Clearly there are no blazing Littrow configurations corresponding to useful wavelengths, and therefore we choose a non-Littrow blazed configuration. The grey shaded areas correspond to angles which are ruled out because they would require either the input or output beam to be at more than 90° from the DMD's normal.

90/10 beam cube for IR light. It then passes through a tube lens before being focussed by a microscope objective onto the atoms. The microscope objective typically used to focus the light onto the atoms is the G Plan Apo 50X Objective from Mitutoyo, which has a focal length of 4mm and a numerical aperture of 0.50. Due to the small depth of focus for a microscope objective, it is important to make sure that the distance between the objective and the cloud is correct. In order to do this, we first focus the top imaging objective well onto the atoms, then project an image from the DMD onto the CCD through the lower objective. The lower objective position is then adjusted until the image is focussed onto the CCD. This ensures that the image plane of the DMD projection system is the same plane as the object plane of the imaging system, which is in turn the plane of the atomic cloud. In practice, this often requires multiple iterations of this procedure due to uncertainty in the quality of focus in the top imaging objective.

2.6.2 Tuneable Laser

The first light source which was used was a tuneable diode laser (Toptica DL pro). This had peak intensity of 147 mW at 797.4 nm, and could be tuned between 763.32 nm and 812.76 nm, with power dropping to less than half of its peak value at the extremes of the wavelength range. The laser could therefore be tuned for different purposes. It could be either blue detuned or red detuned from the D1 and D2 lines depending on whether repulsive or attractive potentials were required. The size of the detuning could also be modified depending on whether we were limited by the heating rate or by the maximum potential.

2.6.3 Superluminescent Diode

This section is a reformatted, slightly adapted copy of my paper: A. Smith, T. Easton, V. Guarrera, and G. Barontini. "Generation of optical potentials for ultracold atoms using a superluminescent diode", which was published in Physical Review Research. Some of this material remains largely unchanged, others has been made more appropriate for the thesis.

Our SLD light source is a Thorlabs SLD830s-A20, emitting 23 mW over a spectrum with full-width at half maximum of $\Delta\lambda = 20.3\,\text{nm}$, centred at $\lambda_c = 836\,\text{nm}$, as shown in Fig. 1b. From the spectrum we estimate the coherence length of the SLD to be $l = 2\ln 2\lambda_c^2/n\pi\Delta\lambda \simeq 15$ μm. The light produced by the SLD is then amplified to 300 mW using a tapered amplifier (TA) with gain centred at 840 nm (Eagleyard EYP-TPA-0830). The spectrum of the amplified light is a convolution between the gain curve of the TA and the SLD spectrum. This is shown in Fig. 2.14b, where it is possible to appreciate that after the amplification the spectrum is centred at $\lambda_c' = 840\,\text{nm}$ and its full-width at half maximum is $\Delta\lambda' = 9.4\,\text{nm}$, therefore smaller than that of the bare SLD. This results in a doubly longer coherence length of $l' \simeq 33\,\mu\text{m}$. Care must be taken to provide 30 dB of isolation between the TA and the SLD to prevent damage to the latter with the TA back emission. The amplified light passes through an acousto-optic modulator that allows us to control its power and then is injected into a single mode optical fibre. A flip mirror allows us to use the same acousto-optic modulator and fibre with the laser tuned at 800 nm,

enabling a direct comparison between the two light sources. We do not observe any difference in the acousto-optic modulator efficiency between the two light sources. The light coming out from the optical fibre is reflected by a DMD and then sent onto the atoms along the vertical direction, demagnified by a factor 100 using an optical setup that includes a 50× high-resolution optical microscope objective, as described above (see Section 2.2.2). After reflection by the DMD and transmission through the optics, we typically obtain 1 mW of power at the position of the atoms.

SLD vs Laser Comparison

In this section we quantitatively compare the images produced using the SLD and the laser. For simplicity and clarity, we constrain our analysis to one-dimensional structures, as our findings can be easily extended to two dimensions. In particular, we investigate the ability of the two sources to produce square-wave gratings with our optical system, as in the examples in Fig. 2.15a and b. In order to quantitatively compare the images produced by the two sources, we use two parameters: the *fidelity* and the *contrast*. We have chosen to separately evaluate these two parameters to highlight the superior ability of SLDs to produce square-wave patterns, regardless of their amplitude or residual background. To compute the fidelity, we perform two-dimensional fits of the images produced on the CCD I with the "target image",

$$I_0(i,j) = A + B\vartheta[\cos(\pi i d/L + \phi)], \tag{2.5}$$

i.e., a perfect square-wave grating, with $\{i, j\}$ the pixel coordinates in the two directions, d the pixel size and L the semi-period of the square-wave. A, B and ϕ are free fitting parameters. The fidelity is then defined as:

$$F = 1 - \frac{1}{BN}\sqrt{\sum_{i,j}(I(i,j) - I_0(i,j))^2} \tag{2.6}$$

where N is the number of CCD pixels in the region of interest. As an example, in Fig. 2.15c and d we report the residuals $I(i,j) - I_0(i,j)$ obtained by fitting the outlined regions in Fig. 2.15a

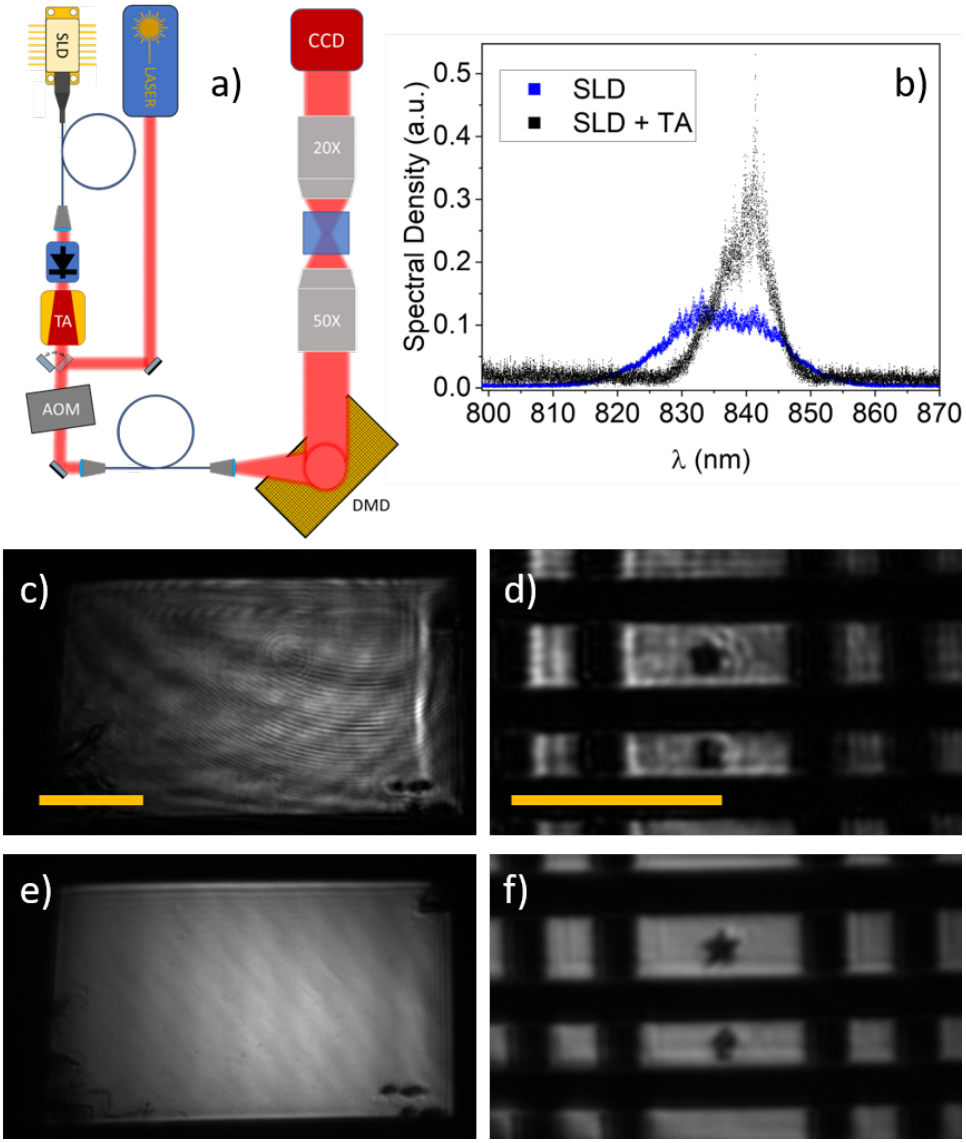


Figure 2.14: a) Schematic representation of our optical system for comparison of the SLD with a laser. The SLD light is first amplified by a TA and then injected into an optical fibre to clean the mode. An AOM is used to control the power injected in the fibre. The output of the fibre is reflected by a DMD that imprints arbitrary patterns on the intensity profile. The patterned intensity profile is then imaged on the atoms using a 100× demagnification system that includes a 50× objective. The plane where the image is produced, that corresponds to the plane where the atoms are trapped, is then imaged on a CCD camera using a 20× magnification system. We can use the same path for the laser source by activating a flip mirror. b) Emission spectrum of the SLD (blue) and spectrum after the SLD emission has been amplified by a TA (black). The spectra are normalised to have the same area.
c) Image produced by the laser at the position of the atoms with the DMD fully *on*. d) Same as c) but with a 2× zoom on a pattern containing an irregular mesh, a star and an arrow. Both the bars in c) and d) correspond to 50 μm. e) and f), same as c) and d) but using the SLD as light source.

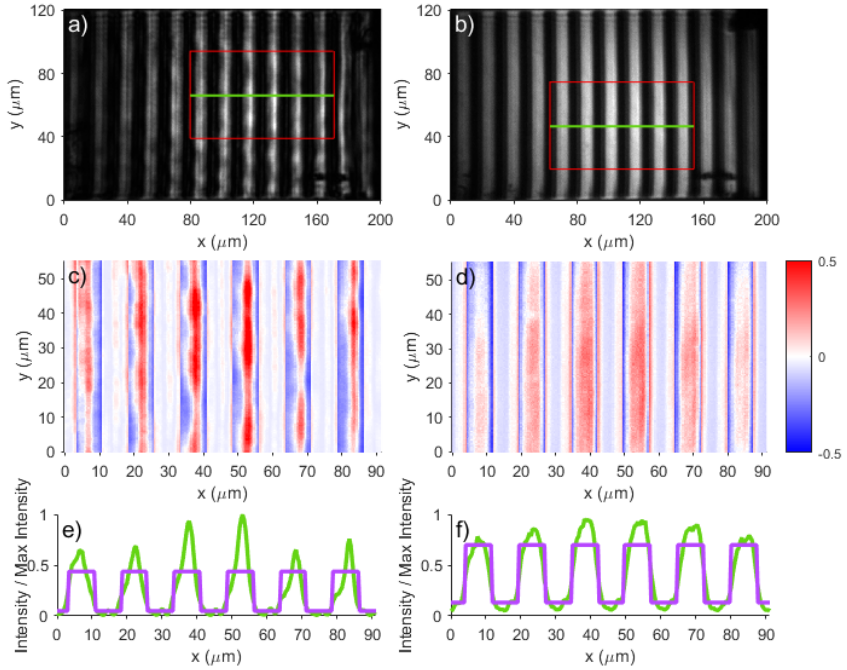


Figure 2.15: a) Image produced on the plane of the atoms using the laser source and a square-wave pattern on the DMD with period 1512 μm, corresponding to a period of 15.12 μm in the imaging plane. b) The same as a) but using the amplified SLD as the source. c) And d) are the residuals obtained by fitting with a square-wave grating the regions within the red rectangles in a) and b) respectively, which correspond to the beams peak intensity regions. The colour bar indicates the values of the residuals. The green curves in e) and f) correspond to 1d cuts along the green lines in a) and b) respectively. The magenta curves are the fits to the data using eq. (2.5).

and b with the same square-wave function. We consistently observe that for SLD-generated images the values of the residuals are lower all across the images, and also that the images have fewer aberrations. This is also evident in Fig. 2.15e and f, where we show the 1d cuts across the green lines in Fig. 2.15a and b together with the fits done using eq. (2.5). To evaluate the contrast, we integrate the images along the y direction obtaining one-dimensional arrays $\tilde{I}$ and then compute

$$C = \frac{\max(\tilde{I}) - \min(\tilde{I})}{\max(\tilde{I})}. \tag{2.7}$$

The fidelity quantitatively estimates how close the image produced is to the target image, while the contrast accounts for the ability of a certain source to effectively produce dark regions, indeed it varies linearly with $\min(\tilde{I})$. For the implementation of accurate optical potentials for cold atoms we require both these quantities to be as close to 1 as possible. Indeed, low values

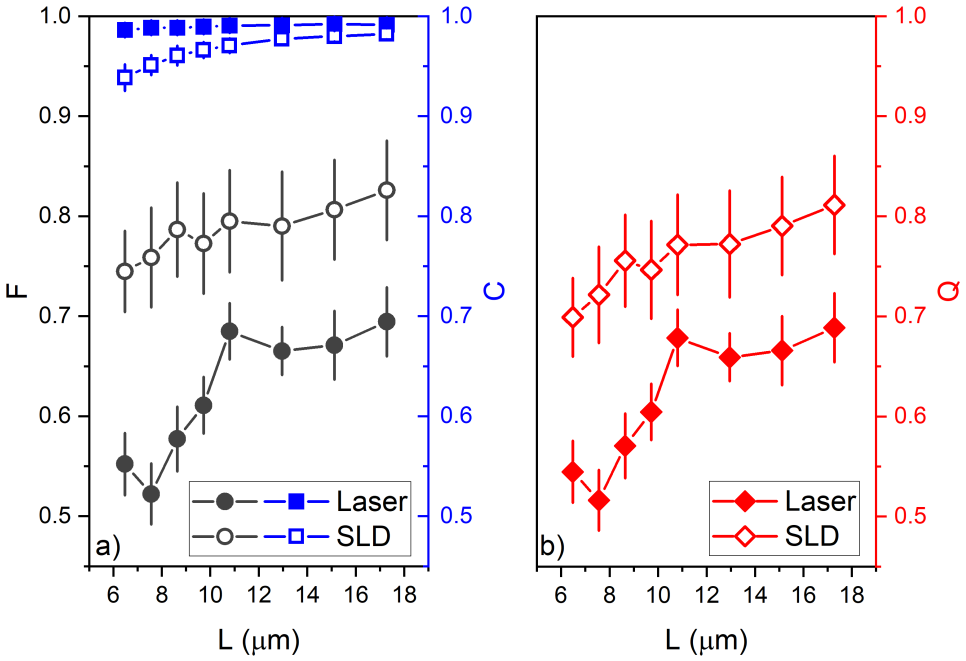


Figure 2.16: a) Fidelity (circles) and contrast (squares) of the SLD images (open symbols) and laser images (filled symbols) as a function of the semi-periodicity of the square wave L. b) Quality of the image as a function of L for the SLD images (open symbols) and the laser images (filled symbols).

of F indicate aberrations in the optical potential and therefore a limited capacity to accurately manipulate the atoms. Low values of C imply instead that higher intensities need to be used to reach the desired potential depth, causing an increase in the scattering rate that makes the potential increasingly less conservative. To account for both these effects we use the *quality of the image* $Q = F \times C$ as our figure of merit. An image with $Q = 1$ would perfectly produce the desired optical potential. In Fig. 2.16 we report the behaviour of F, C and Q as a function of L. With L we indicate the semi-periodicity in the imaging plane, therefore L is a factor 100 smaller than the semi-periodicity of the pattern on the DMD. The SLD images are characterised by a slightly lower contrast than the laser images, especially for low values of L. Our measurements therefore confirm that temporal coherence plays a minor role in the contrast of an image [88], but also suggest that as the size of the features is reduced, such role becomes increasingly important. Notably, SLD images consistently feature a substantially higher fidelity, as the reduced temporal coherence of the SLD almost completely eliminates interference effects. The main source of loss of fidelity for the SLD images is the underlying Gaussian distribution of the intensity, as

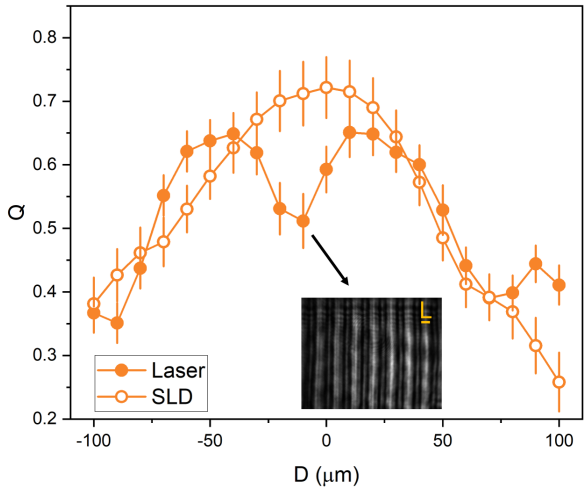


Figure 2.17: Quality of the image generated by the SLD (open symbols) and the laser (filled symbols) for L=7.56 μm a function of the distance from the focal plane D. For SLD-generated images Q is a smooth function of D, while for laser-generated images Q is modulated by the Talbot effect, that every $\simeq$80μm generates images with semi-periodicity $L/2$, as shown in the inset.

can be seen for example in Fig. 2.14e and 2.15b,d. The overall effect is that the SLD generates images with values of Q higher by at least 0.1 than those generated by the laser over the whole range explored. Our imaging system does not allow us to perform quantitative measurements for $L < 5$ μm. To provide a qualitative estimate below the limits of our imaging system, we fit C and F with second order polynomial functions. By doing this we infer that the SLD images should feature a higher Q down to sub-μm structures.

Another important feature stemming from the partial incoherence of SLD-generated light is that it is free from the Talbot effect, that alters the periodicity of regular structures as the beam propagates. This can be observed in Fig. 2.17, where we report the quality of the image Q as a function of the distance from the focal plane D for $L = 7.56$ μm. We observe that for SLD-generated images Q is a smooth function of D, while for laser-generated images Q presents some local maxima and minima. The minima are due to the Talbot effect, that at integer fractions of the Talbot length $\Lambda = 2(2L)^2/\lambda$ causes the appearance of images with $L/2$ semi-periodicity. This in turn causes a degradation both in F and C. SLD-generated images feature also higher values of Q over a broad range of D. The fact that the images produced by the SLD are free from the Talbot effect can be relevant for the implementation of high-quality 3d-patterns, lattices and

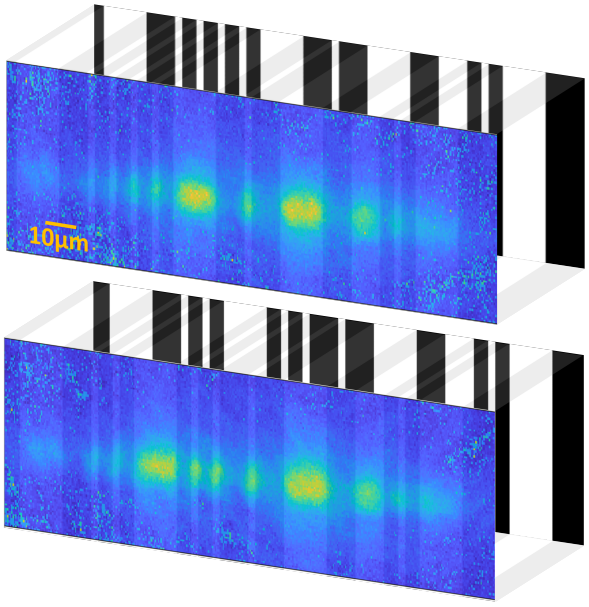


Figure 2.18: In-situ absorption imaging of our ultracold atoms under the action of two distinct 'disordered' potentials. The temperature of the atoms is 20 nK. The patterns imprinted on the DMD are reported in the back panels, and we indicate with black (white) the regions of the DMD where the micromirrors are set to off (on). Regions where the micromirrors are on correspond to regions with full intensity on the atoms, and therefore to attractive potentials. The depth of the potential is 90 nK. The atoms re-arrange in such 'disordered' potentials, nicely retracing the patterns set on the DMD.

holograms using two perpendicular beams that carry periodic or near-periodic structures.

SLD-generated optical potentials for cold atoms

Besides the low temporal coherence that enables the generation of optical potentials with higher quality than lasers, SLDs feature high spatial coherence, that in turn implies Gaussian propagation. On the one hand this represents a problem in reaching very high values of Q, as demonstrated in the previous section. On the other, this is a crucial feature to reach sufficiently high intensities and generate optical potentials that can be used to manipulate ultracold atoms.

Using the SLD, with our setup we can achieve 1 mW of power over an area of $207\times 117\,\mu$m at the position where the atoms are trapped. To evaluate the corresponding optical potential, we fit the amplified spectrum of Fig. 2.14b with a double-Gaussian obtaining the power spectrum

$G(\lambda)$, with λ the wavelength, and then we calculate

$$U(x,y) = -\frac{\pi c^2}{2}\Gamma \int \left(\frac{2}{\Delta_2 \omega_2^3} + \frac{1}{\Delta_1 \omega_1^3}\right) J(x,y,\lambda) d\lambda \tag{2.8}$$

with Γ the linewidth and $\omega_{1,2}$ the frequencies of the D1 and D2 lines of ^{87}Rb, $\Delta_{1,2} = \omega_{1,2} - 2\pi c/\lambda$ the corresponding detunings, and

$$J(x,y,\lambda) = \frac{2P}{\pi w^2} \frac{G(\lambda)}{\int G(\lambda')d\lambda'} e^{-2\frac{x^2+y^2}{w^2}}, \tag{2.9}$$

where P is the total power at the position of the atoms and w is the waist of the beam obtained with a Gaussian fit of the intensity profile of Fig. 2.14e. Similarly, we calculate the heating rate as

$$\Gamma_h(x,y) = \frac{\pi c^2 \Gamma^2}{2\hbar} \int \frac{E_r}{k_B} \left(\frac{2}{\Delta_2^2 \omega_2^3} + \frac{1}{\Delta_1^2 \omega_1^3}\right) J(x,y,\lambda) d\lambda, \tag{2.10}$$

with $E_r = 2\pi^2\hbar^2/m\lambda^2$ the recoil energy, where m is the mass of the atoms, and k_B the Boltzmann constant. With our setup we can obtain a maximum intensity of $2P/(\pi w^2)$ =14.3 W/cm^2, corresponding to a maximum potential depth U/k_B ≃90 nK. This red-detuned potential is therefore sufficiently strong to efficiently manipulate our ultracold sample. The associated maximum heating rate is instead ≃1 nK s^{-1} For comparison, the heating rate for a laser at 840 nm with the same intensity is ≃0.5 nK s^{-1}. Indeed, we could not observe any measurable heating in the typical time scale of our experiments (hundreds of ms) even when illuminating the atomic cloud with the DMD fully on.

To give an example, in Fig. 2.18 we demonstrate that the combination of arbitrary patterns produced with a DMD and the good quality of the images produced by the SLD can be used to arrange ultracold atoms in non-periodic structures. We have implemented two arbitrary 'disordered' 1d potentials by setting unequally spaced gratings on the DMD, as displayed in the back panels. The white vertical lines, corresponding to regions of high intensity, cross with the dipole trap potential creating a series of neatly-separated, sharp squared dimples of different sizes and with different spacing. The dimples are sufficiently deep to trap the atoms, indeed their

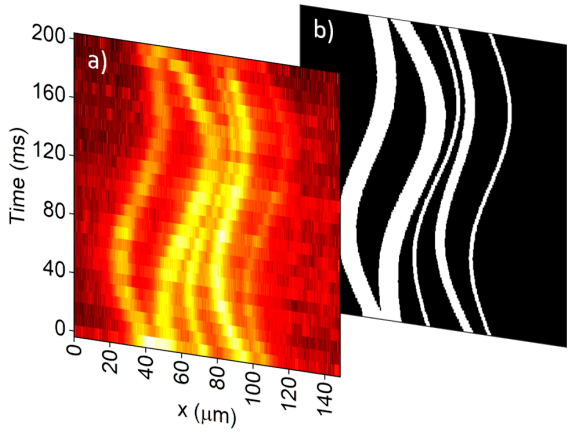


Figure 2.19: a) Evolution of the atomic column density, integrated along the y direction, as a function of time under the action of the dynamical potential (also integrated along the y direction) displayed in panel b). The time frames are taken every 8 ms. The black (white) regions in b) correspond to micromirrors set off (on) on the DMD.

density profile in absorption nicely retraces the patterns imprinted on the DMD, including the sharp edges. Evaluating the fidelity and contrast directly on the the atomic sample can therefore also be used to characterise the potential.

We finally demonstrate the implementation of dynamical potentials with SLDs. The possibility to rapidly reconfigure the pattern on the DMD is particularly appealing as it allows us to dynamically and arbitrarily modify the potential on the atoms a fast as one frame every 100 µs. For dynamical potentials, good image quality is especially desirable as it ensures a good uniformity of the potential across the whole illuminated area, potentially reducing losses of atoms, spurious excitations and heating. In Fig. 2.19a we report the evolution of the density profile of our ultracold atomic sample under the action of the dynamically varying 'disordered' potential of Fig. 2.19b. For every frame we have integrated the density profiles along the y direction. In this case, the pattern on the DMD was modified every 500 µs. We observe that the atomic density is dynamically modified following the trajectory of the optical potential. After 200 ms of evolution, we retain $\simeq$75% of the atoms.

2.6.4 Red Laser

Despite the advantageous coherence properties of SLDs for image formation, they have the disadvantage of reduced power and limited wavelengths available. For these reasons, it was decided that a laser should be used as the primary light source for performing experiments. The majority of the work described in this thesis uses the tuneable infrared laser described above. However, it seems that some measurements were limited by the heating due to the small detuning from this laser. In order to address this, a new red laser was installed. The laser diode is a M1F4S22-675.5-10C-SS5.2M2P19T3 from Coherent. Its central wavelength is 674 nm, with a linewidth of 1.5 nm, and it can produce up to 16 W. The laser is not tuneable, however it is far enough detuned from the transition that the heating rate should be negligible. We can check this by using equations 1.10 and 1.11 to compare the heating rate of a laser at 674 nm to one at, for example, 776 nm, when they are providing the same potential. We find the ratio of heating rates to be 0.037.

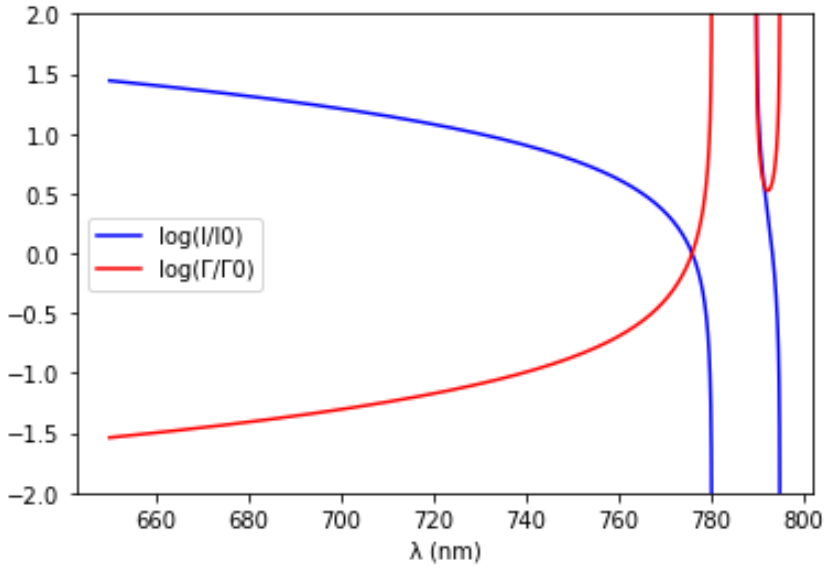


Figure 2.20: Intensity and scattering rate at different wavelengths. The blue curve shows the log of the ratio of the intensity required to generate a given potential at wavelength λ to that at 776 nm. The red curve is the same but for the scattering rate at the intensity that will generate an equal potential.

As the potential and heating rate are both linear in intensity, this value is independent of the potential. However, the far detuning also means that we must use an intensity 22 times

higher to produce the same potential. In order to properly manage the heat output of a diode producing this much power, it was mounted onto a block of copper, which was then mounted on a peltier module, which was then mounted on a large heatsink with a fan. The peltier module's current is modulated my an IGBT which is controlled by a PID temperature controller, attached to an internal thermistor inside the diode module. Even with the increased requirements due to the large detuning, the diode was able to supply more than enough power, and therefore the optics were adjusted to expand the beam to a waist of $\approx 4.8\,\text{cm}$ such that only a small central part of it was incident on the DMD, which has dimensions of $2\,\text{cm} \times 1.1\,\text{cm}$. This means that the beam is more uniform, allowing for more faithful image generation. The use of a laser with a wavelength of 674 nm also has the advantage of having a higher reflection efficiency on our DMD due to the DMD's glass cover being coated for visible light. According to the manufacturer's specifications, the glass cover has a transmittance of $\sim 90\%$ at 800 nm, which causes a round trip loss of almost 20%. 674 nm light is within specification for the glass, and so we have close to 100% transmittance.

Chapter 3

Implementation of Synthetic Dimensions with Atomic Trapped States

This chapter is a reformatted, slightly adapted copy of my paper: C. Oliver, A. Smith, T. Easton, G. Salerno, V. Guarrera, N. Goldman, G. Barontini, and Hannah M. Price "Bloch oscillations along a synthetic dimension of atomic trap states", published in Physical Review Research. Some of this material remains largely unchanged, others has been made more appropriate for the thesis. The experimental work and data analysis was carried out by A. Smith and I, and the numerical data was produced by C. Oliver, with much of the theoretical work carried out by C. Oliver. Because of this, some of the theoretical and analytical details have been omitted from this thesis, but enough has been retained to provide context and explanation for the experimental work and data.

As was briefly explained in the introduction to this thesis, we show the implementation of a synthetic dimension of harmonic oscillator states in a cloud trapped in our crossed optical dipole trap. We implement the coupling between the states by modulating the potential in a spatial and time varying manner using the DMD, at a frequency close to the trapping frequency of the dipole trap. In this chapter I will begin by providing a mathematical overview of the scheme and how it is modelled, including a discussion of how Bloch Oscillations emerge from detuning the modulation frequency from the trap frequency. I will then describe the methods by which

this protocol implemented on the QPrint apparatus. Next I will explain the experimental results and how they were fit and compared to numerical simulations. I will then briefly explain the analytics which were calculated using Floquet Theory to model the motion of the cloud through the synthetic dimension. Finally I will discuss the application of these methods in producing highly excited states.

3.1 Overview of Scheme

To introduce our scheme, let us consider an atomic cloud in a cigar-shaped harmonic trap with trap frequencies $\omega_x = \omega_z \gg \omega_y$. In order to realise the synthetic dimension, we couple together the atomic trap states of the strong trapping potential along x with the spatially- and temporally-varying driving potential given by:

$$V_D(x,t) = -V_0\Theta(x\sin(\omega_D t + \varphi)) \tag{3.1}$$

where V_0 is the driving amplitude, $\Theta(x)$ is the Heaviside step function, ω_D is the driving frequency and φ is the initial driving phase. Physically, this corresponds to illuminating the upper half of the atomic cloud with constant power for the first half of the period, $T_D = 2\pi/\omega_D$, before illuminating the lower half with the same constant power over the second half of the period (see Fig. 3.1(a)). This driving protocol is chosen because it is simple to implement, robust and it leads to a simple Floquet Hamiltonian with near-constant nearest-neighbour hoppings, corresponding to a textbook 1D tight binding model, as discussed below.

Combining Eq. 3.1 with the 1D harmonic oscillator Hamiltonian along x gives the time-dependent Hamiltonian:

$$\hat{H}(t) = \hbar\omega_x \sum_\lambda \lambda \left|\lambda\right\rangle \left\langle\lambda\right| + V_D(x,t), \tag{3.2}$$

written in the eigenstate basis of the "strong" trap along x, as indexed by $\lambda = 0, 1, 2....$

The stroboscopic dynamics of this system is captured by an effective time-independent

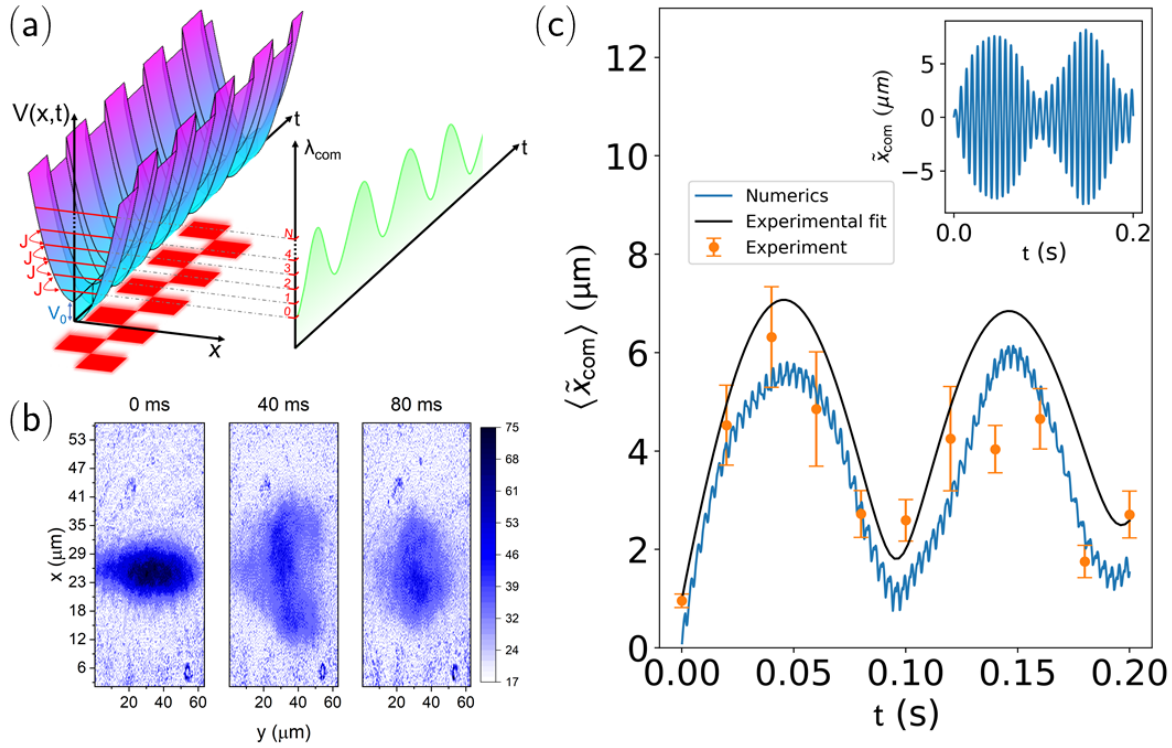


Figure 3.1: Schematic of the experiment and signatures of the synthetic-dimension Bloch oscillations in real space. (a): Schematic of the DMD pattern (*red*), which shakes the harmonic trap (*blue/purple*) and couples together nearest-neighbour trap states with an approximately uniform hopping amplitude, J, in order to create the synthetic dimension. Bloch oscillations (*green*) can be driven along the synthetic dimension by applying a force along λ, corresponding to detuning the shaking frequency from the trap frequency. (b): Experimentally, the cloud is imaged after a short time-of-flight expansion, as demonstrated here for a detuning of $\Delta = 2\pi \times 9.84\,\mathrm{Hz}$. The colour scale is the column density in arbitrary units. The full dynamics includes micromotion within each driving period, so the experimental data are averaged over several values of φ. This averaging procedure makes the cloud appear to widen, although the true cloud width is approximately constant. (c): The real-space centre-of-mass position, x_{com}, of the atomic cloud is extracted, as shown here for the same data as in (b). The experimental data (*orange*) are fitted (*black*) with a function motivated by Bloch oscillations in the synthetic dimension, which captures the real-space dynamics well. Also shown are numerical results (*blue*) with a suitable TOF correction. The micromotion within each driving period can be seen in the inset for an initial driving phase of $\varphi = 0$. To reduce these unwanted micromotion effects, we average both the experiment and numerics over several values of φ (e.g. $\varphi = 0$ and $\pi/2$) to obtain the results shown in the main panel. As can be seen numerically, the residual micromotion oscillations have a small amplitude, which can be further reduced by averaging over more initial driving phases. Panels (b) and (c) use experimental parameters of $V_0 = 4.16\,\mathrm{nK}$, $T = 20\,\mathrm{nK}$, $\omega_y = 2\pi \times 10\,\mathrm{Hz}$, and $\omega_x = 2\pi \times 166.5\,\mathrm{Hz}$, where the latter is determined experimentally by shifting the oscillation frequency data to pass through $(|\Delta|, f) = (0, 0)$. Experimental errorbars are 1σ statistical errors.

Floquet Hamiltonian, which we can approximate over a large number of trap-states by:

$$\hat{\mathcal{H}} \approx \hbar\Delta \sum_{\lambda} \lambda \left|\lambda\right\rangle \left\langle\lambda\right| + J \sum_{\lambda} \left[ie^{i\varphi} \left|\lambda+1\right\rangle \left\langle\lambda\right| + \text{h.c}\right] \tag{3.3}$$

where $\Delta \equiv \omega_x - \omega_D$ is the (small) drive detuning and J is a uniform hopping amplitude, which itself depends on V_0 and ω_x and is calculated using Floquet theory. Note that this description is valid for near-resonant driving in a deep harmonic trap, i.e. such that $\omega_x \simeq \omega_D \gg \Delta, J/\hbar$. As depicted in Fig. 3.1(a), Eq. 3.3 describes a particle hopping between nearest-neighbour sites along a 1D tight-binding lattice with unit spacing in a synthetic dimension. The detuning plays the role of a constant force, $F \equiv -\hbar\Delta$, which therefore can induce Bloch oscillations. Note that the shaking phase φ appears in the effective Hamiltonian as a hopping phase, which we will exploit below to average over unwanted micromotion effects.

In the absence of a force along the synthetic dimension, i.e. when $\Delta = 0$, the effective model in Eq. 3.3 is translationally invariant along the synthetic dimension and has a single energy band in the Brillouin zone. Applying a nonzero force (i.e. $\Delta \neq 0$) accelerates a semiclassical wavepacket formed in the synthetic dimension bulk, such that it undergoes Bloch oscillations across the Brillouin zone, with a centre-of-mass (COM) position along the synthetic dimension, λ_{com}, that varies as [55]:

$$\lambda_{\text{com}}(t) = \lambda^0_{\text{com}} + \frac{2J}{\hbar\Delta}(1 - \cos(2\pi f_B t)), \tag{3.4}$$

from the initial position $\lambda_{\text{com}}(t=0) = \lambda^0_{\text{com}}$ and where f_B is the Bloch oscillation frequency. As we can set the spacing between the fictitious synthetic lattice sites equal to one, the periodic Brillouin zone covers $[-\pi, \pi]$. The Bloch oscillation frequency is then set by the magnitude of the applied force divided by the length of this Brillouin zone, i.e. $f_B = |\Delta|/2\pi$, and so is entirely controlled by the detuning. Conversely, the amplitude of the Bloch oscillations is proportional to the bandwidth divided by the force, i.e. $4J/\hbar\Delta$, and so depends on the detuning but also, through J, on the trap frequency and shaking power. The Bloch oscillations therefore provide a way to transport atoms between different trap states, with independent control over both the

timescale and number of trap states explored.

3.2 Experimental Implementation

Experimentally, we use a thermal cloud of ^{87}Rb atoms in a harmonic trap with trapping frequencies $\omega_x = \omega_z \simeq 2\pi \times 160\,\text{Hz}$ and $\omega_y \simeq 2\pi \times 10\,\text{Hz}$. The cloud was measured, both in-situ and with standard time-of-flight techniques, to have an initial temperature of $T \simeq 20\,\text{nK}$. We used a rapid evaporation ramp to prevent the sample from condensing at this temperature, thus reducing the effect of mean-field interactions [55], which may complicate the dynamics and will be of interest in future investigations. To realise the driving potential of Eq. 3.1, we utilise a digital micromirror device (DMD) that allows us to dynamically and spatially control the intensity profile of a laser beam with wavelength 800 nm. We verify that the trapping and driving potentials are aligned to within $\simeq 1\,\mu\text{m}$. Our driving potential was chosen because it was found to be the most effective and robust, in the sense of not being sensitive to misalignments and other imperfections. This is in addition to the favourable theoretical properties discussed above. We then perform absorption imaging of the atomic cloud in position space after a very short time-of-flight (TOF) expansion of $t_{\text{tof}} = 5\,\text{ms}$, chosen to increase the visibility of the dynamics. This is demonstrated in Fig. 3.1(b) for a detuning of 9.84 Hz, where we plot the real space cloud density as a function of time for an example Bloch oscillation, showing the cloud COM being displaced away from the origin. Note that the density is averaged over several values of φ in order to reduce the effect of micromotion. As such, the cloud appears to widen along x in time, although the cloud width is actually approximately constant. The initial temperature of $T \simeq 20\,\text{nK}$, corresponds to $\lambda^0_{\text{com}} \approx 2$ for an initial Maxwell-Boltzmann distribution of atomic energies. This means that, initially, the atoms start near one “edge" of the synthetic dimension (at $\lambda = 0$), and so atoms must move up the synthetic dimension, irrespective of the sign of the detuning, i.e. the direction of the force. The cloud also does not have a Gaussian distribution with respect to the synthetic dimension as the above semiclassical theory implicitly assumes; nevertheless, as we shall show, the prediction in Eq. 3.4 works well once appropriate corrections

are included.

In our experimental realisation, the final trapping frequencies are $f_x = f_z \simeq 160\,\mathrm{Hz}$, and $f_y \simeq 10\,\mathrm{Hz}$, where z is the vertical axis, resulting in a cloud elongated along y, with $N \simeq 2\times10^4$ atoms at $\simeq$20 nK. We conclude a posteriori that the degeneracy of the x and z trapping directions does not affect the dynamics because of the good agreement between theory and experimental data. We also verified using horizontal imaging that there are no significant dynamics along the z-direction. We verify the alignment between the driving and trapping potentials to a precision of $\simeq$1 µm by imaging both the cloud and the DMD pattern at once. This was done every 20 runs to avoid slow drifts. We also note that we do not observe significant heating of the cloud due to the driving potential. We determine this by observing the width of the cloud in the weak trapping direction after a short TOF expansion and finding that it does not change, as shown by experimental data in Fig. 3.6. This is caused by any "heated" atom spilling out of the weak trap, leading to some atom loss but a fixed temperature.

3.3 Bloch Oscillations

Bloch oscillations in λ-space naturally translate into atomic motion along x in real space, as different harmonic oscillator eigenstates have different real-space profiles. The resulting motion can be seen in Fig. 3.1, where we report the measured dynamics of the real-space COM position under the action of the shaking potential, as a function of time. It is important to notice that the full dynamics also includes micromotion within each driving period [55]; for the real-space COM, as shown numerically in the inset of Fig. 3.1(c), the micromotion corresponds to large and fast oscillations as the atoms slosh backwards and forwards in the trap, while the stroboscopic Bloch oscillations translate into variations in the envelope of the dynamics. We are not able to reliably achieve the high time resolution to observe the micromotion in experiment, so we apply an averaging procedure to remove it. This is because of drifts in experimental parameters on a timescale of hours, which would make the large number of measurements required to reconstruct fast dynamics impractical. To overcome this, we root-mean-square (RMS) average

over different experimental runs with suitably-chosen different initial driving phases, φ. The raw cloud images in Fig. 3.1(b) have themselves been averaged in this way. This has the effect of making the cloud appear to widen significantly over the oscillation, although in each single shot the width is approximately constant. Note that this averaging procedure slightly lowers the apparent amplitude of the motion. However, by reducing the micromotion effects, we can then clearly observe the real-space signatures of the synthetic-dimension Bloch oscillations, as reported in Fig. 3.1(c) for the same parameters as Fig. 3.1(b) (*orange*), where the experimental data is fitted by a function (*black*) motivated by synthetic-dimension Bloch oscillations:

$$x(t) = A\sqrt{1 - e^{-gt}\cos(2\pi f t + \phi)}, \tag{3.5}$$

where we fit to find the amplitude A and frequency f. We introduce the additional fit parameters g and ϕ to capture some details of the experimental data. As can be seen, this fit captures the behaviour of the data very well, with agreement between the experiment and numerical simulations (*blue curve*) of a non-interacting 2D thermal cloud. Our numerical simulations use the time-dependent Hamiltonian to evolve an ensemble of states, each of which is a superposition over the eigenstates of the 2D trap with random phase factors to destroy the phase coherence. Physical observables such as the cloud density are found by averaging over these phases. To account for the fact that we do not measure the true position of the cloud due to the TOF expansion, we include an approximate TOF correction to the cloud centre-of-mass position in our numerical simulations. In particular, we use the simulated COM momentum p_{com} to find the semiclassical cloud velocity, and then shift the simulated cloud COM at each timestep.

To further characterise our experimental results, we plot in Fig. 3.2(a) the values of the oscillation frequency obtained by fitting our data for different detunings. As can be seen, for both experiment and numerics, the frequency increases linearly with detuning, as expected from the analytical Bloch-oscillation frequency (*green line*) given by $f_B = |\Delta|/2\pi$ in both real and synthetic space [c.f. Eq. 3.4]. The trapping frequency is determined by shifting a linear fit to the measured oscillation frequencies to pass through $(|\Delta|, f) = (0, 0)$. This provides

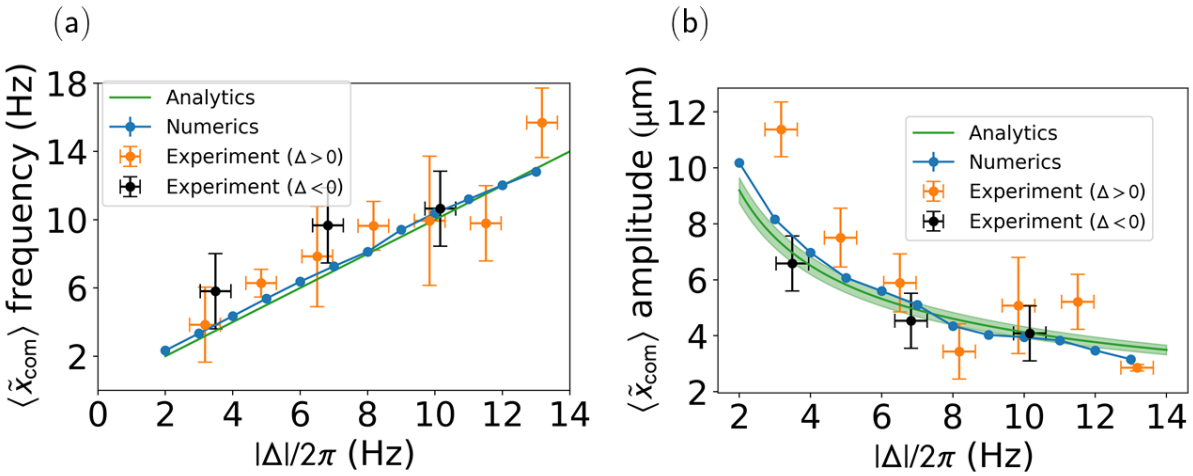


Figure 3.2: Bloch oscillation frequency and real space amplitude as a function of detuning (a): Frequency of the Bloch oscillations for the experiment (*orange* for $\Delta > 0$ and *black* for $\Delta < 0$) and for numerics (*blue*). The observed trend is in agreement with the analytical prediction (*green*) of $f_B = |\Delta|/2\pi$ for Bloch oscillations. (b): Amplitude in real space of Bloch oscillations for the same data as plotted in panel (a). The analytical prediction (*green*) shows the expected real-space amplitude as calculated under appropriate approximations from the synthetic-dimension Bloch oscillations, with the green error band calculated from the errors on J and other numerical parameters. The numerical results are obtained by fitting the same function as in experiment to the TOF-corrected, RMS-averaged results like in Fig. 3.1(c). Note that the numerical fit parameters also include error bars, but these are smaller than the datapoint size. We use the same parameters as Fig. 3.1. Experimental errorbars are 1σ statistical errors.

a straightforward way to measure the trapping frequency, but does mean that any systematic uncertainty would not be detected.

In Fig. 3.2(b) we show how the amplitude of the real-space motion depends on the detuning by plotting the amplitude fitting parameters. As can be seen, the experiment (*orange/black*) and numerics (*blue*) both clearly show the expected growth in the real-space amplitude as the detuning decreases and higher-excited atomic trap states are explored. To make a quantitative comparison with semiclassical Bloch oscillations (Eq. 3.4), we have derived an analytical expression that converts the expected Bloch oscillation amplitude from synthetic space to real space under appropriate assumptions, including a correction for the finite fraction of atoms participating in the dynamics, as discussed further below. The expression is based on the formula:

$$x_{\mathrm{com}} = \sqrt{\lambda_{\mathrm{com}} - \sigma_x^2 + \frac{1}{2}}, \tag{3.6}$$

which connects the real space cloud COM x_{com} and width σ_x to the synthetic space COM λ_{com} under certain assumptions. This analytical prediction is plotted in Fig. 3.2(b) (*green*), with errors calculated from our numerical parameters. As can be seen, there is agreement between the experiment, numerics and the analytics, demonstrating that we have achieved good control of the synthetic-dimension Bloch oscillations.

We can also independently increase the number of atomic trap states explored (i.e. the Bloch oscillation amplitude) while keeping the oscillation frequency constant, by increasing the shaking power, V_0, and hence the hopping parameter J [c.f. Eq. 3.3]. The dependence of the real-space COM amplitude on V_0 is shown in Fig. 3.3(a) for a fixed detuning $\Delta = 2\pi \times 8.3\,\text{Hz}$, while the inset shows the variation of the hopping J, as calculated with Floquet theory.

As can be seen, the amplitude in experiment (*orange*), numerics (*blue*) and analytics (*green*) all increase as the hopping increases [c.f. Eq. 3.4]. Note that the analytical result is only plotted for $V_0 \leq 4\,\text{nK}$, as at higher shaking powers, our simple analytical model (Eq. 3.3) breaks down. Despite this, we still observe clear Bloch oscillation dynamics at high power. This is further demonstrated in Fig. 3.3(b), where we use a very strong potential of $V_0 = 11.96\,\text{nK}$, and still observe the same qualitative trends (i.e. the amplitude decreasing with the detuning and the frequency being equal to the detuning) as in the low power regime. Finally, we can visualise the Bloch oscillations along the synthetic dimension more directly, by translating our real-space experimental measurements [from Fig. 3.1(c)] into λ-space. These experimental results are plotted in Fig. 3.4(a) (*orange*), along with numerical simulations (*blue curve*). Note that the latter is not averaged over different initial driving phases; however, in synthetic space, the micromotion is only a fraction of a "lattice spacing" and becomes negligible as the trapping frequency ω_x increases [55]. We also compare our experimental results directly with the semiclassical analytical predictions [Eq. 3.4] with (*green curve*) and without (*red curve*) multiplying by a constant numerical re-scaling factor to account for the fraction of atoms contributing to the dynamics. This correction was also used in Fig. 3.2 and 3.3 and is necessary because the COM is skewed downwards by the thermal cloud splitting into two distinct parts, with approximately half of the atoms remaining in low λ-states during the oscillation, as can be

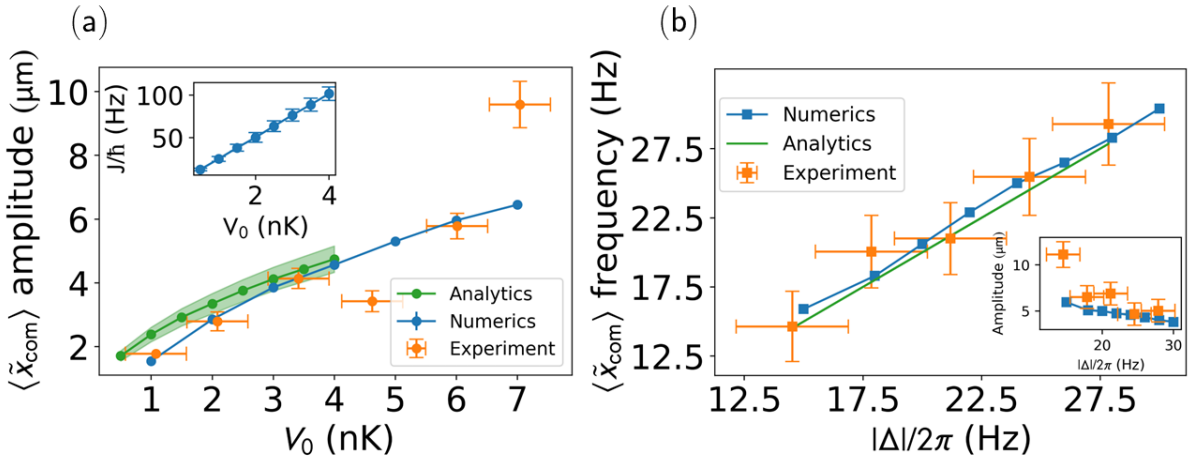


Figure 3.3: Varying the shaking power to control the dynamics. (a): The real-space amplitude [c.f Fig. 3.2(b)] for different shaking powers at a fixed detuning of $\Delta = 2\pi \times 8.3\,\text{Hz}$, with $\omega_x = 2\pi \times 162.6\,\text{Hz}$. As can be seen, the experiment (*orange*), numerics (*blue*) and analytics (*green*) increase with the shaking power; this is because, as shown in the inset, the nearest-neighbour hopping amplitude, J, from Floquet theory, increases with V_0 and hence the Bloch-oscillation amplitude along the synthetic dimension increases. Analytics are only shown up to $V_0 = 4\,\text{nK}$, as at higher shaking potentials the simple nearest-neighbour tight-binding model in Eq. (3.3) is no longer a good description, although the numerics and experiment still appear to exhibit Bloch-oscillation dynamics. This is shown further in (b), where we plot the amplitude fit parameter (inset) and the frequency fit parameter, for $V_0 = 11.96\,\text{nK}$, with $\omega_x = 2\pi \times 142.1\,\text{Hz}$, $\Delta < 0$, and other parameters as in Fig. 3.1 and 3.2. Despite the large shaking power, we still observe similar trends to that at low power [c.f. Fig 3.2], and still with agreement in panel (b) to the $f_B = |\Delta|/2\pi$ analytical result from the simple tight-binding model. Experimental errorbars are 1σ statistical errors. Note that all numerical datapoints include error bars, but these are smaller than the datapoints. The green error band on the analytics is calculated from the errors on J and other numerical parameters.

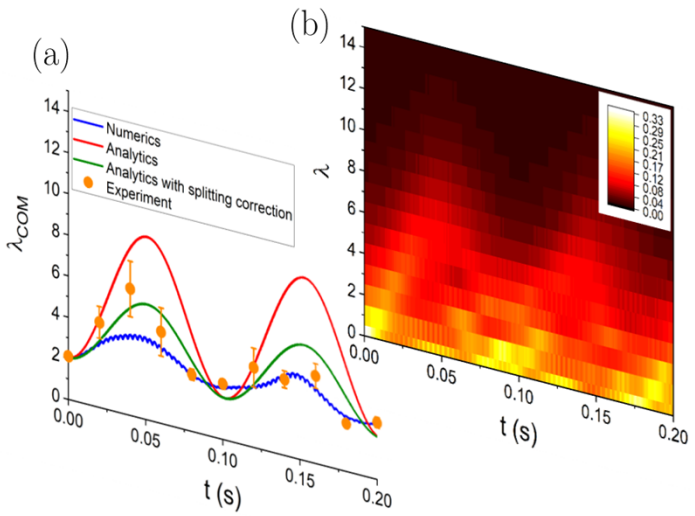


Figure 3.4: Example Bloch oscillation in synthetic space. (a): Evolution of the COM, λ_{com}, and the numerical density distribution heatmap along the synthetic dimension (b) for the same data as Fig. 3.1(b), for $\varphi = 0$. Both Bloch oscillations and high-frequency micromotion are visible in the 2D numerics (*blue line*) for a non-interacting thermal cloud. We also convert the corresponding real space experimental data to synthetic space under suitable assumptions . The observed Bloch oscillation frequency is in good agreement with the 1D analytical semiclassics (Eq. 3.4, *red line*), albeit with a lower amplitude as only around half the atoms from the thermal cloud oscillate along the synthetic dimension [c.f. density distribution heatmap in (b)]. To correct for this, the analytical result is rescaled (*green line*) as discussed in the text. The heatmap shows the numerical atomic density (integrated along the y direction) with respect to λ over the oscillation, showing the cloud-splitting. Both panels use experimental parameters of $\omega_x = 2\pi \times 166.5\,\text{Hz}$, $\Delta = 2\pi \times 9.84\,\text{Hz}$, $V_0 = 4.16\,\text{nK}$, $T = 20\,\text{nK}$, and $\omega_y = 2\pi \times 10\,\text{Hz}$. Experimental errorbars are 1σ statistical errors.

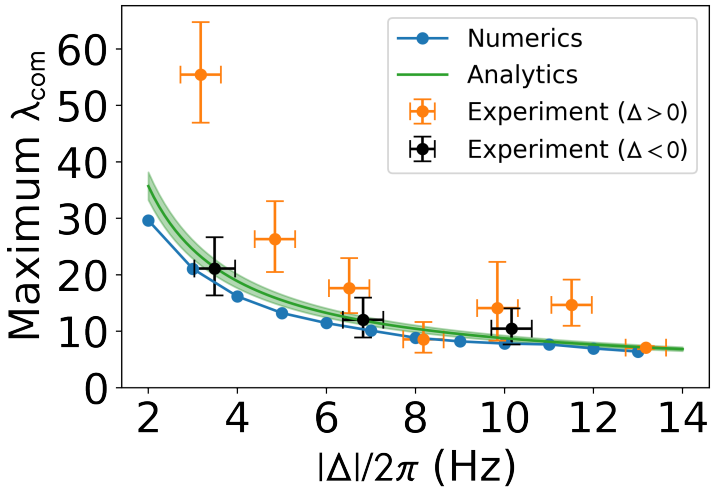


Figure 3.5: Bloch oscillation amplitude in synthetic space. The extrapolated maximum value of λ reached by the oscillating part of the cloud as a function of Δ, demonstrating that we have a long, controllable synthetic dimension. As discussed in Appendix E, we convert the experimental fit parameters in Fig. 3.2(b) to synthetic space (*orange/black*), correcting for cloud splitting. We also plot our numerical maximum λ values (*blue*) for $\varphi = 0$, again corrected for cloud splitting. Furthermore, we derive appropriate analytics (*green*) for comparison. Error bars on experimental points were calculated by converting the real space errors to synthetic space, while the error bars on the analytics were found by propagating errors on J and other numerical parameters. We use experimental parameters of $\omega_x = 2\pi \times 166.5\,\text{Hz}$, $V_0 = 4.16\,\text{nK}$, $T = 20\,\text{nK}$, and $\omega_y = 2\pi \times 10\,\text{Hz}$.

seen in the numerical density distribution heatmap in Fig. 3.4(b). This effect is likely caused by small oscillations in the Floquet Hamiltonian matrix elements..

Importantly, we can also convert our experimental amplitude fit parameters (Fig. 3.2(b)) to synthetic space and divide by the constant numerical cloud splitting factor in order to extrapolate how far up λ the oscillating part of the cloud is actually exploring. This is plotted in Fig. 3.5 (*orange/black*), where we can see that the fraction of the cloud involved in the Bloch oscillations is moving up several tens of Bloch states, demonstrating that we are creating a very long synthetic dimension. This is supported by our numerical (*blue*) and analytical results (*green*).

Note that the number of sites along the synthetic dimension will eventually be limited experimentally by anharmonicities in the trapping potential [55]; however, in this experiment, this does not play an important role. We included the appropriate quartic anharmonic terms in our numerical simulations and found that they had no effect in the range of trap states that are relevant here. Finally, we note that our methods can be extended towards single-site resolution

to on the order of or below $\hbar\omega_x/k_B$. That would start the dynamics with only the $\lambda = 0$ state populated. The subsequent dynamics would maintain the single λ-state character. To reduce micromotion effects, the experimental data for the real-space COM position is RMS-averaged over initial driving phases drawn randomly from $2\pi n/30$, with $n = 0, 1, ...30$. The resulting data are then fitted to the function:

$$x(t) = A\sqrt{1 - e^{-gt}\cos(2\pi f t + \phi)}, \tag{3.7}$$

where A is the amplitude, f is the frequency, g is a damping factor and ϕ is a phase offset which accounts for random variation in the state preparation. The functional form of this fitting function is motivated by translating the semiclassical prediction for synthetic-dimension Bloch oscillations (Eq. 3.4) into real space, using Eq. 3.6. Note that in choosing the form of the fitting function, we assume that the cloud width σ_x is approximately constant as a function of time, as has also been verified numerically. The fitting parameters f and A are then plotted, for example, in Fig. 3.2(a) and (b) respectively. We perform our simulations by time-evolving an appropriate initial state using the time-dependent Hamiltonian in Eq. 3.2, where we also include weak-trap dynamics (i.e. terms that depend on y). We simulate the dynamics of a non-interacting thermal cloud by using an initial state of the form $|\psi_\theta\rangle = A\sum_{i=0}^{N-1}\sqrt{p_i}\exp(i\theta_i)|\phi_i\rangle$, where A is a normalisation factor, $p_i = \exp(-\beta E_i)/Z$ is the Boltzmann weight for the i^{th} eigenstate of the 2D harmonic trap $|\phi_i\rangle$ with energy E_i, β is the inverse temperature, Z is the partition function for the 2D harmonic trap and θ_i is a random phase drawn from a uniform distribution between 0 and 2π. We choose the first N states of the 2D harmonic trap, and we check that the Boltzmann weight is small enough that this is a good approximation. We sequentially generate N' such states, each with a different set of random phases, and then time-evolve each separately. The resulting densities are then averaged together which reproduces the density of a thermal cloud at $t = 0$.

From our numerical simulations, we obtain the cloud density in either synthetic space $\rho(\lambda, y, t)$ or real-space $\rho(x, y, t)$. From these densities, we can then calculate the COM position as a function of time with respect to λ and x respectively. The former is plotted in Fig. 3.4(a),

while the latter requires additional processing steps to be compared with experiment. Firstly, to account for the experimental TOF expansion of the cloud, we apply a correction as $\tilde{x}_{\mathrm{com}} = x_{\mathrm{com}} + v_{\mathrm{com}} t_{\mathrm{tof}}$, where the COM velocity v_{com} is calculated from the numerical momentum distribution. Secondly, we RMS average the M different corrected centres-of-mass together to remove the micromotion: $\langle \tilde{x}_{\mathrm{com}} \rangle = \sqrt{\frac{1}{M} \sum_{i=1}^{M} (\tilde{x}_{\mathrm{com}}^{(i)})^2}$. For the numerics shown in the above, we take $M = 2$ with $\varphi = 0$ and $\varphi = \pi/2$. Finally, we fit our data with the experimental fitting function [Eq. 3.7], although now with $\phi = 0$ as numerically there are no random variations in the state preparation. The corresponding fitting parameters f and A for the numerical data are then plotted, for example, in Fig. 3.2(a) and (b) respectively.

To convert our real space experimental oscillation into synthetic space (Fig. 3.4(a)), we use our conversion formula (Eq. 3.6), assuming that the real space width σ_x (measured in harmonic oscillator lengths) remains constant in time and set by the trap frequency and initial temperature. We then obtain:

$$\lambda_{\mathrm{com}}(t) = \left(\frac{x_{\mathrm{com}}(t)}{\alpha_{\mathrm{rms}} \alpha_{tof}} \right)^2 + \sigma_x^2 - \frac{1}{2}, \tag{3.8}$$

where $x_{\mathrm{com}}(t)$ is the experimental real space COM measured in harmonic oscillator lengths. The conversion for the data in Fig. 3.5 is similar, but here we convert the experimental amplitude fitting parameters, so we use the conversion:

$$\lambda_{\mathrm{com}} = \left(\left(\frac{x_{\mathrm{com}}}{\alpha_{\mathrm{rms}} \alpha_{tof} / \sqrt{2}} \right)^2 + \sigma_x^2 - \frac{1}{2} \right) / r, \tag{3.9}$$

This is then compared against the corresponding numerics, where we extract the maximum value of λ_{com} and rescale by $1/r$ to account for the cloud splitting. We also compare against an analytical expression, $\lambda_{\mathrm{com}} = \lambda_0 + 4J/\hbar\Delta$, as shown in Fig. 3.5.

3.4 Analytical results

The semiclassical prediction for synthetic-dimension Bloch oscillations is given by Eq. 3.4. In order to plot this analytical result, we independently calculate the nearest-neighbour hopping

$J/\hbar = 106 \pm 8\,\mathrm{Hz}$ from Floquet theory. Floquet theory involves removing the micromotion of the system by creating a 'Floquet Hamiltonian', $\hat{H}_F$ such that for some starting time, t_0 we have,

$$\hat{H}_F T = \int_{t_0}^{t_0+T} \hat{H}(t)dt, \tag{3.10}$$

with $\hat{H}$ the full hamiltonian and T the time period of the driving. Using this method, time can be evolved through integer steps of T, and the slow dynamics relative to T, such as Bloch oscillations, become clear.

When calculating this hopping, we observe that the hopping is independent of the detuning, and that each hopping is nearly independent of λ, except for small oscillations. We therefore calculate the error bar by adding the standard deviations of the hopping for each Δ in quadrature. Note that this value applies to our low-power data only; in the high-power case, we have significant long-range hoppings so we can no longer use this nearest-neighbour tight binding model. Note also that, in practice, only a fraction of atoms participates in the dynamics, which leads to a significant reduction in the apparent COM position in both synthetic and real space, as shown in Fig. 3.4. To account for this, we modify Eq. 3.4 to $\lambda_{\mathrm{com}}(t) = \lambda^0_{\mathrm{com}} + r\frac{2J}{\hbar\Delta}(1-\cos(\Delta t))$. Here, $r = 0.52 \pm 0.03$ is the average cloud fraction that undergoes the oscillation, as calculated from our numerics for the low power data, where the error bar is the standard deviation of the different r values for different detunings.

To translate the analytical result from synthetic space to real space, we make use of the conversion formula Eq. 3.6 under the assumption that the real-space cloud width stays constant as a function of time. This leads to the expression:

$$x_{\max} = \frac{1}{\sqrt{2}}\alpha_{\mathrm{rms}}\alpha_{\mathrm{tof}}\sqrt{\frac{\hbar}{m\omega_x}}\sqrt{\lambda^0_{\mathrm{com}} + r\frac{4J}{\hbar\Delta} - \sigma_x^2 + \frac{1}{2}}. \tag{3.11}$$

where we have included corrections for the reduction in amplitude due to RMS averaging, $\alpha_{\mathrm{rms}} = 1/\sqrt{2}$, and for the TOF expansion, $\alpha_{\mathrm{tof}} = 5.25 \pm 0.08$, as calculated from our low-power numerics with an error bar corresponding to the standard deviation across multiple detunings. Note that the cloud width σ_x is here measured in harmonic oscillator lengths $\sqrt{\hbar/m\omega_x}$. This

result is then plotted, for example, in Fig. 3.2(b).

3.5 Creation of highly-excited states

Bloch oscillations along the synthetic dimension offer a way to controllably populate highly-excited atomic trap states. Indeed, by stopping the shaking at a certain given time it is possible to 'freeze' the dynamics. If this is done when the Bloch oscillation is exploring high λ states, the resulting state will have a considerable admixture of highly-excited harmonic trap states. In Fig. 3.6 we show an example of states obtained after a 5 ms TOF expansion with such a technique with $\Delta/2\pi \simeq 17\,\mathrm{Hz}$, $V_0 \simeq 1.2\,\mathrm{nK}$ and stopping the Bloch evolution when the oscillation has reached the peak (40 ms) and half way (20 ms). By averaging over several different phases of the shaking potential, we can reconstruct the whole set of states that can be obtained for a given Bloch evolution time, this is shown as shaded areas in Fig. 3.6 (a) and the column density profiles in Fig. 3.6 (b) and (c). We observe that the resulting density profiles acquire the characteristic double-lobe structure typical of highly-excited harmonic trap states. Additionally, as the Bloch dynamics evolve, we observe that the distance between the two lobes increases, as expected when populating increasingly higher states. Notably, by controlling the phase of the shaking potential, it is possible to accurately control the shape and position of the final state. This is shown in Fig. 3.6 (a), where the two solid lines correspond to averages over several runs with the same phase both for the 20 and 40 ms cases.

We have additionally measured the lifetime of the states created by measuring the number of atoms as a function of time after the Bloch evolution is stopped. We then performed an exponential decay fit, whose decay time sets the lifetime of the state. Concerning the states shown in Fig. 3.6 in particular, we have measured that the lifetime for the states produced after 20 ms of shaking potential is $\simeq$1 s, while for those produced after 40 ms is $\simeq$ 600 ms. Therefore the lifetime of these highly-excited states is sufficiently long to allow one to practically use them. As an example, they would provide a good overlap with a double-well potential enabling new possibilities for trapped atom interferometry [62].

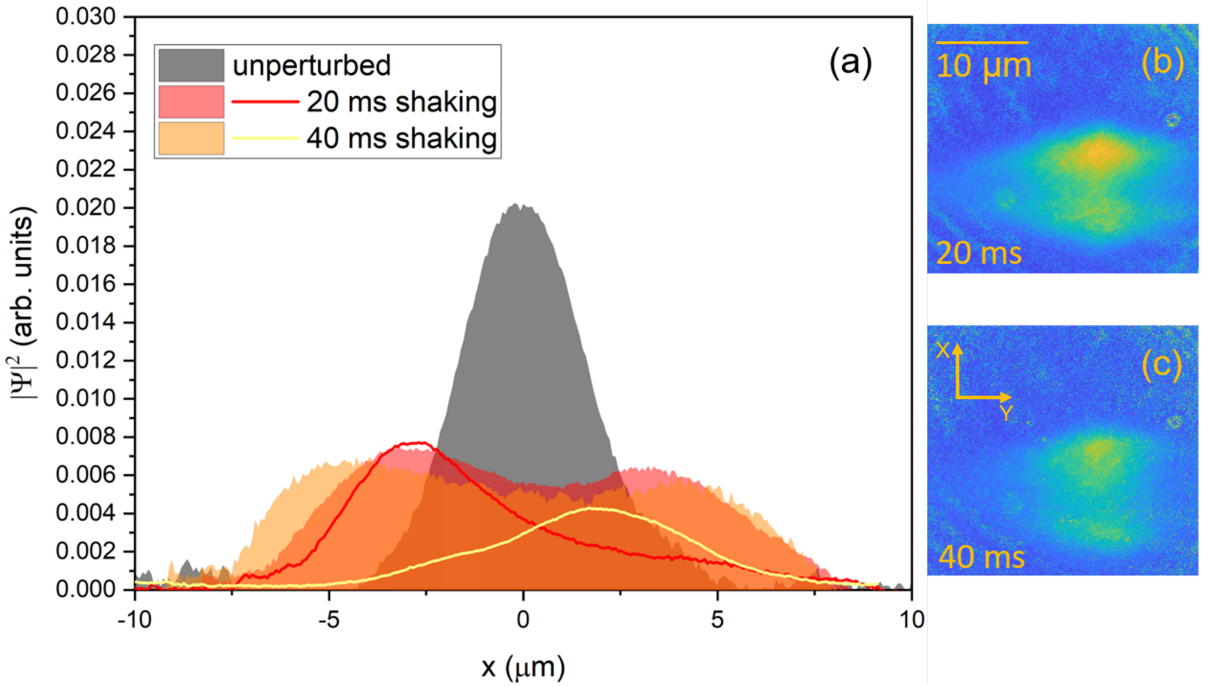


Figure 3.6: (a) Column density distribution integrated along the y direction of our atomic samples after 5 ms of time of flight. The shaded areas correspond to the average of 30 experimental runs where we vary the shaking phase. The solid lines are examples of density distributions that are obtained with fixed phase. The number of atoms is $\simeq 15 \times 10^4$. (b) and (c) are the column densities averaged over 30 runs with different phases in the shaking potential that we observe after 5 ms of time of flight and with 20 and 40 ms of shaking time respectively.

The fidelity of the excited states could be further improved by decreasing the proportion of the cloud that remains in the low-lying λ states, and by decreasing the width with respect to λ of the portion that does oscillate. One approach to achieving this is by a combination of using a stronger trap (i.e. increasing ω_x) and/or a lower temperature, both of which reduce the width of the initial Maxwell-Boltzmann distribution. Fig. 3.7(a) and (b) show the synthetic space density profile, with y-dependence integrated out, for a numerical simulation of a thermal cloud with (a) the typical parameters used elsewhere in our work, and (b) a larger trapping frequency and lower temperature, over a single Bloch oscillation period. As can be seen, in panel (b) the part of the cloud that oscillates is narrower with respect to λ than with our more typical parameters in panel (a). Note that, for a small enough temperature, a significant initial condensate fraction may also affect the dynamics. However, we have verified numerically that an initial state with the whole cloud in the $\lambda = 0$ state (i.e. a non-interacting BEC) still undergoes Bloch oscillations under the driving potential.

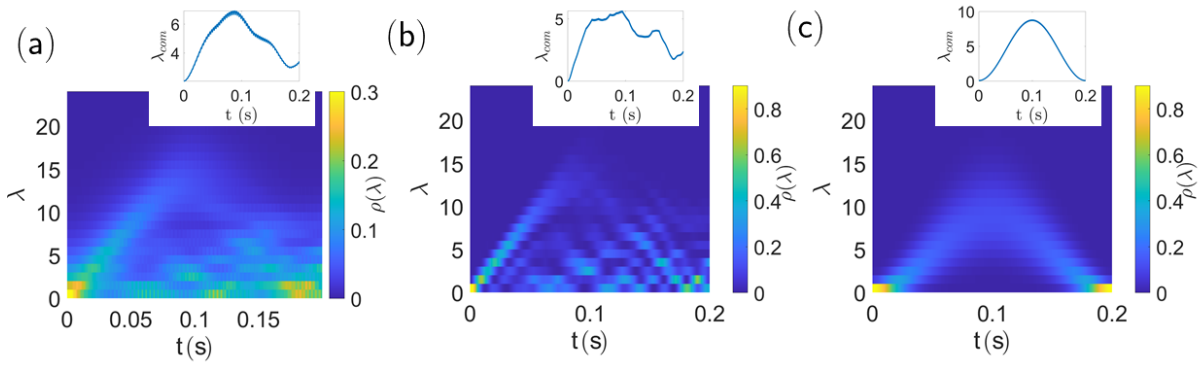


Figure 3.7: (a): Time evolution of the integrated synthetic space density for a thermal cloud under our usual driving potential using typical parameters, for a detuning of $\Delta = 2\pi \times 5\,\mathrm{Hz}$. We see significant cloud splitting and a relatively wide oscillating component. We use identical parameters to our low-power data elsewhere in this work, with $\varphi = 0$. (b): The result in (a) but with increased trapping frequency and decreased temperature, showing that the oscillating part of the cloud becomes much narrower in synthetic space. Note the different colour scale to (a). We use the same parameters as (a) but with $T = 5\,\mathrm{nK}$ and $\omega_x = 2\pi \times 500\,\mathrm{Hz}$. (c): Time evolution of the integrated synthetic space density of a thermal cloud for a modified driving potential, showing that the entire cloud moves, with no split component. Note that the linear driving potential together with parameters as in (a) produces a wide oscillating cloud, so we also increase the trapping frequency and decrease the temperature here to compensate for this. We use: $\kappa x_{\mathrm{qho}} = 1\,\mathrm{nK}$, with $x_{\mathrm{qho}} = \sqrt{\hbar/m\omega_x}$, $\omega_x = 2\pi \times 500\,\mathrm{Hz}$, $\Delta = 2\pi \times 5\,\mathrm{Hz}$, $T = 10\,\mathrm{nK}$ and $\omega_y = 2\pi \times 10\,\mathrm{Hz}$. The insets of each panel shows the corresponding λ COM as a function of time. Note that the results for (a) and (b) are not rescaled to take into account cloud splitting.

We also note that the width of the oscillating part of the cloud also depends upon the detuning. In Fig. 3.8, for the low-power parameters used above, and a detuning of $\Delta/2\pi = 2\,\mathrm{Hz}$ (panel (a)) and $\Delta/2\pi = 5\,\mathrm{Hz}$ (panel (b)), the density with respect to λ is shown close to the peak of the oscillation. The oscillating part of the cloud can be seen to have a full-width at half-maximum (FWHM) of around 8 states in (a). This width depends upon the detuning, with larger detunings yielding smaller widths. For example, in panel (b), the FWHM is around 5 states. Note that these methods to reduce the width of the cloud with respect to λ could be extended towards single-site resolution.

Another strategy for improving the fidelity is to optimize the driving potential. As an example, Fig. 3.7(c) shows the effect of a different driving potential, $V(x,t) = \kappa x \cos(\omega_D t)$, upon a lower-temperature thermal cloud ($T = 10\,\mathrm{nK}$). Note that this driving potential is the same as that of [55] (see Eq. 2 therein). As can be seen, the entire cloud undergoes the Bloch oscillation, with no split component. This difference is likely because for the experimental driving potential (Eq. 3.1), there are oscillations in the Floquet Hamiltonian matrix elements (e.g. Fig. 3.9) at low λ, which include, for example, an effective potential minimum at $\lambda = 0$ which may trap some atoms, leading to the cloud splitting. For the linear driving potential, on the other hand, the Floquet Hamiltonian does not exhibit such oscillations, although there is then a strong λ-dependence in the hopping elements [55]. Going further, quantum control approaches could be used to further numerically optimize the driving potential, in order to improve the fidelity of desired state preparation. Finally, another possible strategy for improving the fidelity of excited states would be to employ a two-step protocol. Firstly, the cloud could be placed into an excited trap state without using the driving potential [58]. Secondly, the driving potential could be activated, causing Bloch oscillations in the synthetic dimension bulk.

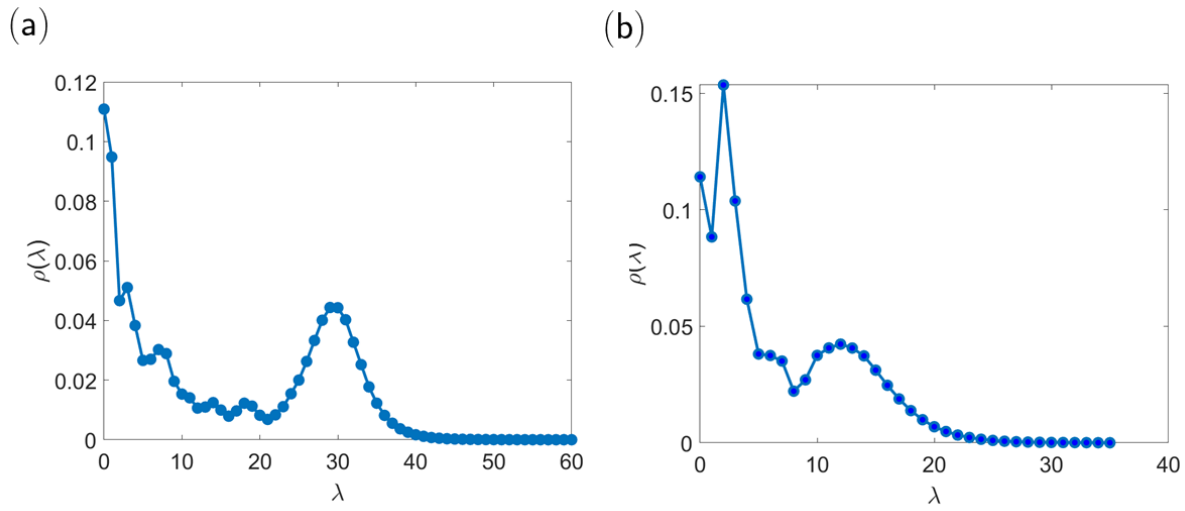


Figure 3.8: Cloud density with respect to λ for the low power parameters used in the above and a detuning of $\Delta/2\pi = 2\,\text{Hz}$ (panel (a)) and $\Delta/2\pi = 5\,\text{Hz}$ (panel (b)). The density is extracted from close to the peak of the oscillation. We clearly see the oscillating part of the cloud, which has a full-width at half-maximum of around 8 states in (a) and around 5 states in (b).

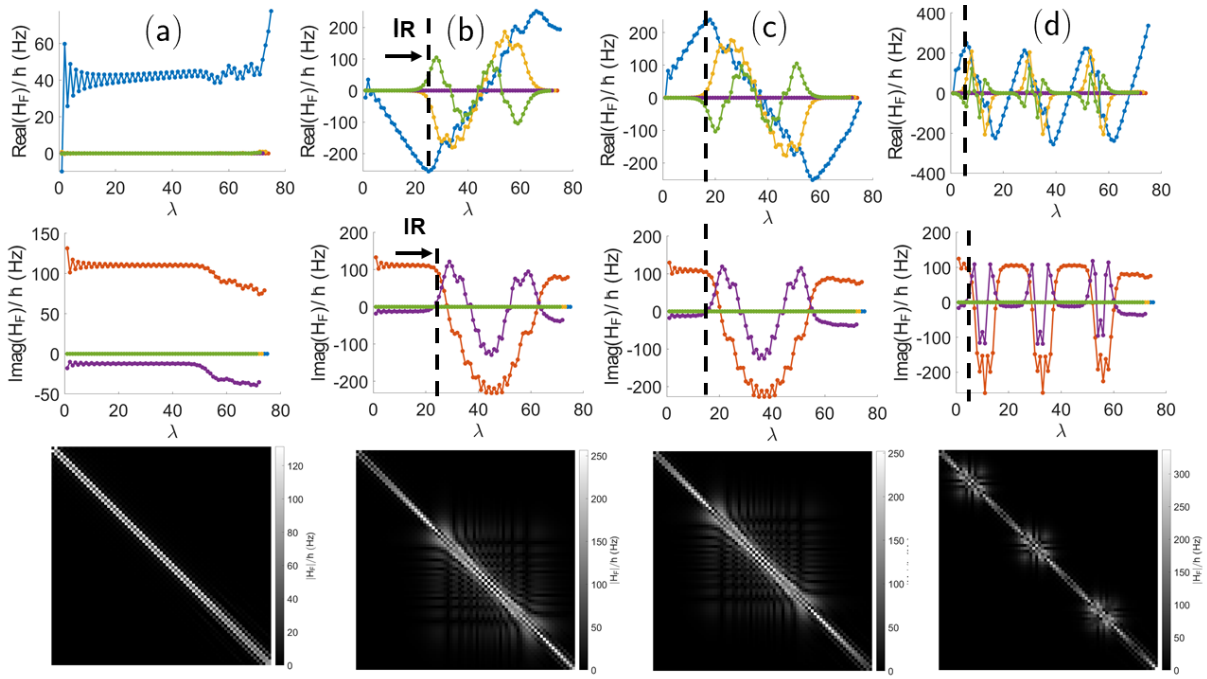


Figure 3.9: Numerically-calculated matrix elements of the full Floquet Hamiltonian for $\omega_x = 2\pi \times 166.5\,\text{Hz}$, $V_0 = 4.16\,\text{nK}$ and $\varphi = 0$, for $\Delta = 2\pi \times 0, -2, 2$ and $7\,\text{Hz}$ in columns (a), (b), (c) and (d) respectively. These parameters correspond to the low-power data shown in Fig. 3.1, 3.3, 3.4 and 3.5 . The top row shows the real part of the first five diagonals, the middle row shows the imaginary part, and the final row shows a heat map of $|\hat{H}_F|$. The on-site terms are in blue, the NN hoppings in red and longer-range hoppings in other colours. We see that we can approximate $\hat{H}_F$ by a nearest-neighbour tight-binding model where Δ plays the role of a force along the synthetic dimension. The onset of instability regions (IR), marked by the black dotted lines, show long-range hoppings for some λ and are a numerical artifact and are not physical.

Chapter 4

Simulations of Clustering Dynamics in Quantised Vortex Systems

This chapter is a reformatted, slightly adapted copy of my paper: T. Easton, M. Kokmotos and G. Barontini "Vortex clustering in trapped Bose-Einstein condensates". This has been published in a revised form in Scientific Reports. Some of this material remains largely unchanged, others has been made more appropriate for the thesis.

As mentioned in the introduction to this thesis, trapped atomic Bose-Einstein condensates are an ideal context in which to study the dynamics of quantised vortices due to the ease of generation and interrogation of vortex states. Trapped BECs also have the advantage that their dimensionality can be varied easily by adjusting the ratio of trapping frequencies. In the following work, we consider quasi-2D systems in which we simulate structures vortex states and study their dynamics. Such structures states are now possible to implement using spatially and temporally varying potentials via the phase imprinting method described in the thesis introduction, and could be implemented using an SLM such as a DMD. The work presented here is simulation based, and much of it was completed during COVID-19 lockdowns, however it was all done with a view towards experimental implementation on the QPrint apparatus.

In this chapter, I will provide a brief overview of the concept of quantised vorticity in a superfluid. I will then describe the methods used to simulate the systems of vortices. Next I

will describe the arrangements of vortices we chose and how they form cluster states. I will then describe the algorithm used to quantitatively determine when a state was clustered. Lastly I will describe the analytical model for vortex motion, and an extension of this model to one which models the motion of clusters.

4.1 Quantised Vorticity

Vortices in Bose-Einstein condensates are quantised topological defects, each of with quantised angular momentum. To see that vortices must be quantised, consider a general form for the velocity field of a vortex at the origin in a 2D plane,

$$\vec{v}(\vec{r}) = v(|\vec{r}|)\hat{\theta}. \tag{4.1}$$

As noted above, the velocity of the condensate can be given in terms of the order parameter's phase by, $\vec{v} = \frac{\hbar}{m}\nabla\phi$.

We then have that,

$$\begin{aligned} \frac{\partial\phi}{\partial\theta} &= \frac{m|\vec{r}|v(|\vec{r}|)}{\hbar} \\ \frac{\partial\phi}{\partial r} &= 0. \end{aligned} \tag{4.2}$$

The solution to this is clearly,

$$\begin{aligned} \phi(\theta) &= n\theta + \phi_0 \\ v(|\vec{r}|) &= \frac{\hbar n}{m|\vec{r}|} \end{aligned} \tag{4.3}$$

Where n is constrained to be an integer because of the condition that ϕ is single valued, up to integer multiples of 2π. The value n is known as the 'topological charge' of the vortex. This configuration also clearly has an angular momentum of,

$$L_z = \hbar n. \tag{4.4}$$

Quantised vortices are also characterised by the density depletion at their cores. In fact, the density must drop to zero at the centre of a vortex, both because the velocity diverges there, and because Stokes' theorem requires that the circulation,

$$\Gamma = \oint_C \vec{v} \cdot d\vec{r}, \tag{4.5}$$

is zero for a simply connected region bounded by a closed path, C. Here $d\vec{r}$ is an infinitesimal displacement along C. The shortest distance over which the density of a BEC can drop from background level to zero is known as the healing length, ξ which is given by,

$$\xi = \frac{1}{\sqrt{8\pi\rho_0 a}}, \tag{4.6}$$

where ρ_0 is the background density and a is the s-wave scattering length. This sets the length scale for the size of the density depletion region around the centre of the vortex. This density depletion can be used in simulations to track the position of vortices, and is visible in experiments after the cloud has been expanded in time-of-flight. Vortices in Bose-Einstein condensates are quantised topological defects, each of with quantised angular momentum. In fact, unless the BEC has a topology which already includes holes, quantised vortices are the only way in which a BEC can support angular momentum.

4.2 Simulation Methods

In order to simulate vortex dynamics, FORTRAN code was run on University of Birmingham's Bluebear cluster to find a ground state solution for the trapping potential, apply a phase change according to the vortex configuration of interest, and then evolve the cloud forwards through time. For these simulations, we assumed that the dynamics followed the Gross-Pitaevskii equation. This ignores small effects beyond the mean field as well as any effects due to finite temperatures, however these effects are known to be very small for a cold enough cloud and a high enough atom number. We simulate a system with $N = 5 \times 10^4$ ^{87}Rb atoms trapped in a harmonic

potential with trapping frequencies $\omega_x = \omega_y = \omega_\perp$ and $\omega_z = \lambda\omega_\perp$ in the radial and transverse directions respectively, with $\lambda = 15$ and $\omega_\perp = 2\pi \times 20$ Hz. We implement these simulations on a grid of $256 \times 256 \times 16$ sites.

4.2.1 Ground State

The first step in simulating the dynamics of a BEC is to find the ground state of the system. This was done using a modified version of the method of 'steepest decent in imaginary time'. This process begins by taking a starting guess for the ground state of the system. In our case, a parabolic Thomas-Fermi density distribution worked well. This is clearly close to the shape of the ground state solution, but the Thomas-Fermi distribution is an approximation which can be numerically improved upon.

The standard process starts with the Schrödinger equation (or Gross-Pitaevskii equation),

$$i\hbar \frac{d\,|\Psi(t)\rangle}{dt} = \hat{H}\,|\Psi(t)\rangle\,. \tag{4.7}$$

If time is evolved forwards, we see that energy eigenstates maintain their amplitudes, and rotate in phase with a frequency proportional to their corresponding energy eigenvalue. However, if one instead evolves towards the negative imaginary axis, energy eigenstates instead decay exponentially, with a rate proportional to their corresponding energy eigenvalue. In this way, the highest energy states are suppressed, and once the state is normalised, the low energy states are enhanced. This process then converges on the ground state. To first order in time step this gives us,

$$|\Psi(t + \Delta t)\rangle \approx (1 - \frac{\Delta t}{\hbar}\hat{H})\,|\Psi(t)\rangle\,. \tag{4.8}$$

Making this process explicitly discrete, we can take $|\Psi_n\rangle$ as the state after n iterations. We can also take $\delta = \Delta t/\hbar$ for simplicity. Finally, we can improve the standard algorithm by adding a term proportional to the mean energy, $\mu_0 = \langle\Psi_0|\,\hat{H}\,|\Psi_0\rangle$, in the following way,

$$|\tilde{\Psi}_1\rangle = (1 - \delta(\hat{H} - \mu_0))\,|\Psi_0\rangle\,, \tag{4.9}$$

This further suppresses energy states higher than the current mean, while enhancing those below it, which has the effect of allowing the result to converge on the ground state more quickly.

We can see that the process reduces the average energy by calculating,

$$\frac{\mu_1}{\mu_0} = 1 - \frac{\delta}{\mu_0}\frac{2\mu_0^{(2)} - \delta\mu_0^{(3)}}{1 + \delta^2\mu_0^{(2)}}, \tag{4.10}$$

where $\mu_0^{(n)}$ is the n-th central moment of the energy distribution for state $|\Psi_0\rangle$. From this we can see that the energy of the system decreases for,

$$0 < \delta < \frac{2\mu_0^{(2)}}{\mu_0^{(3)}}. \tag{4.11}$$

It is therefore possible to reach a good approximation for the ground state by iterating this process, as long as δ is always kept small enough.

4.2.2 Time Evolution

In order to evolve the condensate through time we make the following approximation for the time evolution operator,

$$e^{\frac{-i\Delta t\hat{H}}{\hbar}} = e^{\frac{-i\Delta t(\hat{T}+U_{tot})}{\hbar}} \approx e^{\frac{-i\Delta t U_{tot}}{2\hbar}} e^{\frac{-i\Delta t\hat{T}}{\hbar}} e^{\frac{-i\Delta t U_{tot}}{2\hbar}}, \tag{4.12}$$

where $\hat{H} = \hat{T} + U_{tot}$ is the Gross-Pitaevskii hamiltonian, $\hat{T}$ is the kinetic energy operator and U_{tot} is the total potential energy including the nonlinear term. According to the Baker-Campbell-Hausdorff formula for the product of exponentials of non-commuting objects, the error due to this approximation is on the order of Δt^3. This form is useful because it allows $\hat{T}$ and U_{tot} to be treated separately, and because it is much easier to calculate the result of the kinetic energy operator in momentum space, which can be conveniently found by applying a Fourier transform. The final time evolution of the order parameter is therefore given by,

$$\Psi(t + \Delta t) \approx e^{\frac{-i\Delta t U_{tot}}{2\hbar}} \mathcal{F}^{-1}[e^{\frac{-i\Delta t p^2}{2m\hbar}} \mathcal{F}[e^{\frac{-i\Delta t U_{tot}}{2\hbar}} \Psi(t)]], \tag{4.13}$$

Where $\mathcal{F}$ denotes the (discrete) fourier transform which transforms functions of position, x to momentum, p.

4.3 Cluster Formation

In this work, we numerically study the conditions under which linear vortex structures, imprinted onto a trapped BECs, can evolve into vortex clusters. The system under investigation has been chosen with an eye to possible experimental implementations, as vortices can be controllably imprinted on ultracold atomic samples [77, 89]. Our configuration of choice is the case of simple one-dimensional linear structures which are symmetrical about the centre of the cloud. This layout has a symmetry that is expected to favour the formation of clusters, but also has the characteristic of being geometrically very different from clusters. This combination allows us to observe the dynamical formation of the clusters and determine under which initial imprinting conditions such dynamics happen. In particular, we study the clustering dynamics of arrangements of N_v vortices arranged on a line passing through the centre of the cloud, with a symmetric uniform distribution of vortices on each side. While similar configurations in an anisotropic cloud have been considered in the past where the ordering of the linear layout is not destroyed [90], our isotropic system gives rise to clusters with rich dynamics. For concreteness, we will consider $N = 5 \times 10^4$ ^{87}Rb atoms trapped in a harmonic potential with trapping frequencies $\omega_x = \omega_y = \omega_\perp$ and $\omega_z = \lambda\omega_\perp$ in the radial and transverse directions respectively, with $\lambda = 15$ and $\omega_\perp = 2\pi \times 20$ Hz. We numerically simulate our system on a 256 by 256 by 16 grid. The strong anisotropy between radial and transverse directions allows us to treat our system effectively as a 2D BEC where the vortices are constrained to move in the plane as their bending would be energetically unfavourable.

To initiate the dynamics that generates the vortex clusters, at $t = 0$ we imprint on the condensate a spatially dependent phase profile of the form

$$\phi(x, y) == 2 \sum_{n=1}^{N_v} s_n \tan^{-1}\left(\frac{y - y_n}{\sqrt{(x - x_n)^2 + (y - y_n)^2} + x - x_n}\right), \tag{4.14}$$

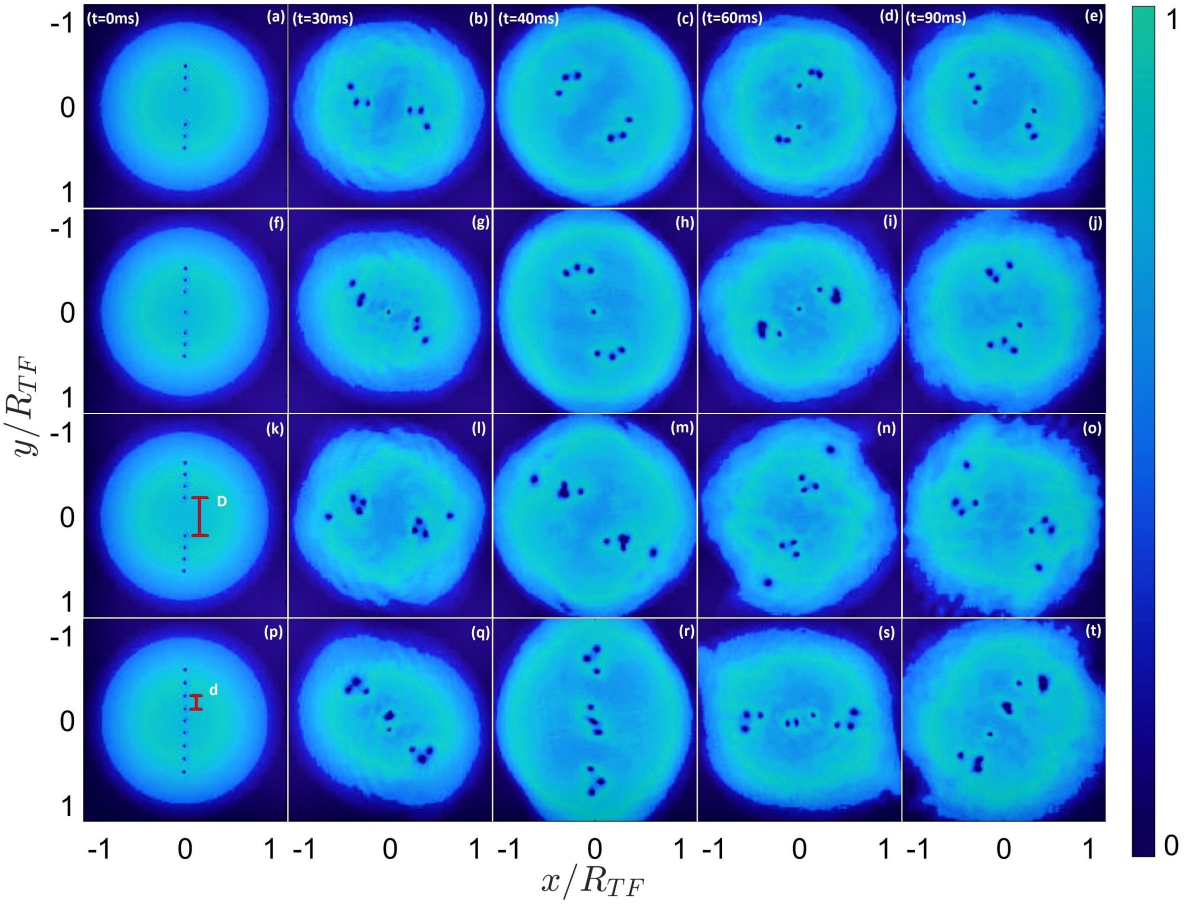


Figure 4.1: Snapshots of the column density in the xy plane over time. The evolution time for each panel is indicated in the top row. Distances are normalised to the Thomas-Fermi radius R_{TF}. The red segments in panels (k) and (p) correspond to D and d respectively, as defined in Sec. II. The colour scale corresponds to the column density value normalised to the maximum in each panel. The top row shows $N_v = 6$ vortices with $D = 0.414R_{TF}$ and $d = 0.138R_{TF}$. The second row shows $N_v = 7$ vortices with $D = 0.48R_{TF}$ and $d = 0.138R_{TF}$. The third row shows $N_v = 8$ vortices with $D = 0.44R_{TF}$ and $d = 0.138R_{TF}$. The bottom row shows $N_v = 9$ vortices with $D = 0.274R_{TF}$ and $d = 0.154R_{TF}$.

where s_n is the vortex charge for the n-th vortex and (x_n, y_n) are the coordinates of the n-th vortex. We arrange a number of vortices, N_v, in two groups symmetrically along a common diameter of the cloud. Within each of these groups, we choose a constant nearest-neighbour distance, d (see fig.4.1p). The closest distance between the two groups is then parameterised by D (so, excluding the central vortex of the line in case of odd N_v, D is the distance between the two inner-most vortices) as depicted in the first column of Fig.4.1. In the cases where there is an odd vortex number, we also include a vortex at the centre of the cloud. All vortex lines run parallel to the z-axis. As soon as the vortices are imprinted, they begin to precess around

the centre of the cloud in a direction given by the sign of the imprinted topological charge (see fig. 4.1). Because the precession frequency is an increasing function of distance from the centre of the cloud, the outer vortices rotate faster than the inner ones, leading to the line bending into an 's'-shape. Without vortex-vortex interactions, one would expect that this bending would become more and more exaggerated, leading the vortices to wind into a spiral configuration with each vortex remaining at its original radial distance from the centre of the cloud. However, the existence of vortex-vortex interactions, although repulsive, gives rise to dynamics that leads to the creation of vortex clusters. In particular, as the interaction scales inversely with the distance between vortices, the vortices tend to rotate around their closest neighbours, causing the linear structure to break into clusters, as shown in Fig.4.1. Once formed, the vortex clusters rotate around their centroids, and continue to precess around the centre of the cloud. Typically, the arrangements of clusters remain well separated from one another and maintain the symmetry of the initial state, forming two identical antipodal clusters or two antipodal clusters and an additional one in the centre, depending whether N_v is even or odd.

Depending on the number of vortices imprinted and the distances d and D, we observe a range of different clustering dynamics. An example of the simplest kind of dynamics is reported in the first row of Fig.4.1. We observe this dynamics when $D \gg d$, therefore when the vortices are already imprinted into two fairly separated groups, and when N_v is even. The dynamics that follows the imprinting essentially keeps the overall symmetry, and the two lines of vortices evolve into two separated clusters that orbit around their centroids. The inner cluster dynamics is quite complex, in the sense that the two clusters change their shape often, however, as we discuss later on, the average distance between the vortices in the cluster and the distance between the clusters do not substantially change. We observe similar dynamics when $D \gg d$ and N_v is odd. An example is shown in the second row of Fig.4.1. In this case, the central vortex remains stationary while the antipodal clusters form and begin to evolve as described previously. However, this central vortex will eventually be perturbed and move from the centre, usually joining one of the existing clusters (an example of this can be seen in Fig.4.1i-j). Once the central vortex moves, the symmetry of the system breaks and the clusters are perturbed. The

perturbed cluster ceases to be tightly bound and its dynamics is no longer a simple revolution around its centroid, while the centroid itself changes.

The clustering dynamics becomes richer as N_v increases. An example is shown in the third row of Fig. 4.1, with $N_v = 8$ and $D \gg d$. In this case we observe that the dynamics that follows the imprinting generates clusters with a satellite vortex. These are formations of strongly-bound clusters that revolve around their centroids, similarly to what previously described, with an additional vortex that revolves around them. The satellite vortices are at a distance from the others that doesn't allow them to be considered part of the cluster, nor to be considered as stray vortices. Another kind of clustering dynamics is shown in the fourth row of Fig.4.1, for $N_v = 9$ and $D \simeq 2d$. Here we observe the formation of three clusters. The third cluster forms around the central vortex and remains stable until it is perturbed by the other two (Fig.4.1t).

As we discuss in Sec. 4.5, we do not observe any clustering dynamics for small values of D, where the initial configuration of the imprinted vortices causes the trajectories to tangle and does not allow the formation of well separated clusters. We also do not not observe clustering for large values of d, where the vortices fail to capture one another in their velocity fields.

4.4 Cluster Detection

Various algorithms and statistical methods have been used to devise clustering measures in a 2D Bose-Einstein Condensate in systems of 2D decaying quantum turbulence [91, 92] and low vortex-number systems [93]. To provide a quantitative description of the clustering dynamics and to determine when a cluster has been formed, we have applied the Hierarchical Agglomerative Clustering algorithm [94]. The quantitative definition of a cluster is indeed a common problem in statistical theory and its modern machine learning applications [94], where clusters of similar objects are detected based on similarity of their features in a multi-dimensional space. In our system we seek clusters in a Euclidean two-dimensional geometry. The clustering algorithm detects clusters by analysing the positions of the vortices with no external input besides the definition of the algorithm's metrics. The only assumption is that we are able to accurately

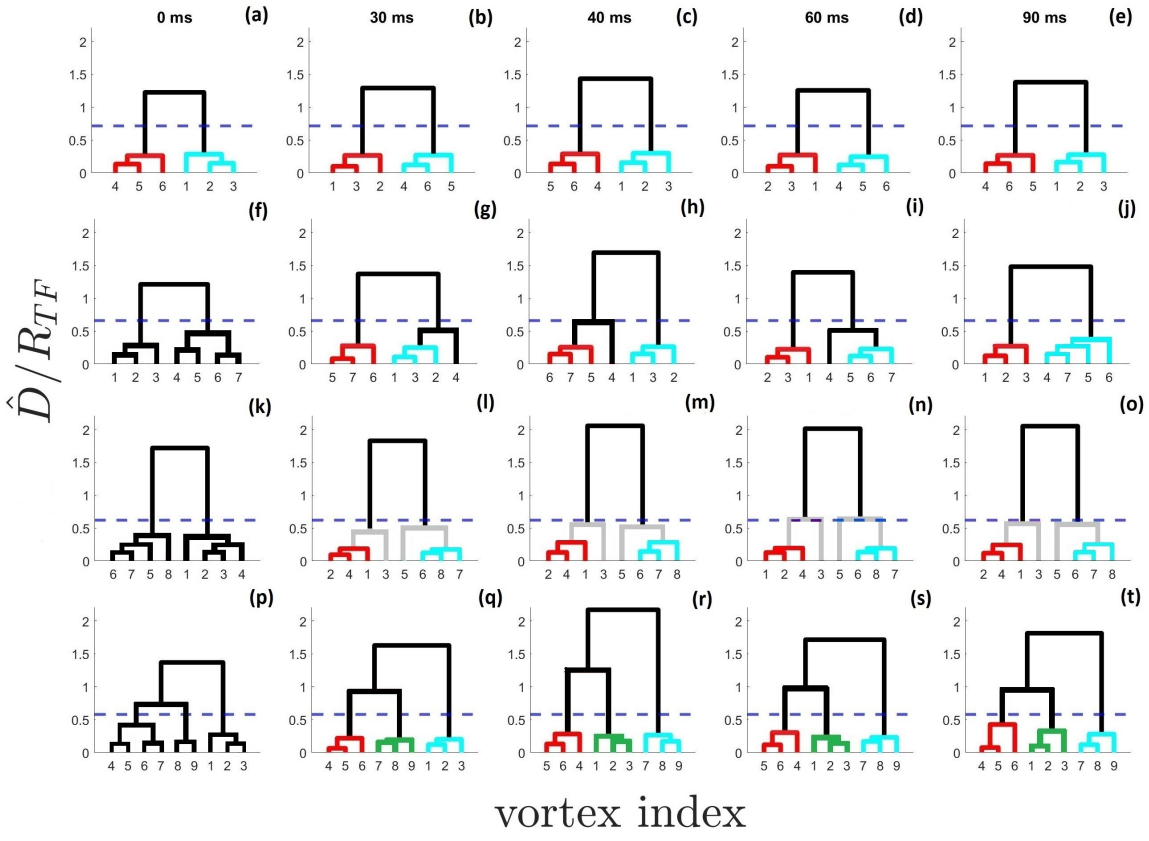


Figure 4.2: Dendrogram for the hierarchical agglomerative algorithm for the same data as Fig.4.1. The evolution time for each panel is indicated in the top row. The merging distances $\hat{D}$ computed by the clustering algorithm are normalised to R_{TF}. The horizontal dashed line in each panel corresponds to δ. The first row corresponds to $N_v = 6$ vortices. The algorithm detects two clusters of three vortices each, highlighted with different colours. The second row shows the case of $N_v = 7$ vortices. The third row is for the case of $N_v = 8$ vortices, where the grey branches identify the 'satellite', vortices. The bottom row is for the case of $N_v = 9$ vortices, where three clusters are formed, identified with different colours.

describe the trajectories of the individual vortices. This is a reasonable assumption for our case of interest that consists of well separated vortex cores.

The algorithm starts by treating each vortex as an individual cluster, and then it iteratively attempts to merge the clusters in larger clusters following a bottom-up approach, according to the Ward criterion [95]. The selection of the optimal pair to be joined at each step is based on the distance metric

$$\hat{D} = \sqrt{2\frac{n_r n_s}{n_r + n_s}}\|\mathbf{r}_r - \mathbf{r}_s\|, \tag{4.15}$$

where n_r and n_s are the number of elements in each of two clusters r and s respectively that are under consideration. Similarly, $\mathbf{r}_r$ and $\mathbf{r}_s$ are the positions of their centroids. At each step, the clusters with the minimum pairwise distance are connected. The distance is also proportional to the square root of the harmonic mean of the number of elements in each of the two cluster to be joined. The clusters appear as distinct formations in the dendrogram output of the algorithm, see Fig. 4.2. A strongly bound cluster is characterised by a short merging distance and large difference to the next merging point in the dendrogram.

Each panel in Fig. 4.2 corresponds to the same panel in Fig. 4.1. The dashed horizontal lines correspond to the average inter-vortex distance for uniform distributions of vortices, which is $\delta = \sqrt{\pi/N_v}R_{TF}/2$, for the same sets of parameters. In general, clusters must satisfy $\hat{D} \ll \delta$. It is important to note that δ is not a parameter of the algorithm but only a reference point for our interpretation of the results compared to a purely random layout. The first row of Fig. 4.2 shows that when $D \gg d$ and N_v is even, one can already consider the imprinted pattern as two separate clusters (highlighted with different colours). The following dynamics essentially does not alter the clusters that keep their intra- and inter- distances roughly the same as the initial pattern. The case with $D \gg d$ and N_v odd is instead shown in the second row. After the initial imprinting, two three-vortex clusters are rapidly formed while the remaining seventh vortex orbits at a distance $\simeq \delta$ from one of the clusters, therefore we can't consider it part of any cluster. The dendrogram remains essentially stationary until $t = 90$ ms, where it shows that the seventh vortex is finally incorporated in one of the clusters.

The third row of Fig. 4.2 reports the case of $N_v = 8$ vortices. The dendrogram shows that two

three-vortex clusters are clearly formed at a distance well below δ, while each of the remaining vortices have a merging distance to one of the clusters near δ. The fact that the merging distance of the fourth vortex is close to δ confirms the fact that it can only be considered as a satellite vortex and not part of the cluster itself. Interestingly the cluster-plus-satellite formations remain stable and stationary for as long as we follow their dynamics. This is a phenomenon that could not be predicted a-priori and is only discovered by the algorithm. The bottom row of Fig. 4.2 finally reports the dendrograms for the case of $N_v = 9$ vortices. Shortly after the imprinting, the algorithm clearly identifies three very tightly bound clusters that remain well separated and stationary for most of the dynamics. Towards $t = 90$ ms we observe that the clusters start to slightly weaken their binding, and for longer times we observe that the clusters dissolve.

4.5 Vortex Dynamics

As just discussed, the initial imprinting gives rise to a range of different dynamics depending on the number of vortices N_v and the distances d and D. However, not every imprinting configuration generates stable or quasi-stable clusters. To explore the range of parameters that lead to the formation of clusters, we utilise an effective particle model. This approach allows us to scan the space of parameters more easily than GPE simulations. In this simplified model the vortices are treated as point-like objects in a 2D space. The use of such a model, which also excludes effects from vortex line curvature and effects of vortex-phonon coupling, is justified in a quasi-2D system such as the one we consider. The motion of each vortex can be ascribed to two constituent factors. The first is the precession induced by the inhomogeneous atomic density profile of the condensate, while the second is the effect of pairwise interactions between the vortices. The latter can be explained as the motion that is induced on every point of a vortex in a pair due to the fluid flow that is generated by the other vortex of the pair.

As has been shown in [96] the dynamics of the vortices can be expressed in the following

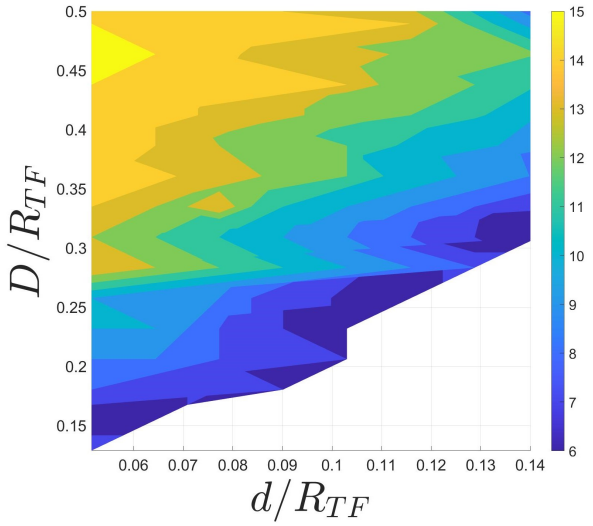


Figure 4.3: Maximum N_v of imprinted vortices that can generate clusters as a function of d and D. The white region corresponds to configurations that either don't produce clusters or can only produce clusters of two vortices. The non-smooth boundaries of the contours indicate the breakdown of the qualitative agreement between the ODE and GPE solutions.

system of first order ordinary differential equations (ODEs),

$$\dot{w_k} = iw_k\left(\Omega_p \frac{s_k}{1-|w_k|^2} + \Omega_I \sum_{j\neq k} \frac{s_j}{w_j^* w_k - |w_k|^2}\right), \tag{4.16}$$

with s_k the topological charge of the vortex ($= \pm 1$), $w_k = z_k/R_{TF}$ the position of the k-th vortex, written as a complex number (i.e. $z_k = x_k + iy_k$), normalised to the Thomas-Fermi radius, R_{TF} of the cloud. The first term in equation 4.16 corresponds to the precession of the vortex around the cloud while the second term corresponds to the interactions. The two frequencies controlling the relative strengths of these two effects are given by[97],

$$\Omega_p = \frac{(3+\frac{1}{5\lambda^2})\hbar}{2mR_{TF}^2}\ln\left(\frac{R_{TF}}{\xi}\right), \tag{4.17}$$

$$\Omega_I = b\frac{\hbar}{2mR_{TF}^2}. \tag{4.18}$$

where ξ is the healing length, and b is an empirically determined parameter which modifies the strength of interactions.

We implemented Equation 4.16 in a numerical ODE solver, using a ratio of $\Omega_p/\Omega_I \approx 9$, corresponding to the same values as simulated using the GPE. By comparing the dynamics observed in the ODE solver to those obtained by the numerical solution of the GPE, we found that the rotation period of the vortex clusters matched when $b = 1.35$. This agrees with the value used in [96].

By running simulations of the ODE system for various values of the D, d and N_v parameters, we extract a clear region in which clustering occurs, shown in Fig. 4.3. Fig. 4.3 shows the maximum number of vortices that can be imprinted, which generates clusters. For every N_v smaller than this maximum value, we observe cluster formation. The configuration space of Fig. 4.3 shows that there is a strong relationship between the distance parameters D and d -according to which the initial imprinting of the vortices is configured- and the number of vortices that can cluster. We also observe good agreement between the ODE and the GPE solutions on whether clustering is observed for different values of d, D and N_v, except in cases which are very close to the boundary between clustered and unclustered states. As discussed, different initial D and d parameters lead to different cluster formations. We observe that a relatively large D value compared to d always lead to distinct clusters, even when the number of vortices is as high as 15. For odd and large number of vortices, we observe the formation of a central cluster in addition to the antipodal ones. As expected, for lower values of D and higher values of d the formation of clusters is hindered, and more complex dynamics occur.

4.6 Cluster Dynamics

By treating the clusters as the objects of interest, we can extend the model developed in the previous section. This further simplifies the system by reducing the degrees of freedom but keeping the salient features of the system dynamics. In order to make a model of the dynamics of the clusters as opposed to their constituent vortices, we should first check whether the internal dynamics of a vortex cluster are important. In fact, in the case of a cluster of vortices in the absence of any external vortices or precession effects due to the shape of the cloud, it can be

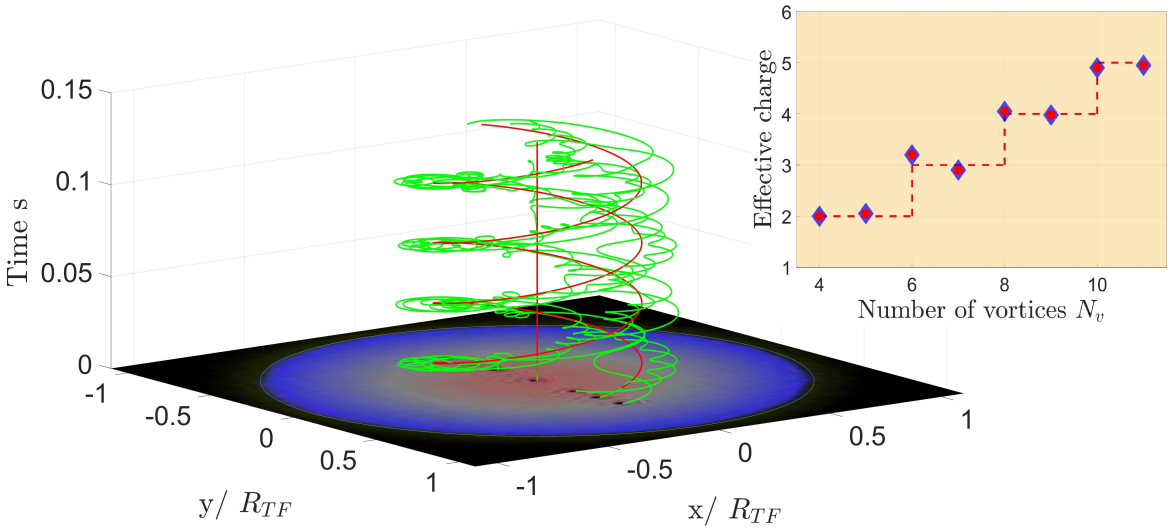


Figure 4.4: Comparison of the period of revolution and the dynamics of the clusters against the period of revolution of the composite object in the simplified system leads to an effective charge for the composite object for which a similar period is observed between the two systems. There is a good agreement of the dynamics between the simplified system (red trajectories) and the original system consisting of 7 vortices (green trajectories) . The embedded figure shows the agreement of the effective charge of the simplified ODE system (composite object) on the vertical axis and the sum of the vortex charges in the cluster of the full ODE system. For a system with N_v vortices the effective charge agrees with the sum of the individual cluster (the integer part of $N_v/2$).

shown that the centroid position of any group of vortices with the same topological charge remains fixed.

We define the cluster position to be its centroid,

$$C = \frac{1}{N}\sum_{k=1}^{N} w_k. \tag{4.19}$$

Then, using 4.16, the equation of motion for this centroid is,

$$\dot{C} = \frac{i\Omega_I s}{N}\sum_{k=1}^{N}\sum_{j=1}^{N}\begin{cases} 0 & j = k \\ \frac{1}{(w_j - w_k)^*} & j \neq k, \end{cases} \tag{4.20}$$

where we set $\Omega_p = 0$ to remove the effects of precession due to the cloud density, and only summed over the N vortices within the cluster, thus eliminating the effects of interactions with the rest of the system. Clearly, from the anti-symmetry under dummy-index interchange, this is

gives $\dot{C} = 0$. In other words, an isolated cluster of vortices on a flat background won't move on it's own, in the same way that a single isolated vortex wouldn't.

It follows from this that if we consider small clusters such that the effects of their differing positions in the velocity fields due to external vortices and the shape of the cloud is negligible, we may discard all of the internal dynamics of a cluster and consider it to be a single object, with its position taken to be the centroid of its constituent vortices.

The velocity of a vortex cluster centroid due to external sources such as those produced by the cloud shape or the effects of other vortices and clusters is equal to the mean of the velocity of its constituent vortices, which in turn depend only on their positions. As we consider small clusters, we can take the velocity of a vortex cluster to be the same as that of a single constituent vortex at the centroid position.

The effect of the cluster on an external vortex (or vortex cluster) is the sum of the velocity fields of all of its constituent vortices. If we assume that all external vortices have distances from the cluster much larger than the size of the cluster, we can simply treat the cluster as a vortex with a charge equal to the total charge of its constituent vortices.

These observations allow us to generalise equation 4.16 to one describing the dynamics of clusters of 1 or more vortices,

$$\dot{w_k} = i w_k \left(\Omega_p \frac{s_k}{1 - |w_k|^2} + \Omega_I \sum_{j \neq k} \frac{s_j n_j}{w_j^* w_k - |w_k|^2} \right), \tag{4.21}$$

where the positions w_i and charges s_i now refer to the centroid positions and topological charges per vortex of a cluster, and n_i gives the number of vortices found in the cluster labelled i. This model is only applicable for clusters formed from vortices of the same charge, however, due to the instability of vortices with absolute charges greater than one, this is the case of primary interest.

To test the validity of this model, it was implemented in the same numerical ODE solver as equation 4.16. The period of rotation was used as the comparison factor between the simulations of the two models, and it was found to be in a really good agreement (see figure 4.4). Specifically,

for the case of even N_v the line segments consisting of $\lfloor N_v/2 \rfloor$ vortices, when clustered as per the configuration space of fig.4.3 were replaced by an object with an effective charge that turns out to be in a very good agreement with the expected sum of charges in the cluster. For the cases of an odd number of vortices, the central vortex remains unchanged while the symmetrical line segments with respect to the cloud are replaced with an object of an effective charge. The effective charges in both cases show a very good agreement with the expected total sum of charges in a cluster. In systems which are large enough to support multiple levels of length scale separation, we expect that one may observe this clustering process occur recursively, i.e. if there are many clusters which are well separated, they may form 'superclusters' in which each small cluster acts in the way that a single vortex does in a normal cluster. With enough length scale separation, this process may continue for multiple levels, however the ratio of cloud size to healing length would have to be very large to support enough clusters with enough distance between them, and the initial arrangements which would form these superclusters is not obvious.

Chapter 5

Conclusions and Outlook

In this thesis I have described the apparatus and methods required to produce ultracold atomic clouds of ^{87}Rb and manipulate them using optical potentials controlled via the use of a DMD. In chapter 1, I introduced many of the key topics required to understand the work, including the basics of the theory of Bose-Einstein condensates, the theory and applications of optical potentials as well as the ideas of synthetic dimensions and quantised vorticity. In chapter 2, I described the experimental apparatus, including the vacuum system and the various optical systems required to generate and image an ultracold sample of ^{87}Rb, including a description of the working principles of magneto-optical traps and all-optical evaporative cooling, along with details of how these are used in our apparatus. I then described the use of the Digital Micromirror Device and how we use it to produce spatially and temporally varying optical optical potentials on the clouds. I have also provided a comparison between the light sources used to produce these optical potentials. From this we can see that while lasers clearly have their place due to their wide range of available wavelengths and high intensity, Superluminescent diodes are also useful when image quality is paramount. In chapter 3, I have explained how we demonstrated an implementation of a synthetic dimension formed from the quantum harmonic oscillator states of our trapping potential, and the production of Bloch oscillations. This work could be extended to 1 real + 1 synthetic dimension by adding a phase variation in the driving oscillation across an elongated real dimension. By doing this, a synthetic magnetic field could be produced, causing

atoms to undergo cyclotron motion in the real-synthetic space. Our scheme would make this an interesting avenue to explore as there is a natural edge to the synthetic dimension in that there are no states lower than the ground state of the harmonic oscillator. An upper edge to the dimension could also be engineered by adding optically generated walls to the driving potential which would restrict the oscillations to lower lying states. Finally walls restricting the motion of atoms along the long real dimension could add edges to that dimension as well. This setup would allow for the investigation of topologically protected edge states. Further to this, one could imagine extending the scheme to a 2D or 3D optical lattice, with driving individually addressing each lattice site. While this would be challenging to implement, it would allow us to study physics in up to 6 spatial dimensions in the case of a 3D lattice with 3 independent driving directions. In Chapter 4, I have described the quantisation of vortices and how we numerically simulated the evolution of systems of specifically chosen arrangements of vortices, as could be implemented in the experiment via the phase imprinting method. In particular, we simulated linear arrangements which were symmetric about the centre of a quasi-2D cloud. I showed that for particular numbers and spacings of vortices, these arrangements quickly form pairs of vortex clusters, while others produces cluster triplets or clusters with satellites. I have also described a hierarchical agglomerative clustering algorithm used to identify cluster states. I then showed the efficacy of a simple analytical model for vortex motion, and extended it to the motion of vortex clusters. This work suggests that in a large enough system with appropriate separation of length scales, there may exist some recursive 'clustering of clusters' and so on.

Finally, I will outline a few directions which the experiment may take in the future. The simulations work on quantised vortices provides a clear avenue for future experimental implementation. Our work on synthetic dimensions and the modifications to out imprinting light sources has also honed our abilities to produce optical potentials with arbitrary spatial and temporal behaviour, which unlocks further projects. Some preliminary work was done to assess the viability of demonstrating the superfluid fountain effect [98] in a cold atomic BEC, which has been simulated numerically [99]. In order to do this, the cloud could be separated into two pieces by raising an optically produced barrier in the centre of the cloud. One half of the cloud

could then be heated before a small channel in the barrier is opened up. The predicted behaviour is that in order to achieve thermodynamic equilibrium, atoms would flow from the cold to the hot side of the barrier. This assumes that the channel is small enough that only the zero viscosity superfluid component of the atomic cloud could flow through it. Because no entropy and thus no heat can be transported by a superfluid, heat could not flow from the hot side to the cold, and therefore the temperature gradient can only be decreased by adding zero-entropy cold atoms to the hot side from the cold side. In our studies we have seen that splitting the cloud into 2 halves is easy, however viewing them separately in time of flight is challenging as they tend to overlap as they expand. This was overcome by adding a kicking potential to force the two half-clouds to pass through each other and separate. It was also challenging to find a method to reliably heat one side of the atomic cloud without losing too many atoms to give a good signal. Finally, the issue of the required channel width is so far unclear. If these issues can be resolved, the system should be able to give a clear demonstration of this predicted effect. As another example of work which may soon be performed on this apparatus, there is potential to investigate the superfluid nature of BECs. Superfluids are characterised by their zero viscosity, and the fact that they do not cause any drag effect on a normal fluid. However, it has been predicted [100] that there is a dispersionless drag between separate superfluids, known as the 'Andreev-Bashkin effect'. In our system, because we use all optical trapping, we are able to make spinor Bose-Einstein Condensates of ^{87}Rb, which can be thought of as a collection of 3 independent BECs (one for each magnetic Zeeman state). These 3 components can be separated spatially by performing a Stern-Gerlach pulse (i.e. free-fall with a magnetic field gradient applied). In principle, it would then be possible to phase imprint quantised vortices onto 2 or more of the components before recombining them with the reverse Stern-Gerlach pulse. Observing any interaction between vortices imprinted in different components would be strong evidence for the Andreev-Bashkin Effect. Lastly, our system would be well placed to produce acoustic black holes (also known as dumb holes). These are simulations of general relativistic black holes whereby an 'event horizon' is generated by creating a region of fluid that moves faster than the local speed of sound. In such a region, phonons would be unable to make progress and escape the fast moving

region. By creating a potential step, a fluid can be separated into regions with different speeds of sound (because the speed of sound is density dependent). If the step is then moved with a speed between these two speeds of sound, in the frame of the step, one region is moving subsonically, and the other supersonically. In implementations of this scheme, entangled Hawking Radiation has been observed [101]. With our very flexible apparatus, it would be possible to vary parameters such as the shape of the step, which may lead to new physics such as massive Hawking radiation.

References

[1] Arthur L. Robinson. "Sodium Atoms Trapped With Laser Light". In: *Science* 233.4764 (1986), pp. 623–623. DOI: 10.1126/science.233.4764.623.a. eprint: https://www.science.org/doi/pdf/10.1126/science.233.4764.623.a. URL: https://www.science.org/doi/abs/10.1126/science.233.4764.623.a.

[2] E. L. Raab et al. "Trapping of Neutral Sodium Atoms with Radiation Pressure". In: *Phys. Rev. Lett.* 59 (23 Dec. 1987), pp. 2631–2634. DOI: 10.1103/PhysRevLett.59.2631. URL: https://link.aps.org/doi/10.1103/PhysRevLett.59.2631.

[3] M. H. Anderson et al. "Observation of Bose-Einstein Condensation in a Dilute Atomic Vapor". In: *Science* 269.5221 (1995), pp. 198–201. DOI: 10.1126/science.269.5221.198. eprint: https://www.science.org/doi/pdf/10.1126/science.269.5221.198. URL: https://www.science.org/doi/abs/10.1126/science.269.5221.198.

[4] K. B. Davis et al. "Bose-Einstein Condensation in a Gas of Sodium Atoms". In: *Phys. Rev. Lett.* 75 (22 Nov. 1995), pp. 3969–3973. DOI: 10.1103/PhysRevLett.75.3969. URL: https://link.aps.org/doi/10.1103/PhysRevLett.75.3969.

[5] B. DeMarco and D. S. Jin. "Onset of Fermi Degeneracy in a Trapped Atomic Gas". In: *Science* 285.5434 (Sept. 1999), pp. 1703–1706. DOI: 10.1126/science.285.5434.1703. URL: https://doi.org/10.1126/science.285.5434.1703.

[6] Nicolas Schlosser et al. "Sub-poissonian loading of single atoms in a microscopic dipole trap". In: *Nature* 411.6841 (June 2001), pp. 1024–1027. ISSN: 1476-4687. DOI: 10.1038/35082512. URL: https://doi.org/10.1038/35082512.

[7] Timothy P. Sofley. "Cold and ultracold molecules in the twenties". In: *Proceedings of the Royal Society A* 497.2274 (June 2023). ISSN: 1471-2946. DOI: 10.1098/rspa.2022.0806. URL: https://doi.org/10.1098/rspa.2022.0806.

[8] Immanuel Bloch. "Ultracold quantum gases in optical lattices". In: *Nature Physics* 1.1 (Oct. 2005), pp. 23–30. ISSN: 1745-2481. DOI: 10.1038/nphys138. URL: https://doi.org/10.1038/nphys138.

[9] L. Madeira et al. "Quantum Turbulence in Quantum Gases". In: *Annual Review of Condensed Matter Physics* 11.1 (2020), pp. 37–56. DOI: 10.1146/annurev-conmatphys-031119-050821. eprint: https://doi.org/10.1146/annurev-conmatphys-031119-050821. URL: https://doi.org/10.1146/annurev-conmatphys-031119-050821.

[10] Bo Zhao and Jian-Wei Pan. "Quantum control of reactions and collisions at ultralow temperatures". In: *Chem. Soc. Rev.* 51 (5 2022), pp. 1685–1701. DOI: 10.1039/D1CS01040A. URL: http://dx.doi.org/10.1039/D1CS01040A.

[11] F. Riehle et al. "Optical Ramsey spectroscopy in a rotating frame: Sagnac effect in a matter-wave interferometer". In: *Phys. Rev. Lett.* 67 (2 July 1991), pp. 177–180. DOI: 10.1103/PhysRevLett.67.177. URL: https://link.aps.org/doi/10.1103/PhysRevLett.67.177.

[12] Rui Xu et al. "Magneto-Optical Traps for Cold Atomic Gravimetry: Research Status and Development Trends". In: *Applied Sciences* 13.10 (2023). ISSN: 2076-3417. DOI: 10.3390/app13106076. URL: https://www.mdpi.com/2076-3417/13/10/6076.

[13] Remi Geiger et al. "High-accuracy inertial measurements with cold-atom sensors". In: *AVS Quantum Science* 2.2 (June 2020), p. 024702. DOI: 10.1116/5.0009093. URL: https://hal.science/hal-02988722.

[14] Andrew D. Ludlow et al. "Optical atomic clocks". In: *Rev. Mod. Phys.* 87 (2 June 2015), pp. 637–701. DOI: 10.1103/RevModPhys.87.637. URL: https://link.aps.org/doi/10.1103/RevModPhys.87.637.

[15] G. Barontini et al. "Measuring the stability of fundamental constants with a network of clocks". In: *EPJ Quantum Technology* 9.1 (May 2022), p. 12. ISSN: 2196-0763. DOI: 10.1140/epjqt/s40507-022-00130-5. URL: https://doi.org/10.1140/epjqt/s40507-022-00130-5.

[16] L. Badurina et al. "AION: an atom interferometer observatory and network". In: *Journal of Cosmology and Astroparticle Physics* 2020.05 (May 2020), p. 011. DOI: 10.1088/1475-7516/2020/05/011. URL: https://dx.doi.org/10.1088/1475-7516/2020/05/011.

[17] Tanya S. Roussy et al. "An improved bound on the electron's electric dipole moment". In: *Science* 381.6653 (2023), pp. 46–50. DOI: 10.1126/science.adg4084. eprint: https://www.science.org/doi/pdf/10.1126/science.adg4084. URL: https://www.science.org/doi/abs/10.1126/science.adg4084.

[18] I. M. Georgescu, S. Ashhab, and Franco Nori. "Quantum simulation". In: *Rev. Mod. Phys.* 86 (1 Mar. 2014), pp. 153–185. DOI: 10.1103/RevModPhys.86.153. URL: https://link.aps.org/doi/10.1103/RevModPhys.86.153.

[19] Immanuel Bloch, Jean Dalibard, and Wilhelm Zwerger. "Many-body physics with ultracold gases". In: *Rev. Mod. Phys.* 80 (3 July 2008), pp. 885–964. DOI: 10.1103/RevModPhys.80.885. URL: https://link.aps.org/doi/10.1103/RevModPhys.80.885.

[20] W Hofstetter and T Qin. "Quantum simulation of strongly correlated condensed matter systems". In: *Journal of Physics B: Atomic, Molecular and Optical Physics* 51.8 (Mar. 2018), p. 082001. DOI: 10.1088/1361-6455/aaa31b. URL: https://dx.doi.org/10.1088/1361-6455/aaa31b.

[21] Tomoki Ozawa and Hannah M. Price. "Topological quantum matter in synthetic dimensions". In: *Nature Reviews Physics* 1.5 (May 2019), pp. 349–357. ISSN: 2522-5820. DOI: 10.1038/s42254-019-0045-3. URL: https://doi.org/10.1038/s42254-019-0045-3.

[22] P. C. Haljan et al. "Driving Bose-Einstein-Condensate Vorticity with a Rotating Normal Cloud". In: *Phys. Rev. Lett.* 87 (21 Nov. 2001), p. 210403. DOI: 10.1103/PhysRevLett.87.210403. URL: https://link.aps.org/doi/10.1103/PhysRevLett.87.210403.

[23] Bogdan Damski, Krzysztof Sacha, and Jakub Zakrzewski. "Stirring a Bose–Einstein condensate". In: *Journal of Physics B: Atomic, Molecular and Optical Physics* 35.19 (Sept. 2002), p. 4051. DOI: 10.1088/0953-4075/35/19/308. URL: https://dx.doi.org/10.1088/0953-4075/35/19/308.

[24] Ł. Dobrek et al. "Optical generation of vortices in trapped Bose-Einstein condensates". In: *Phys. Rev. A* 60 (5 Nov. 1999), R3381–R3384. DOI: 10.1103/PhysRevA.60.R3381. URL: https://link.aps.org/doi/10.1103/PhysRevA.60.R3381.

[25] Alexander L. Gaunt et al. "Bose-Einstein Condensation of Atoms in a Uniform Potential". In: *Phys. Rev. Lett.* 110 (20 May 2013), p. 200406. DOI: 10.1103/PhysRevLett.110.200406. URL: https://link.aps.org/doi/10.1103/PhysRevLett.110.200406.

[26] K Henderson et al. "Experimental demonstration of painting arbitrary and dynamic potentials for Bose–Einstein condensates". In: *New Journal of Physics* 11.4 (Apr. 2009), p. 043030. DOI: 10.1088/1367-2630/11/4/043030. URL: https://doi.org/10.1088/1367-2630/11/4/043030.

[27] G. Gauthier et al. "Direct imaging of a digital-micromirror device for configurable microscopic optical potentials". In: *Optica* 3.10 (Oct. 2016), pp. 1136–1143. DOI: 10.1364/OPTICA.3.001136. URL: http://www.osapublishing.org/optica/abstract.cfm?URI=optica-3-10-1136.

[28] Philip Zupancic et al. "Ultra-precise holographic beam shaping for microscopic quantum control". In: *Opt. Express* 24.13 (June 2016), pp. 13881–13893. DOI: 10.1364/OE.24.013881. URL: http://www.opticsexpress.org/abstract.cfm?URI=oe-24-13-13881.

[29] C. J. Pethick, Thomas Schaefer, and A. Schwenk. *Bose-Einstein condensates in neutron stars*. 2015. arXiv: 1507.05839 [nucl-th].

[30] Franco Dalfovo et al. "Theory of Bose-Einstein condensation in trapped gases". In: *Rev. Mod. Phys.* 71 (3 Apr. 1999), pp. 463–512. DOI: 10.1103/RevModPhys.71.463. URL: https://link.aps.org/doi/10.1103/RevModPhys.71.463.

[31] Rudolf Grimm, Matthias Weidemüller, and Yurii B. Ovchinnikov. "Optical Dipole Traps for Neutral Atoms". In: ed. by Benjamin Bederson and Herbert Walther. Vol. 42. Advances In Atomic, Molecular, and Optical Physics. Academic Press, 2000, pp. 95–170. DOI: https://doi.org/10.1016/S1049-250X(08)60186-X. URL: https://www.sciencedirect.com/science/article/pii/S1049250X0860186X.

[32] Daniel A. Steck. *Alkali D Line Data*. 2001. URL: https://steck.us/alkalidata/ (visited on 08/11/2023).

[33] O. Boada et al. "Quantum Simulation of an Extra Dimension". In: *Phys. Rev. Lett.* 108 (13 Mar. 2012), p. 133001. DOI: 10.1103/PhysRevLett.108.133001. URL: https://link.aps.org/doi/10.1103/PhysRevLett.108.133001.

[34] Eric J. Meier, Fangzhao Alex An, and Bryce Gadway. "Observation of the topological soliton state in the Su–Schrieffer–Heeger model". In: *Nature Communications* 7.1 (Dec. 2016), p. 13986. ISSN: 2041-1723. DOI: 10.1038/ncomms13986. URL: https://doi.org/10.1038/ncomms13986.

[35] Konrad Viebahn et al. "Matter-Wave Diffraction from a Quasicrystalline Optical Lattice". In: *Phys. Rev. Lett.* 122 (11 Mar. 2019), p. 110404. DOI: 10.1103/PhysRevLett.122.110404. URL: https://link.aps.org/doi/10.1103/PhysRevLett.122.110404.

[36] Han Cai et al. "Experimental Observation of Momentum-Space Chiral Edge Currents in Room-Temperature Atoms". In: *Phys. Rev. Lett.* 122 (2 Jan. 2019), p. 023601. DOI: 10.1103/PhysRevLett.122.023601. URL: https://link.aps.org/doi/10.1103/PhysRevLett.122.023601.

[37] Bhuvanesh Sundar, Bryce Gadway, and Kaden R. A. Hazzard. "Synthetic dimensions in ultracold polar molecules". In: *Scientific Reports* 8.1 (Feb. 2018), p. 3422. ISSN: 2045-2322. DOI: 10.1038/s41598-018-21699-x. URL: https://doi.org/10.1038/s41598-018-21699-x.

[38] Jin Hyoun Kang, Jeong Ho Han, and Y Shin. "Creutz ladder in a resonantly shaken 1D optical lattice". In: *New Journal of Physics* 22.1 (Jan. 2020), p. 013023. DOI: 10.1088/1367-2630/ab61d7. URL: https://dx.doi.org/10.1088/1367-2630/ab61d7.

[39] A. Celi et al. "Synthetic Gauge Fields in Synthetic Dimensions". In: *Phys. Rev. Lett.* 112 (4 Jan. 2014), p. 043001. DOI: 10.1103/PhysRevLett.112.043001. URL: https://link.aps.org/doi/10.1103/PhysRevLett.112.043001.

[40] M. Mancini et al. "Observation of chiral edge states with neutral fermions in synthetic Hall ribbons". In: *Science* 349.6255 (2015), pp. 1510–1513. DOI: 10.1126/science.aaa8736. eprint: https://www.science.org/doi/pdf/10.1126/science.aaa8736. URL: https://www.science.org/doi/abs/10.1126/science.aaa8736.

[41] B. K. Stuhl et al. "Visualizing edge states with an atomic Bose gas in the quantum Hall regime". In: *Science* 349.6255 (2015), pp. 1514–1518. DOI: 10.1126/science.aaa8515. eprint: https://www.science.org/doi/pdf/10.1126/science.aaa8515. URL: https://www.science.org/doi/abs/10.1126/science.aaa8515.

[42] L. F. Livi et al. "Synthetic Dimensions and Spin-Orbit Coupling with an Optical Clock Transition". In: *Phys. Rev. Lett.* 117 (22 Nov. 2016), p. 220401. DOI: 10.1103/PhysRevLett.117.220401. URL: https://link.aps.org/doi/10.1103/PhysRevLett.117.220401.

[43] S. Kolkowitz et al. "Spin–orbit-coupled fermions in an optical lattice clock". In: *Nature* 542.7639 (Feb. 2017), pp. 66–70. ISSN: 1476-4687. DOI: 10.1038/nature20811. URL: https://doi.org/10.1038/nature20811.

[44] Thomas Chalopin et al. "Probing chiral edge dynamics and bulk topology of a synthetic Hall system". In: *Nature Physics* 16.10 (Oct. 2020), pp. 1017–1021. ISSN: 1745-2481. DOI: 10.1038/s41567-020-0942-5. URL: https://doi.org/10.1038/s41567-020-0942-5.

[45] Vincent Lienhard et al. "Realization of a Density-Dependent Peierls Phase in a Synthetic, Spin-Orbit Coupled Rydberg System". In: *Phys. Rev. X* 10 (2 May 2020), p. 021031.

DOI: 10.1103/PhysRevX.10.021031. URL: https://link.aps.org/doi/10.1103/PhysRevX.10.021031.

[46] S. K. Kanungo et al. "Realizing topological edge states with Rydberg-atom synthetic dimensions". In: *Nature Communications* 13.1 (Feb. 2022). DOI: 10.1038/s41467-022-28550-y. URL: https://doi.org/10.1038%2Fs41467-022-28550-y.

[47] Eran Lustig et al. "Photonic topological insulator in synthetic dimensions". In: *Nature* 567.7748 (Mar. 2019), pp. 356–360. ISSN: 1476-4687. DOI: 10.1038/s41586-019-0943-7. URL: https://doi.org/10.1038/s41586-019-0943-7.

[48] Avik Dutt et al. "A single photonic cavity with two independent physical synthetic dimensions". In: *Science* 367.6473 (2020), pp. 59–64. DOI: 10.1126/science.aaz3071. eprint: https://www.science.org/doi/pdf/10.1126/science.aaz3071. URL: https://www.science.org/doi/abs/10.1126/science.aaz3071.

[49] Armandas Balč ytis et al. "Synthetic dimension band structures on a Si CMOS photonic platform". In: *Science Advances* 8.4 (Jan. 2022). DOI: 10.1126/sciadv.abk0468. URL: https://doi.org/10.1126%2Fsciadv.abk0468.

[50] Hao Chen et al. "Real-time observation of frequency Bloch oscillations with fibre loop modulation". In: *Light: Science & Applications* 10.1 (Mar. 2021), p. 48. ISSN: 2047-7538. DOI: 10.1038/s41377-021-00494-w. URL: https://doi.org/10.1038/s41377-021-00494-w.

[51] Kai Wang et al. "Generating arbitrary topological windings of a non-Hermitian band". In: *Science* 371.6535 (2021), pp. 1240–1245. DOI: 10.1126/science.abf6568. eprint: https://www.science.org/doi/pdf/10.1126/science.abf6568. URL: https://www.science.org/doi/abs/10.1126/science.abf6568.

[52] Eric J. Meier et al. "Observation of the topological Anderson insulator in disordered atomic wires". In: *Science* 362.6417 (2018), pp. 929–933. DOI: 10.1126/science.aat3406. eprint: https://www.science.org/doi/pdf/10.1126/science.aat3406. URL: https://www.science.org/doi/abs/10.1126/science.aat3406.

[53] H. M. Price et al. "Four-Dimensional Quantum Hall Effect with Ultracold Atoms". In: *Phys. Rev. Lett.* 115 (19 Nov. 2015), p. 195303. DOI: 10.1103/PhysRevLett.115.195303. URL: https://link.aps.org/doi/10.1103/PhysRevLett.115.195303.

[54] Fangzhao Alex An et al. "Nonlinear Dynamics in a Synthetic Momentum-State Lattice". In: *Phys. Rev. Lett.* 127 (13 Sept. 2021), p. 130401. DOI: 10.1103/PhysRevLett.127.130401. URL: https://link.aps.org/doi/10.1103/PhysRevLett.127.130401.

[55] Hannah M. Price, Tomoki Ozawa, and Nathan Goldman. "Synthetic dimensions for cold atoms from shaking a harmonic trap". In: *Phys. Rev. A* 95 (2 Feb. 2017), p. 023607. DOI: 10.1103/PhysRevA.95.023607. URL: https://link.aps.org/doi/10.1103/PhysRevA.95.023607.

[56] G. Salerno et al. "Quantized Hall Conductance of a Single Atomic Wire: A Proposal Based on Synthetic Dimensions". In: *Phys. Rev. X* 9 (4 Oct. 2019), p. 041001. DOI: 10.1103/PhysRevX.9.041001. URL: https://link.aps.org/doi/10.1103/PhysRevX.9.041001.

[57] Georg Wirth, Matthias Ölschläger, and Andreas Hemmerich. "Evidence for orbital superfluidity in the P-band of a bipartite optical square lattice". In: *Nature Physics* 7.2 (Feb. 2011), pp. 147–153. ISSN: 1745-2481. DOI: 10.1038/nphys1857. URL: https://doi.org/10.1038/nphys1857.

[58] Torben Müller et al. "State Preparation and Dynamics of Ultracold Atoms in Higher Lattice Orbitals". In: *Phys. Rev. Lett.* 99 (20 Nov. 2007), p. 200405. DOI: 10.1103/PhysRevLett.99.200405. URL: https://link.aps.org/doi/10.1103/PhysRevLett.99.200405.

[59] Xiaopeng Li and W Vincent Liu. "Physics of higher orbital bands in optical lattices: a review". In: *Reports on Progress in Physics* 79.11 (Sept. 2016), p. 116401. DOI: 10.1088/0034-4885/79/11/116401. URL: https://dx.doi.org/10.1088/0034-4885/79/11/116401.

[60] Dong Hu et al. "Ramsey interferometry with trapped motional quantum states". In: *Communications Physics* 1.1 (June 2018), p. 29. ISSN: 2399-3650. DOI: 10.1038/s42005-018-0030-7. URL: https://doi.org/10.1038/s42005-018-0030-7.

[61] S. van Frank et al. "Interferometry with non-classical motional states of a Bose–Einstein condensate". In: *Nature Communications* 5.1 (May 2014), p. 4009. ISSN: 2041-1723. DOI: 10.1038/ncomms5009. URL: https://doi.org/10.1038/ncomms5009.

[62] V Guarrera et al. "Microwave-dressed state-selective potentials for atom interferometry". In: *New Journal of Physics* 17.8 (Aug. 2015), p. 083022. DOI: 10.1088/1367-2630/17/8/083022. URL: https://dx.doi.org/10.1088/1367-2630/17/8/083022.

[63] Sai Vinjanampathy and Janet Anders. "Quantum thermodynamics". In: *Contemporary Physics* 57.4 (2016), pp. 545–579. DOI: 10.1080/00107514.2016.1201896. eprint: https://doi.org/10.1080/00107514.2016.1201896. URL: https://doi.org/10.1080/00107514.2016.1201896.

[64] H. T. Quan et al. "Quantum thermodynamic cycles and quantum heat engines". In: *Phys. Rev. E* 76 (3 Sept. 2007), p. 031105. DOI: 10.1103/PhysRevE.76.031105. URL: https://link.aps.org/doi/10.1103/PhysRevE.76.031105.

[65] Raam Uzdin, Amikam Levy, and Ronnie Kosloff. "Equivalence of Quantum Heat Machines, and Quantum-Thermodynamic Signatures". In: *Phys. Rev. X* 5 (3 Sept. 2015), p. 031044. DOI: 10.1103/PhysRevX.5.031044. URL: https://link.aps.org/doi/10.1103/PhysRevX.5.031044.

[66] Maxime Ben Dahan et al. "Bloch Oscillations of Atoms in an Optical Potential". In: *Phys. Rev. Lett.* 76 (24 June 1996), pp. 4508–4511. DOI: 10.1103/PhysRevLett.76.4508. URL: https://link.aps.org/doi/10.1103/PhysRevLett.76.4508.

[67] Christoph Bersch, Georgy Onishchukov, and Ulf Peschel. "Experimental observation of spectral Bloch oscillations". In: *Opt. Lett.* 34.15 (Aug. 2009), pp. 2372–2374. DOI: 10.1364/OL.34.002372. URL: https://opg.optica.org/ol/abstract.cfm?URI=ol-34-15-2372.

[68] Johannes Floß et al. "Observation of Bloch Oscillations in Molecular Rotation". In: *Phys. Rev. Lett.* 115 (20 Nov. 2015), p. 203002. DOI: 10.1103/PhysRevLett.115.203002. URL: https://link.aps.org/doi/10.1103/PhysRevLett.115.203002.

[69] H. J. Lugt. *Vortex Flow in Nature and Technology*. Wiley, New York, 1983.

[70] Anton S Desyatnikov, Yuri S Kivshar, and Lluis Torner. "Optical vortices and vortex solitons". In: *Progess in Optics* 47 (2005), pp. 291–391.

[71] W. F. Vinen and J. J. Niemela. "Quantum Turbulence". In: *Journal of Low Temperature Physics* 128.5 (Sept. 2002), pp. 167–231. ISSN: 1573-7357. DOI: 10.1023/A:1019695418590. URL: https://doi.org/10.1023/A:1019695418590.

[72] Bo Chen et al. "Two-dimensional vortices in superconductors". In: *Nature Physics* 3.4 (Apr. 2007), pp. 239–242. ISSN: 1745-2481. DOI: 10.1038/nphys540. URL: https://doi.org/10.1038/nphys540.

[73] I. Coddington et al. "Experimental studies of equilibrium vortex properties in a Bose-condensed gas". In: *Phys. Rev. A* 70 (6 Dec. 2004), p. 063607. DOI: 10.1103/PhysRevA.70.063607. URL: https://link.aps.org/doi/10.1103/PhysRevA.70.063607.

[74] T. W. Neely et al. "Observation of Vortex Dipoles in an Oblate Bose-Einstein Condensate". In: *Phys. Rev. Lett.* 104 (16 Apr. 2010), p. 160401. DOI: 10.1103/PhysRevLett.104.160401. URL: https://link.aps.org/doi/10.1103/PhysRevLett.104.160401.

[75] Sang Won Seo et al. "Observation of vortex-antivortex pairing in decaying 2D turbulence of a superfluid gas". In: *Scientific Reports* 7.1 (July 2017), p. 4587. ISSN: 2045-2322. DOI: 10.1038/s41598-017-04122-9. URL: https://doi.org/10.1038/s41598-017-04122-9.

[76] Audun Skaugen and Luiza Angheluta. "Vortex clustering and universal scaling laws in two-dimensional quantum turbulence". In: *Phys. Rev. E* 93 (3 Mar. 2016), p. 032106. DOI: 10.1103/PhysRevE.93.032106. URL: https://link.aps.org/doi/10.1103/PhysRevE.93.032106.

[77] Nadine Meyer et al. "Observation of Two-Dimensional Localized Jones-Roberts Solitons in Bose-Einstein Condensates". In: *Phys. Rev. Lett.* 119 (15 Oct. 2017), p. 150403. DOI: 10.1103/PhysRevLett.119.150403. URL: https://link.aps.org/doi/10.1103/PhysRevLett.119.150403.

[78] S. Gautam. "GENERATION OF VORTEX DIPOLES IN SUPERFLUID FERMI GAS IN BCS LIMIT". In: *International Journal of Modern Physics B* 27.11 (2013), p. 1350041. DOI: 10.1142/S0217979213500410. eprint: https://doi.org/10.1142/S0217979213500410. URL: https://doi.org/10.1142/S0217979213500410.

[79] R. Panico et al. *Onset of vortex clustering and inverse energy cascade in dissipative quantum fluids*. 2022. DOI: 10.48550/ARXIV.2205.02925. URL: https://arxiv.org/abs/2205.02925.

[80] E. C. Samson et al. "Deterministic creation, pinning, and manipulation of quantized vortices in a Bose-Einstein condensate". In: *Phys. Rev. A* 93 (2 Feb. 2016), p. 023603. DOI: 10.1103/PhysRevA.93.023603. URL: https://link.aps.org/doi/10.1103/PhysRevA.93.023603.

[81] P. A. Ruprecht et al. "Time-dependent solution of the nonlinear Schrödinger equation for Bose-condensed trapped neutral atoms". In: *Phys. Rev. A* 51 (6 June 1995), pp. 4704–4711. DOI: 10.1103/PhysRevA.51.4704. URL: https://link.aps.org/doi/10.1103/PhysRevA.51.4704.

[82] E. Zaremba, T. Nikuni, and A. Griffin. "Dynamics of Trapped Bose Gases at Finite Temperatures". In: *Journal of Low Temperature Physics* 116.3 (Aug. 1999), pp. 277–345. ISSN: 1573-7357. DOI: 10.1023/A:1021846002995. URL: https://doi.org/10.1023/A:1021846002995.

[83] M. J. Davis, S. A. Morgan, and K. Burnett. "Simulations of Bose Fields at Finite Temperature". In: *Phys. Rev. Lett.* 87 (16 Sept. 2001), p. 160402. DOI: 10.1103/PhysRevLett.87.160402. URL: https://link.aps.org/doi/10.1103/PhysRevLett.87.160402.

[84] Pedro Torres et al. "Vortex interaction dynamics in trapped Bose-Einstein condensates". In: *Communications on Pure and Applied Analysis* 10 (Nov. 2011). DOI: 10.3934/cpaa.2011.10.1589.

[85] Daniel Benedicto Orenes. "Realization of a spin-1 Bose-Einstein condensation experiment". Available at http://etheses.bham.ac.uk/id/eprint/8073. PhD thesis. University of Birmingham, Sept. 2017.

[86] Aviv Keshet and Wolfgang Ketterle. "A distributed, graphical user interface based, computer control system for atomic physics experiments". In: *Review of Scientific Instruments* 84.1 (Jan. 2013), p. 015105. ISSN: 0034-6748. DOI: 10.1063/1.4773536. eprint: https://pubs.aip.org/aip/rsi/article-pdf/doi/10.1063/1.4773536/14701602/015105_1_online.pdf. URL: https://doi.org/10.1063/1.4773536.

[87] John D. Jackson. *John D. Jackson*. 2004. URL: http://www2.optics.rochester.edu/workgroups/cml/opt307/spr05/john/ (visited on 07/24/2023).

[88] Y. Deng and D. Chu. "Coherence properties of different light sources and their effect on the image sharpness and speckle of holographic displays". In: *Scientific Reports* 7 (2017), p. 5893.

[89] A. E. Leanhardt et al. "Imprinting Vortices in a Bose-Einstein Condensate using Topological Phases". In: *Phys. Rev. Lett.* 89 (19 Oct. 2002), p. 190403. DOI: 10.1103/PhysRevLett.89.190403. URL: https://link.aps.org/doi/10.1103/PhysRevLett.89.190403.

[90] S. McEndoo and Th. Busch. "Vortex dynamics in anisotropic traps". In: *Phys. Rev. A* 82 (1 July 2010), p. 013628. DOI: 10.1103/PhysRevA.82.013628. URL: https://link.aps.org/doi/10.1103/PhysRevA.82.013628.

[91] Angela C. White, Carlo F. Barenghi, and Nick P. Proukakis. "Creation and characterization of vortex clusters in atomic Bose-Einstein condensates". In: *Phys. Rev. A* 86 (1 July 2012), p. 013635. DOI: 10.1103/PhysRevA.86.013635. URL: https://link.aps.org/doi/10.1103/PhysRevA.86.013635.

[92] Matthew T. Reeves et al. "Signatures of coherent vortex structures in a disordered two-dimensional quantum fluid". In: *Phys. Rev. A* 89 (5 May 2014), p. 053631. DOI: 10.1103/PhysRevA.89.053631. URL: https://link.aps.org/doi/10.1103/PhysRevA.89.053631.

[93] Guillaume Gauthier et al. "Giant vortex clusters in a two-dimensional quantum fluid". In: *Science* 364.6447 (2019), pp. 1264–1267. DOI: 10.1126/science.aat5718. eprint: https://www.science.org/doi/pdf/10.1126/science.aat5718. URL: https://www.science.org/doi/abs/10.1126/science.aat5718.

[94] T. Hastie, R. Tibshirani, and J. Friedman. *The Elements of Statistical Learning: Data Mining, Inference, and Prediction, Second Edition*. Springer Series in Statistics. Springer New York, 2009. ISBN: 9780387848587. DOI: https://doi.org/10.1007/978-0-387-84858-7. URL: https://link.springer.com/book/10.1007/978-0-387-84858-7.

[95] Joe H. Ward Jr. "Hierarchical Grouping to Optimize an Objective Function". In: *Journal of the American Statistical Association* 58.301 (1963), pp. 236–244. DOI: 10.1080/01621459.1963.10500845.

[96] S. Middelkamp et al. "Guiding-center dynamics of vortex dipoles in Bose-Einstein condensates". In: *Phys. Rev. A* 84 (1 July 2011), p. 011605. DOI: 10.1103/PhysRevA.84.011605. URL: https://link.aps.org/doi/10.1103/PhysRevA.84.011605.

[97] Alexander L Fetter and Anatoly A Svidzinsky. "Vortices in a trapped dilute Bose-Einstein condensate". In: *Journal of Physics: Condensed Matter* 13.12 (Mar. 2001), R135–R194. DOI: 10.1088/0953-8984/13/12/201. URL: https://doi.org/10.1088/0953-8984/13/12/201.

[98] J. F. ALLEN and H. JONES. "New Phenomena Connected with Heat Flow in Helium II". In: *Nature* 141.3562 (Feb. 1938), pp. 243–244. ISSN: 1476-4687. DOI: 10.1038/141243a0. URL: https://doi.org/10.1038/141243a0.

[99] Tomasz Karpiuk et al. "Superfluid fountain effect in a Bose-Einstein condensate". In: *Phys. Rev. A* 86 (3 Sept. 2012), p. 033619. DOI: 10.1103/PhysRevA.86.033619. URL: https://link.aps.org/doi/10.1103/PhysRevA.86.033619.

[100] A. F. Andreev and E. P. Bashkin. "Three-velocity hydrodynamics of superfluid solutions". In: *Soviet Journal of Experimental and Theoretical Physics* 42 (July 1975), p. 164.

[101] Jeff Steinhauer. “Observation of quantum Hawking radiation and its entanglement in an analogue black hole”. In: *Nature Physics* 12.10 (Oct. 2016), pp. 959–965. ISSN: 1745-2481. DOI: 10.1038/nphys3863. URL: https://doi.org/10.1038/nphys3863.